

# Bijendra Prasad

## 2K20PHDME03\_Thesis\_Bijendra Prasad.docx



Delhi Technological University

### Document Details

Submission ID

trn:oid:::27535:122275033

Submission Date

Nov 21, 2025, 6:02 PM GMT+5:30

Download Date

Nov 21, 2025, 6:09 PM GMT+5:30

File Name

2K20PHDME03\_Thesis\_Bijendra Prasad.docx

File Size

49.1 MB

175 Pages

33,449 Words

188,167 Characters

# 10% Overall Similarity

The combined total of all matches, including overlapping sources, for each database.





## Filtered from the Report

- Bibliography
- Quoted Text
- Cited Text
- Small Matches (less than 14 words)




## Exclusions

- 4 Excluded Sources

## Match Groups


-  **111 Not Cited or Quoted 10%**  
Matches with neither in-text citation nor quotation marks
-  **0 Missing Quotations 0%**  
Matches that are still very similar to source material
-  **0 Missing Citation 0%**  
Matches that have quotation marks, but no in-text citation
-  **0 Cited and Quoted 0%**  
Matches with in-text citation present, but no quotation marks

## Top Sources

- 7%  Internet sources
- 6%  Publications
- 4%  Submitted works (Student Papers)

## Integrity Flags

### 1 Integrity Flag for Review

-  **Replaced Characters**  
33 suspect characters on 20 pages  
Letters are swapped with similar characters from another alphabet.

Our system's algorithms look deeply at a document for any inconsistencies that would set it apart from a normal submission. If we notice something strange, we flag it for you to review.

A Flag is not necessarily an indicator of a problem. However, we'd recommend you focus your attention there for further review.

## Match Groups

- 111 Not Cited or Quoted 10%**  
Matches with neither in-text citation nor quotation marks
- 0 Missing Quotations 0%**  
Matches that are still very similar to source material
- 0 Missing Citation 0%**  
Matches that have quotation marks, but no in-text citation
- 0 Cited and Quoted 0%**  
Matches with in-text citation present, but no quotation marks

## Top Sources

- 7% Internet sources
- 6% Publications
- 4% Submitted works (Student Papers)

## Top Sources

The sources with the highest number of matches within the submission. Overlapping sources will not be displayed.

1	Internet	dspace.dtu.ac.in:8080	2%
2	Internet	www.researchgate.net	<1%
3	Publication	D Raja Satish, D Ravi Kumar. "Formability of AA6061 alloy sheets in warm forming...	<1%
4	Submitted works	IIT Delhi on 2024-07-15	<1%
5	Internet	coek.info	<1%
6	Internet	es.scribd.com	<1%
7	Publication	Pankaj Kumar Sharma, Vijay Gautam, Atul Kumar Agrawal. "Analytical and Nume...	<1%
8	Submitted works	Delhi Technological University on 2025-05-06	<1%
9	Internet	www.eprint.iitd.ac.in	<1%
10	Internet	slideplayer.com	<1%

11	Submitted works	University of Warwick on 2011-09-26	<1%
12	Submitted works	Delhi Technological University on 2024-05-23	<1%
13	Internet	docu.tips	<1%
14	Publication	Dong Nyung Lee, Yoon Keun Kim. "Tensile properties of stainless steel-clad alumi...	<1%
15	Publication	Mohammad Masoumi, Esmail Emadoddin. "Interface characterization and form...	<1%
16	Internet	moam.info	<1%
17	Publication	Shi-Hoon Choi, Keun-Hwan Kim, Kyu Hwan Oh, Dong Nyung Lee. "Tensile deform...	<1%
18	Publication	Atul S. Takalkar, Lenin Babu Mailan Chinnapandi. "Deep drawing process at the el...	<1%
19	Internet	dtu.ac.in	<1%
20	Publication	"Proceeding of 5th International Conference on Advances in Manufacturing and ...	<1%
21	Publication	D Raja Satish, D Ravi Kumar, Marion Merklein. "Effect of temperature and punch ...	<1%
22	Submitted works	Jaypee University of Information Technology on 2018-03-16	<1%
23	Publication	Vijay Gautam, D Ravi Kumar. "Experimental and numerical investigations on spri...	<1%
24	Publication	Pankaj Kumar Sharma, Vijay Gautam, Atul Kumar Agrawal. "Investigations on eff...	<1%



25	Internet	eprint.iitd.ac.in	<1%
26	Submitted works	Sabancı Universitesi on 2020-04-17	<1%
27	Submitted works	Mahidol University on 2009-07-27	<1%
28	Internet	link.springer.com	<1%
29	Publication	Amir Atrian, Hamed Panahi. "Experimental and finite element investigation on w...	<1%
30	Internet	pdfcoffee.com	<1%
31	Internet	dokumen.pub	<1%
32	Internet	www.mdpi.com	<1%
33	Submitted works	PSG Institutions on 2025-04-22	<1%
34	Submitted works	Uttar Pradesh Technical University on 2025-03-28	<1%
35	Internet	ebin.pub	<1%
36	Internet	www.labtesting.com	<1%
37	Publication	Chu Wang, Delun Li, Bao Meng, Min Wan. "Effect of Anisotropic Yield Functions o...	<1%
38	Publication	Vijay Gautam, Vinayak Manohar Raut, D Ravi Kumar. "Analytical prediction of spri...	<1%

39	Publication	Swadesh Kumar Singh. "Numerical prediction of limiting draw ratio and thicknes...	<1%
40	Submitted works	University of Hull on 2025-09-10	<1%
41	Submitted works	IIT Delhi on 2015-09-23	<1%
42	Publication	Miao Cao, Kun-kun Deng, Kai-bo Nie, Cui-ju Wang, Lifei Wang, Wei Liang. "Microst...	<1%
43	Internet	gyan.iitg.ernet.in	<1%
44	Publication	Bhadpiroon Watcharasresomroeng. "Investigation on Forming Behaviour of Shee...	<1%
45	Submitted works	University of Technology on 2017-08-01	<1%
46	Internet	doc-test.utsp.utwente.nl	<1%
47	Publication	"Springer Handbook of Mechanical Engineering", Springer Science and Business ...	<1%
48	Publication	Amir Atrian, Faramarz Fereshteh-Saniee. "Deep drawing process of steel/brass la...	<1%
49	Submitted works	University of Sheffield on 2018-09-25	<1%
50	Internet	dspace-jcboseust.refread.com	<1%
51	Internet	tudr.thapar.edu:8080	<1%
52	Internet	www.dtu.ac.in	<1%

53

Internet

www.icdd.com

<1%

**INVESTIGATIONS ON FORMABILITY OF A  
2-PLY LAMINATE COMPOSITE SHEET  
METAL AT ELEVATED TEMPERATURE**

**A Thesis Submitted  
In Fulfillment of the Requirements  
for the Degree of**

**DOCTOR OF PHILOSOPHY**

**by**

**BIJENDRA PRASAD  
(Roll No.- 2K20/PHDME/03)**

**Under the Supervision of  
Prof. VIJAY GAUTAM**



to the  
**Department of Mechanical Engineering**

**DELHI TECHNOLOGICAL UNIVERSITY  
(Formerly Delhi College of Engineering)  
Shahbad Daultapur, Main Bawana Road, Delhi-110042. India**

**November, 2025**



# DELHI TECHNOLOGICAL UNIVERSITY

(Formerly Delhi College of Engineering)  
Shahbad Daultpur, Main Bawana Road, Delhi-42

## CANDIDATE'S DECLARATION

I, **BIJENDRA PRASAD**, hereby certify that the work which is being presented in the thesis entitled “**Investigations on Formability of a 2-Ply Laminate Composite Sheet Metal at Elevated Temperature**” in partial fulfillment of the requirements for the award of the Degree of Doctor of Philosophy, submitted in the Department of Mechanical Engineering, Delhi Technological University is an authentic record of my own work carried out during the period from August, 2020 to July 2025 under the supervision of Prof Vijay Gautam, Department of Mechanical Engineering, DTU, Delhi. The matter presented in the thesis has not been submitted by me for the award of any other degree of this or any other Institute.

**Bijendra Prasad**  
(Roll No.- 2K20/PHDME/03)

8



# DELHI TECHNOLOGICAL UNIVERSITY

(Formerly Delhi College of Engineering)

Shahbad Daulatpur, Main Bawana Road, Delhi-42

## CERTIFICATE BY THE SUPERVISOR

Certified that **BIJENDRA PRASAD** (2K20/PHDME/03) has carried out their search work presented in this thesis entitled “**Investigations on Formability of a 2-Ply Laminate Composite Sheet Metal at Elevated Temperature**” for the award of **Doctor of Philosophy** from Department of Mechanical Engineering, Delhi Technological University, Delhi, under my supervision. The thesis embodies results of original work, and studies are carried out by the student himself and the contents of the thesis do not form the basis for the award of any other degree to the candidate or to anybody else from this or any other University/Institution.

12

**Prof. VIJAY GAUTAM**

Department of Mechanical Engineering

Delhi Technological University

Date:

## ACKNOWLEDGEMENTS

I would like to convey my deep sense of gratitude and sincere thanks to my supervisor Professor Vijay Gautam, Department of Mechanical Engineering, Delhi Technological University, for giving me an opportunity to pursue this research work under his guidance. He has been a tremendous mentor for me. Perseverance, exuberance, positive approaches are just some of the traits they have imprinted on my personality.

He steered me through this journey with his invaluable advice, positive criticism, stimulating discussions and consistent encouragement. If I will stand proud of my achievements, then undeniably he is the main creditor. It is my privilege to be under his guidance. His advice on both research as well as on my career have been priceless. Words are short to suffice his favour and cooperation. I am grateful to him in all respects.

I would like to express my gratitude to Prof. Prateek Sharma, Vice chancellor, Delhi Technological University, Delhi for providing this opportunity to carry out this work in this prestigious institute.

I would like to thank Prof. B.B. Arora, Head of the Department of Mechanical Engineering, and Prof. Atul Kumar Agrawal, DRC Chairman, for their support in finishing this work.

I wish to record my thanks and gratitude to my Internal SRC expert, Prof. Atul Kumar Agrawal, Department of Mechanical Engineering (Delhi Technological University); and External SRC expert Prof. Amit Kumar Srivastava, Department of Civil Engineering (Delhi Technological University), for their valuable guidance, critical and constructive discussion during this work.

I would like to thank my senior fellow research scholars Dr. Pankaj Kumar Sharma, and Dr Ravi Datt Yadav, for steering me in my challenges during PhD work. Their valuable experience was very needful in improving my quality of research work. Also, I would like to thank my fellow research scholars, especially Mr Rakesh Kumar, Mr Subhajit Konar, Mr Praveen Kumar

Singh, Mr Gaurav Ranjan, Mr Jayant, for helping and encouraging me throughout my research. Without their support and motivation, pursuit of this Ph.D. work would have never been possible.

I would like to thank lab assistant/ Senior Technician Mr. Ignatius Francis, Mr. Om Prakash and Mr. Tek Chand for their help and support during the experimental work in the Metal Forming Laboratory.

1 I sincerely thank the anonymous reviewers whose insightful and constructive comments and suggested revisions improved the organization and clarity of the research.

1 I am greatly indebted to my parents (Lt. (Retd) RB Ram and Mrs Seia Devi) for their love and blessings to see me scaling greater heights of life. With immense pleasure and delight, I would like to thank my wife Khushboo Kumari for giving me mental and moral support in my highs and lows of this PhD journey. I appreciate my little son Mayank for abiding my neglect and the patience he showed during my PhD work.

Finally, I would like to express my gratitude to the supreme personality, Lord Krishna, for giving me the patience and strength to overcome all types of hindrances.



## ABSTRACT

In pursuit of newer lightweight components, metallic laminate composite sheet, also termed as clad sheet, emerges as a solution to meet the demand for automotive and aerospace applications. The present work focuses on the effect of warm forming temperature on the tensile properties, microstructural characteristics, formability, and residual stress of a 2-ply clad sheet composed of SS430 and AA1050 layers with total thickness of 2mm. Four different temperatures are selected for characterization: room temperature, 180°C, 220°C, and 300°C. The tensile properties of the clad and the individual layers are determined as per ASTM E8M standard using a universal testing machine integrated with an environmental chamber facility. The normal and planar anisotropy of the clad sheet and individual layers are determined by evaluating the  $R$  value (Lankford value) in directions  $0^\circ$ ,  $45^\circ$  and  $90^\circ$  with rolling direction. The tensile properties and anisotropy are used to predict the finite element simulation of the deep drawing. An analytical model is also developed to determine the punch force during the deep drawing operation, incorporating the anisotropy of the parent layers.

The microstructural investigations of the clad interface and the parent layers are done through electron back scatter diffraction technique. The thermo-mechanical effects on the different texture components of the material like pole figures, inverse pole figures, kernel average misorientation, geometrically necessary dislocations and misorientation angle (high-angle and low-angle grain boundaries) are examined.

The forming limit diagrams are plotted at different temperatures through the limiting dome height experiments, with and without the use of MoS<sub>2</sub> lubricant. The H13 tool steel is used to fabricate the die, blank holder, and punch for the limiting dome height and deep drawing experiments. The experiments are also conducted to determine the limiting draw ratio at different elevated temperatures. The strength values of the clad sheet decrease as the temperature increases, whereas the ductility reduces significantly. The decrease in ductility at

elevated temperature is primarily due to the increase in the fraction of high-angle grain boundaries which obstructs the dislocation movement during plastic deformation. The strength and ductility of the clad sheet are primarily influenced by the properties of the SS430 component. The formability of the clad sheet decreases with increasing temperature on account of the increasing sticking friction between the sheet and tools. The MoS<sub>2</sub> lubricant tends to reduce the friction between the tool surfaces and hence improves the formability at the elevated temperatures. When compared to the specimen at room temperature, the limiting draw ratio of the lubricated clad sheet rises by 11% at 300°C. The experimental results are in good agreement with the predictions and the developed analytical model.

Keywords: Clad sheet, Microstructure evolution, Warm formability, Forming limit diagram, Deep drawing, Limiting draw ratio.

34

## TABLE OF CONTENTS

50

Topics	Page no
Candidate Declaration	ii
Certificate	iii
Acknowledgement	iv-v
Abstract	vi-vii
Table of Contents	viii-xi
List of Figures	xii-xvi
List of Tables	xvii
List of Abbreviations	xviii
Nomenclatures	xix-xx
<b>Chapter 1 Introduction</b>	<b>1-18</b>
1.1 Clad sheet metals	1
1.1.1 Manufacturing of clad sheet metals	1
1.1.2 Aluminium/stainless steel clad sheets	4
1.2 Sheet metal forming	6
1.3 Formability assessment	8
1.3.1 Erichsen cupping test	9
1.3.2 Limiting dome height test	9
1.3.3 Hydraulic bulge test	11
1.3.4 Swift cup drawing test	11
1.4 Forming limit diagram	12
1.5 Factors affecting formability	15
1.5.1 Strain hardening exponent	16

1.5.2	Normal and planar anisotropy	16
<b>Chapter 2 Literature review</b>		<b>19-36</b>
2.1	Clad sheet metal forming	18
2.2	Analytical model	31
2.3	Microstructure evolution	32
2.4	Research gaps	36
2.5	Research objectives	37
<b>Chapter 3 Development of analytical model</b>		<b>39-46</b>
<b>Chapter 4 Prediction of punch force in deep drawing process by finite element method</b>		<b>47-58</b>
4.1	About the software	48
4.2	Modelling and simulations of deep drawing process	48
4.3	Material model	53
4.4	Contact and boundary conditions in simulations	55
<b>Chapter 5 Experimental procedure</b>		<b>59-90</b>
5.1	Material selection	59
5.2	Determination of mechanical properties	60
5.2.1	Characterisation of tensile properties	60
5.2.2	Characterisation of Anisotropy	63
5.2.3	Determination of Residual stresses	64
5.2.4	Determination of coefficient of friction	67
5.2.5	Determination of Vickers micro-indentation hardness	68
5.3	Characterisation of the formability of the clad sheet	70

5.3.1	Design and development of experimental setup for forming at elevated temperature	71
5.3.1.1	Design of tool setup for forming limit diagram	72
5.3.1.2	Design of tool setup for deep drawing analysis	75
5.3.2	Heating system and temperature control	76
5.3.3	Hydraulic press assembly with the designed tools	79
5.3.4	Determination of forming limit diagram	82
5.3.5	Deep drawing analysis	86
5.4	Microstructural characterization	87
5.4.1	Sample preparation	88
5.4.2	Electron backscatter diffraction (EBSD)	88
<b>Chapter 6 Results and Discussion</b>		<b>91-130</b>
6.1	Mechanical properties	91
6.1.1	Tensile properties of 2-ply sheet	91
6.1.2	Residual stresses in Tensile tested 2-ply clad sheet	96
6.1.3	Vickers micro-indentation hardness results in clad sheet	97
6.1.4	Coefficient of friction results of both layers of clad sheet	99
6.2	Microstructural analysis of the 2-ply clad sheet	102
6.2.1	Microstructure of the parent and the interface layer	102
6.2.2	Inverse pole figures	104
6.2.3	Misorientation angles (LAGB and HAGB)	106
6.2.4	Geometrically necessary dislocations (GND) density	108
6.2.5	Fractography and SEM-EDAX	111
6.3	Formability analysis	114
6.3.1	Forming limit diagram of clad sheet	114

6.3.2	Deep drawing analysis of clad sheet	118
6.4	Summary	125
6.5	Industrial significance of the present work	128
<b>Chapter 7 Conclusions and future research scope</b>		<b>131-135</b>
7.1	Conclusions	131
7.2	Future research work	133
<b>References</b>		<b>136-152</b>
<b>Publications based on the present work</b>		<b>153-154</b>
<b>Biodata</b>		<b>155</b>

## LIST OF FIGURES

Fig. No.	Title	Page No.
Fig.1.1	Schematic illustration of the roll bonding process for manufacturing multi-ply clad metals	2
Fig.1.2	Common sheet metal forming operations	7
Fig.1.3	Schematic of the setup for Erichsen test	9
Fig.1.4	Schematic of the setup for limiting dome height test	10
Fig.1.5	Hydraulic bulge test setup	10
Fig.1.6	Schematic of swift cup test setup	11
Fig.1.7	Forming-limit diagrams (FLD) for various sheet metals	12
Fig.1.8	The deformation of the grid pattern and tearing during forming	13
Fig.1.9	The stretch deformed sheets of various widths	13
Fig.1.10	Strains in deformed circular grid patterns	14
Fig.3.1	A pie-shaped segment of circular blank in deep drawing process	39
Fig.3.2	Radial element in the flange region of the sheet during deep drawing	40
Fig.4.1	Shell section modelled for clad sheet	50
Fig.4.2	Meshed blank with shell section	51
Fig.4.3	A quarter symmetric 3D model of deep drawing assembly	53
Fig.4.4	The anisotropy ratios incorporated in the material properties in Abaqus	55
Fig.4.5	X-symmetry and Z-symmetry boundary condition assigned to blank	56
Fig.4.6	Velocity provided to the punch	56
Fig.4.7	Interaction properties defined for the surfaces in contact	57
Fig.5.1	Laser cutting of tensile samples in progress	60

9	Fig.5.2	Size description of sub size sample of tensile test as per ASTM E8M standard	61
	Fig.5.3	UTM (50 kN capacity) integrated with environmental chamber	62
	Fig.5.4	Tensile tested specimens	63
	Fig.5.5	Clad sheet anisotropy tested samples	64
	Fig.5.6	Portable X-ray residual stress measurement setup	63
	Fig.5.7	Coordinate system of Cosα technique using a 2D detector	66
	Fig.5.8	Linear reciprocating tribometer	68
	Fig.5.9	Struers Micro-indentation Hardness tester	70
	Fig.5.10	Engineering drawing of lower die with dimensions and solid model	73
	Fig.5.11	Engineering drawing and solid model of the die and blank holder assembly	74
	Fig.5.12	Die, blank holder, punch with heater and thermocouple assembly	74
	Fig.5.13	(a) Engineering drawing, (b) solid model, and (c) fabricated die for deep drawing	76
	Fig.5.14	(a) Engineering drawing, (b) solid model, and (c) fabricated assembly setup for deep drawing	77
	Fig.5.15	CAD assembly of hydraulic press with the designed tools	80
	Fig.5.16	Final assembly of fabricated tools integrated with 100 tonne capacity hydraulic press	81
	Fig.5.17	Clad sheet specimens used for the determination of FLD	83
	Fig.5.18	(a) Laser marking in progress with 20W laser head, (b) CAD grid pattern of 2.5mm diameter circles, and (c) laser-marked pattern on clad specimen	83



22	Fig.5.19	Clad specimen (a) before, and (b) after laser marking	83
	Fig.5.20	Deformed FLD clad sample at fracture	84
	Fig.5.21	Measurement of strains using stereo zoom microscope on a deformed specimen	85
	Fig.5.22	Dome height measurement of FLD specimen using vernier height gauge	85
	Fig.5.23	Specimen orientation for EBSD measurement	89
	Fig.5.24	Field emission gun (FEG) scanning electron microscope (SEM) for electron backscattered diffraction (EBSD) analysis	89
	Fig.6.1	True stress vs. true strain plots at different temperatures of (a) SS430 layer, (b) two-ply clad sheet and (c) AA1050 layer	92
	Fig.6.2	True stress vs. true strain plots of clad sheet, SS430 and AA1050 layers at (a) room temperature, (b) 180°C, (c) 220°C, and (d) 300°C.	93
	Fig.6.3	Variation of tensile strength in clad sheet and parent layers with temperature	94
	Fig.6.4	Debye ring and measurement condition for the residual stress measurement in the SS layer of the clad sheet	96
	Fig.6.5	The residual stress values for SS and AA layers at different temperatures	97
	Fig.6.6	Micro-indentation hardness values for SS and AA layers at different temperatures	98
	Fig.6.7	Micro-indentation formed after Vickers hardness test for (a) SS430, and (b) AA1050	99
	Fig.6.8	Coefficient of friction plot of AA050 layer under (a) no lubrication, and (b) MoS <sub>2</sub> lubrication at 300°C	100
	Fig.6.9	Coefficient of friction plot of SS430 layer under (a) no lubrication, and	101

(b) MoS<sub>2</sub> lubrication at 300°C

9	Fig.6.10	Microstructure of the (a) As-received clad sheet, (b) 20% deformed clad sheet at room temperature and (c) 20% deformed clad sheet at 300°C	103
	Fig.6.11	IPF of the AA and SS layers of (a), (d) As-received clad sheet; (b), (e) 20% deformed clad sheet at room temperature and (c), (f) 20% deformed clad sheet at 300°C	104
	Fig.6.12	Microstructure, and grain boundary map of interface region of the (a)-(b) as received clad sheet, (c)-(d) 20% plastic strained at RT, (e)-(f) 20% plastic strained at 300°C	107
	Fig.6.13	GND map of clad sheet: (a) as received, (b) 20% plastic strained at RT, (c) 20% plastic strained at 300°C	109
	Fig.6.14	GND density ( $10^{12} / \text{m}^2$ ) distribution plot of SS430 and AA1050 for (a), (d) as received sheet; (b), (e) 20% plastic strained at RT; (c), (f) 20% plastic strained at 300°C	110
	Fig.6.15	Elemental profile plot of SS/AA clad interface	112
	Fig.6.16	Fractographs of SS430/AA1050 interface at (a) RT, (b) 180°C, (c) 220°C, and (d) 300°C	112
	Fig.6.17	Necking region in tensile specimen on the (a)-(d) SS430 side, (e)-(h) AA1050 side, of the clad sheet at different temperatures	113
	Fig.6.18	Test FLD specimens of 2-ply clad sheet with steel as outer layer of dome	114
	Fig.6.19	Forming limit diagram of clad sheet at different temperatures with (a) no lubrication and (b) lubrication condition	115
	Fig.6.20	Plane strain specimens of the clad sheet from LDH test under (a) no lubrication and (b) MoS <sub>2</sub> lubrication condition	117

35	Fig.6.21	Variation of LDR of the clad sheet with temperature under different lubricating conditions	118
	Fig.6.22	FEA result of the deep drawing of clads sheet at RT under no lubrication with (a) draw ratio of 2.0 and (b) draw ratio of 1.8	119
	Fig.6.23	FEA predictions of (a) true thickness strain distribution and (b) punch force plot, of the failed and successful drawn cup at RT under no lubrication	120
	Fig.6.24	Experimental result of the deep drawing of clads sheet at RT under no lubrication with draw ratio of 2.0 and 1.8	120
	Fig.6.25	Experimental result of LDR values at different temperature under (a) no lubrication and (b) MoS <sub>2</sub> lubrication	121
	Fig.6.26	Experimental and FEA results of deep drawn cups at 300°C under different lubricating conditions	121
	Fig.6.27	Experimental and predicted punch force vs. travel plots for deep drawing	123
	Fig.6.28	Variation of maximum punch force for the LDR at different temperatures with and without lubrication	124

## LIST OF TABLES

Table. No.	Title	Page No.
Table 4.1	Details of elements and nodes for the simulations of 100 mm diameter blank	52
Table 4.2	Anisotropy yield stress ratios for the constituent materials at different temperatures	55
Table 4.3	Variation of Coefficient of friction on the SS side and AA side of the clad specimen at different temperatures under different lubrication condition	58
Table 5.1	Chemical constituent's results obtained by spark-based spectroscopy	60
Table 6.1	Tensile properties of SS430 layer	94
Table 6.2	Tensile properties of a clad sheet	94
Table 6.3	Tensile properties of AA1050 layer	94
Table 6.4	Coefficient of friction values of both materials under different lubricating condition	101
Table 6.5	Dome heights of the LDH tested specimens under no lubrication condition	116
Table 6.6	Dome heights of the LDH tested specimens under MoS <sub>2</sub> lubrication condition	116
Table 6.7	Maximum punch force of deep drawing specimens under no lubrication condition	122
Table 6.8	Maximum punch force of deep drawing specimens under MoS <sub>2</sub> lubrication condition	122

## LIST OF ABBREVIATIONS

ASTM	American Society for Testing and Materials
AA	Aluminium alloy
BHF	Blank holding force
CAE	Computer Aided Engineering
EBSD	Electron backscattered diffraction
FLD	Forming limit diagram
FEA	Finite Element Analysis
GND	Geometrically necessary dislocations
HAGB	High angle grain boundary
HV	Hardness on Vickers scale
LDR	Limiting Draw Ratio
LDH	Limiting Dome height
LAGB	Low angle grain boundary
ND	Normal direction
ODF	Orientation distribution function
RD	Rolling Direction
SS	Stainless steel
SEM	Scanning electron microscopes
TD	Transverse direction
UTS	Ultimate Tensile Strength
UTM	Universal testing machine
XRD	X-ray diffraction
YS	Yield strength

## NOMENCLATURES

$\varepsilon_z$	Strain in thickness direction
$R$	Plastic strain ratio
$\sigma_{ri}$	Radial stresses acting on sheet layer
$\sigma_{\theta i}$	Tangential stresses acting on sheet layer
$\sigma_{rc}$	Radial stress acting on the clad sheet
$t_c$	Thickness of the clad sheet
$t_i$	Layer thicknesses of individual sheets
$r$	Radius of the element
$d\sigma_{r1}$	Differential radial stress on the radial element
$k_1, k_2$	Stress tensor invariants
$a$	Material parameter in anisotropic yield criterion
$\sigma_1 \sigma_2 \sigma_3$	Principal stresses
$\bar{\sigma}$	Effective stress
$d\varepsilon_{ij}$	plastic strain increment
$\lambda$	plastic multiplier
$f$	plastic potential
$d\bar{\varepsilon}$	effective strain increment
$d\varepsilon_1 \ d\varepsilon_2$	Principal strain increment
$\varepsilon_r$	radial strain
$\varepsilon_\theta$	circumferential strain
$\varepsilon_z$	thickness strain
$K$	strength coefficient
$n$	strain hardening exponent

$K'$	Strength coefficient in plane strain condition
$\mu_{avg}$	Average friction coefficient
$F_{bh}$	Blank holding force
$r_0$	Initial blank radius
$\sigma_{wc}$	Cup wall stress
$F_{dr}$	Punch force required for deep drawing

# CHAPTER 1

## INTRODUCTION

### 1.1 Clad sheet metals

The clad sheet metals have gained significant attention across various industrial sectors due to their ability to combine the advantageous properties of two or more metals into a single, multifunctional material [1,2]. This innovative approach of material design has led to widespread applications in industries such as automotive, aerospace and energy [3–5]. In the automotive sector, clad metals are used to reduce vehicle weight while maintaining structural integrity and corrosion resistance [6]. In aerospace, these sheets serve in fuel tanks and structural panels where strength and resistance to extreme temperatures are critical [7]. The energy sector also benefits from clad materials in components that must withstand high pressure and corrosive environments, such as chemical reactors and heat exchangers [5]. The growing demand for multi-functional materials with different layers has increased the development in manufacturing techniques, with newer material combinations of different properties and thicknesses in clad sheets.

#### 1.1.1 Manufacturing of clad sheet metals

Although several fabrication techniques such as adhesive bonding, explosive pressure bonding, and seam welding are available for producing clad sheets, roll bonding has emerged as the most commonly used and a cost-effective method [8]. This process not only ensures strong metallurgical bonding but also yields clad sheets with excellent interfacial properties, making it highly suitable for industrial applications. Roll bonding is a solid-state joining technique, primarily dependent on the plastic



deformation of the bonding layers; employed in the fabrication of clad sheets, wherein two or more metal layers are joined under substantial compressive rolling pressure [9]. The integrity and functional performance of the resulting laminate are strongly influenced by critical process parameters at the bonding interface. Among these, surface preparation plays a pivotal role; oxide films and contaminants must be effectively removed, typically through acid pickling or mechanical cleaning methods such as wire brushing, to ensure the metal-to-metal contact necessary for diffusion-driven bonding [10–12]. The increased surface roughness contributes to improved interfacial adhesion by enhancing friction, promoting localized plastic deformation, and disrupting residual oxide layers, all of which collectively increase the interfacial shear strength of the sheet [13,14]. Fig. 1.1 shows the basic steps in manufacturing of a clad sheet with three ply/layers through a roll bonding technique.

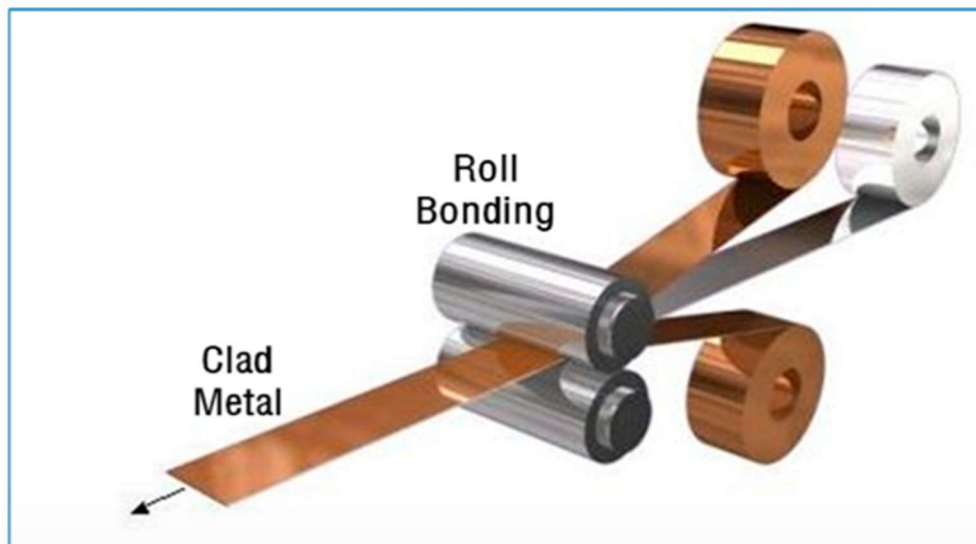


Fig 1.1 Schematic illustration of the roll bonding process for manufacturing multi-ply clad metals [15].

Atmospheric conditions during the roll bonding process play a critical role in determining the quality of interfacial bonding [16]. A high vacuum environment

significantly minimizes surface oxidation, leading to the formation of finely dispersed interfacial oxide particles that are less likely to obstruct diffusion of alloying elements across the interface. These dispersed oxide inclusions are generally favourable for bonding, as they can be broken up and distributed during plastic deformation without forming a continuous barrier for alloying elements. Conversely, processing under low vacuum or in ambient atmospheric conditions often results in the development of dense, continuous oxide layers, which act as diffusion barriers, thereby hindering atomic bonding across the interface and severely compromising the metallurgical integrity of the clad product [17,18]. To mitigate oxidation and enhance interfacial contact, controlled atmospheres such as hydrogen or argon are commonly employed during the heating and rolling stages. These inert or reducing environments suppress the formation of stable oxides on the metal surfaces, thereby facilitating improved bonding conditions [19,20]. However, achieving sufficient bond strength under inert gas conditions may require multiple rolling passes, as the absence of vacuum may not entirely eliminate oxide formation.

Rolling temperature is a crucial parameter, as operating above the recrystallization temperature promotes alloy diffusion and grain boundary migration, thereby facilitating the formation of a strong metallurgical bond and enhancing mechanical properties. However, excessive temperatures can lead to grain coarsening and phase instability, potentially compromising material integrity [21,22]. The rolling reduction ratio is another key parameter influencing the quality of clad materials. An increase in the total rolling reduction ratio typically results in a progressive decrease in the size of interfacial oxides, leading to notable improvements in peeling and fracture strengths. Additionally, post-rolling heat treatments such as quenching and tempering are

commonly applied to relieve residual stresses, refine the microstructure, and reduce interfacial defects. Careful optimization of these parameters is critical to achieving clad materials with robust interfacial bonding, excellent mechanical properties, and improved corrosion resistance, making them suitable for demanding industrial applications [23,24].

The bonding mechanism in the roll bonding process is commonly explained by four widely accepted theories: the film theory, energy barrier theory, diffusion bonding theory, and joint recrystallization theory [25]. The film theory emphasizes the disruption of surface layers during rolling, which exposes the clean base material. This material is then extruded through cracks in the oxide layer or work-hardened surface under applied rolling pressure. For bonding to occur, however, the surfaces must overcome an initial resistance [26]. This is addressed by the energy barrier theory, which posits that a minimum energy threshold is required to facilitate the rearrangement of surface atoms and the dispersion of oxide particles. The diffusion bonding and joint recrystallization theories are particularly relevant under elevated temperature conditions, where enhanced atomic mobility promotes interatomic diffusion and recrystallization at the interface [27,28]. Recrystallization, driven by thermal and mechanical energy, leads to the formation of new, strain-free grains across the bonded interface. This process significantly improves mechanical strength, enhances bond uniformity, and minimizes the formation of brittle interfacial phases.

### 1.1.2 Aluminium/stainless steel clad sheets

Aluminium/stainless steel-clad sheets offer several distinct advantages that make them highly suitable for various industrial applications. The use of aluminium significantly reduces the overall weight of the material, resulting in lightweight sheets without

compromising mechanical performance. The stainless steel layer enhances the surface hardness and provides excellent scratch resistance, ensuring durability and maintaining surface appearance. These clad sheets are also thermally conductive, as aluminium contributes to efficient heat distribution, making them ideal for applications requiring good thermal management. Moreover, both aluminium and stainless steel possess high ductility, which imparts excellent formability to the clad sheets. The presence of stainless steel also offers superior corrosion resistance, enabling the material to perform reliably in harsh or corrosive environments. Additionally, since both constituent metals are electrically conductive, the clad sheets exhibit good electrical conductivity, suitable for electrical and electronic uses. Finally, the inherent strength of stainless steel imparts high mechanical strength to the composite, ensuring that the aluminium/stainless steel-clad sheets are not only lightweight and corrosion-resistant but also strong and durable.

Aluminium/stainless steel-clad sheets find extensive applications across various industries due to their unique combination of strength, corrosion resistance, thermal conductivity, and aesthetic appeal. In the automotive sector, they are used to manufacture truck bumpers that require high corrosion resistance along with dent and scratch resistance, ensuring durability and an attractive finish. In the cookware industry, these clad sheets are preferred for their superior heat distribution, which allows for uniform and consistent cooking performance. Similarly, iron soleplates made from aluminium/stainless steel-clad sheets benefit from the even heat distribution provided by aluminium and the scratch-resistant surface of stainless steel, creating an ideal combination for smooth and efficient ironing.

Beyond automotive applications, aluminium/stainless steel-clad sheets are utilized in electrical connectors, metro rail coaches, and spacecraft chambers, where their balance of conductivity, light weight, and durability is advantageous.

In rail transport, stainless/aluminium transition strips are employed to enable the use of lightweight aluminium on steel-bodied vehicles to optimize heat diffusion in heating, ventilation, and air conditioning grills and ductworks. In the aerospace sector, these clad sheets play a vital role as aluminium alone tends to corrode when in contact with modern composite airframe materials. The stainless steel cladding provides a permanent, maintenance-free barrier between aluminium and composites, making aluminium/stainless steel-clad sheets ideal for a range of aerospace applications where strength, reliability and corrosion resistance are paramount.

## 1.2 Sheet metal forming

Sheet metal forming is one of the most widely used manufacturing processes in the production of components for industries such as automotive, aerospace, electronic appliances and cookware. It involves the plastic deformation of metal sheets into desired shapes without material removal, making it a cost-effective and efficient process for mass production. Common sheet metal operations include bending, deep drawing, stretching, spinning, hydroforming, and stamping. The ability to produce complex geometries with high dimensional accuracy and structural integrity makes sheet metal forming a critical technology in modern manufacturing.

Plastic deformation in sheet metal occurs when the material is subjected to external forces, in the form of tensile, compressive, or a combination of both types of forces to achieve the desired shape of the component without fracture. Several widely used sheet metal forming processes leverage these principles, including stretch forming, deep

drawing, and bending, each suited for different applications and geometries. These processes are illustrated in Fig. 1.2.

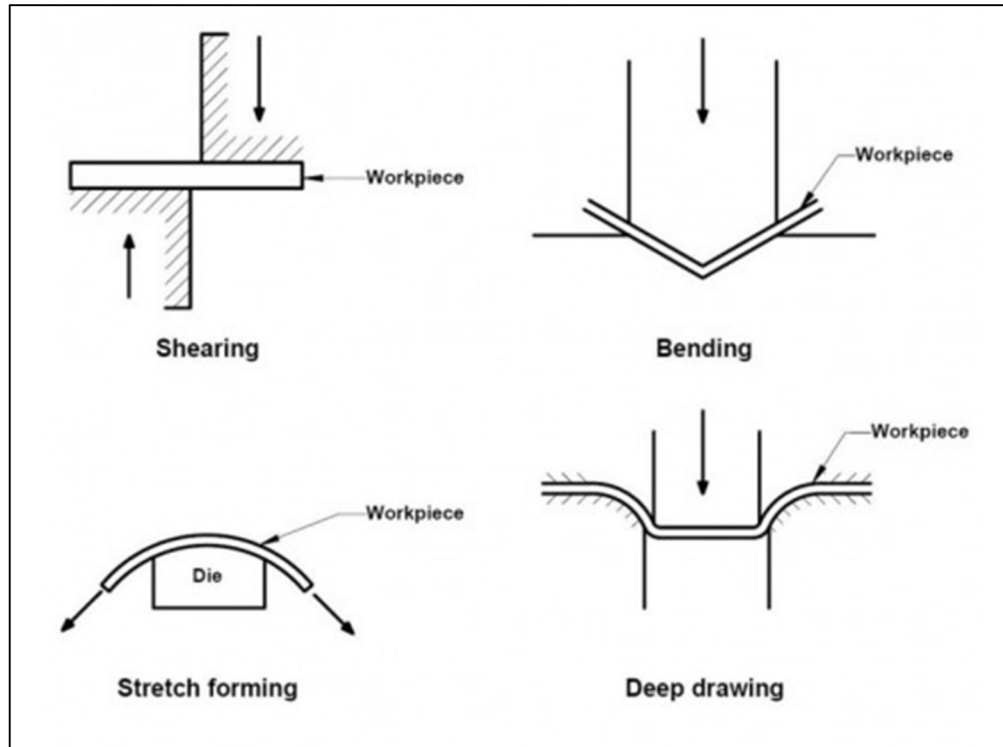


Fig. 1.2 Common sheet metal forming operations [29].

One of the fundamental techniques is stretch forming, a method in which a sheet metal blank is tightly clamped along its edges using a significant blank holding force. Once securely held in place, a rigid punch presses against the sheet to stretch it into the desired contour [30]. Unlike other forming operations that may involve compressive or bending stresses, stretch forming subjects the material predominantly to uniaxial or biaxial tensile stresses, resulting in elongation of the material surface. This process can produce parts with superior dimensional accuracy, uniform thickness distribution, and high-quality surface finishes. Due to these benefits, stretch forming is extensively utilized in the aerospace industry, where precise and smooth contours are critical, especially in manufacturing aircraft skin panels, fuselage components, and wing skins.

Compared to other forming methods, stretch forming offers enhanced control over the final geometry and reduced risk of surface defects such as wrinkling.

Deep drawing is another sheet metal forming process used to produce hollow components by drawing a sheet metal blank into a die using a punch. Unlike stretch forming, it involves both tensile and compressive stresses, particularly in the flange region where radial tensile and circumferential compressive stresses dominate. Excessive compressive stress can lead to wrinkling, which is controlled by applying an adequate blank holding force. The cup wall experiences plane strain and thinning, while the center of the blank undergoes biaxial tensile stress from contact with the punch. Deep drawing is commonly used in automotive, aerospace, and packaging industries to manufacture deep hollow parts through single or multi-stage operations [31].

### **1.3 Formability assessment**

Formability refers to the ability of a material to undergo deformation processes, such as bending, stretching, or drawing, without developing defects or fractures. It is an important parameter to design sheet metal components using various forming techniques. Formability is further influenced by material properties, process parameters, and tooling design. Formability evaluation is a complex process that often involves a combination of these parameters to obtain a comprehensive understanding of a material's behaviour under different modes of forming conditions. Sheet metal's formability is examined using a variety of tests that determine its ability to deform without fracture. The most frequent methods include experimental tests such as the Erichsen, Swift, and Fukui cupping tests, Limiting dome, Hydraulic bulge test as well as the Forming Limit Diagram (FLD), which graphically depicts the start of necking

or fracture under various strain situations. These assessments are critical for forecasting the success of a part's production before it is made. The manufacturers use these assessments to optimize the processes, select appropriate materials, and ensure the production of high-quality components. A brief overview of the common techniques for formability assessment is provided in this section [3–5]. In the automotive sector, clad metals are used to reduce vehicle weight while maintaining structural integrity.

### 1.3.1 Erichsen cupping test

The Erichsen cupping test is performed to determine the ability of the sheet metals to undergo plastic deformation in the stretch deformation mode. The schematic of the test setup is shown in Fig. 1.3. Blank samples of 100 mm x 100 mm dimension are clamped between the die and blank holder. The bore diameter of the die is 27 mm, and the inside die corner radius is 0.75 mm. A spherical punch of 20 mm diameter is provided with a linear displacement so that the sheet undergoes stretch forming till the point of instability.

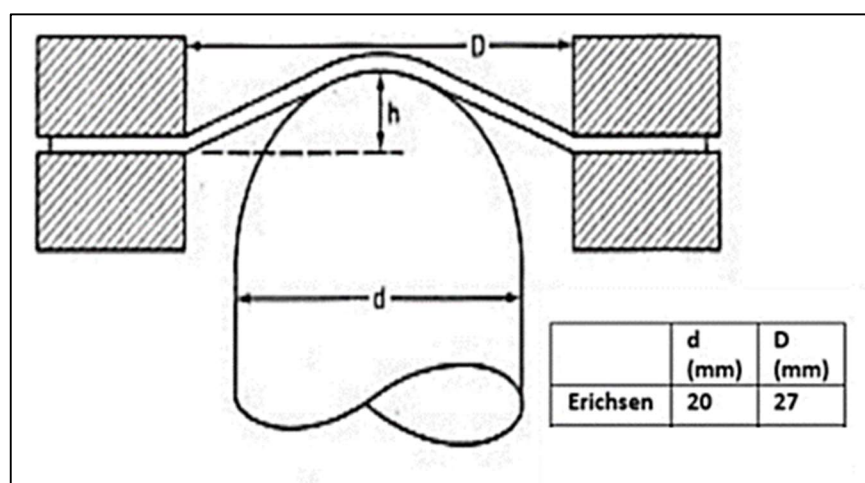
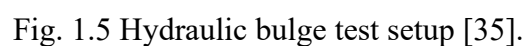
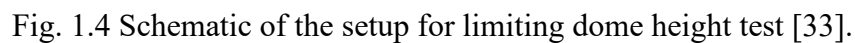


Fig. 1.3 Schematic of the setup for Erichsen test [32].

### 1.3.2 Limiting dome height test



4



### 1.3.3 Hydraulic bulge test

Another method to determine formability of a sheet subjected to biaxial stretching is hydraulic bulge test [34]. The setup consists of a pressure chamber and clamping mechanism. The pressure can be built by using fluid or gas as shown in Fig. 1.5. The bulge height at which material fails is used to estimate the formability. The advantage of this test is the absence of friction between the tool and the workpiece, and hence equibiaxial stretching can be obtained, leading to higher overall strain.

### 1.3.4 Swift cup drawing test

All the above tests are used to estimate the formability of a sheet when subjected to stretching. In order to determine drawability of a sheet, Swift flat bottom cup test is a standard method [36]. In this test, a flat bottom punch of 50 mm diameter is used to draw circular blanks of different diameter into the die (Fig. 1.6). The blank diameter is gradually increased to determine limiting draw ratio (LDR) which is defined as the ratio of the maximum blank diameter that can be drawn without failure and diameter of the punch.

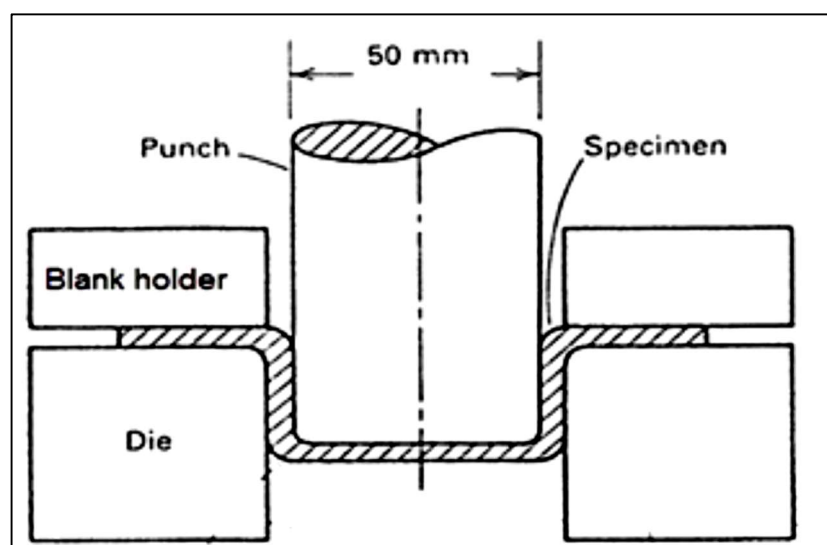


Fig. 1.6 Schematic of swift cup test setup [36].

## 1.4 Forming limit diagram

The formability assessment methods described in previous section gives formability indication at only single mode of deformation. The forming limit diagram (FLD), discussed in this section, is an important tool to find the necking limit strains at which necking/failure occurs in a sheet metal under all possible modes of deformation. Sheet metals undergo deformation only up to a certain threshold during forming, primarily determined by the ratio of major to minor strains at the onset of necking. FLD curve for some common sheet metal is shown in Fig 1.7.

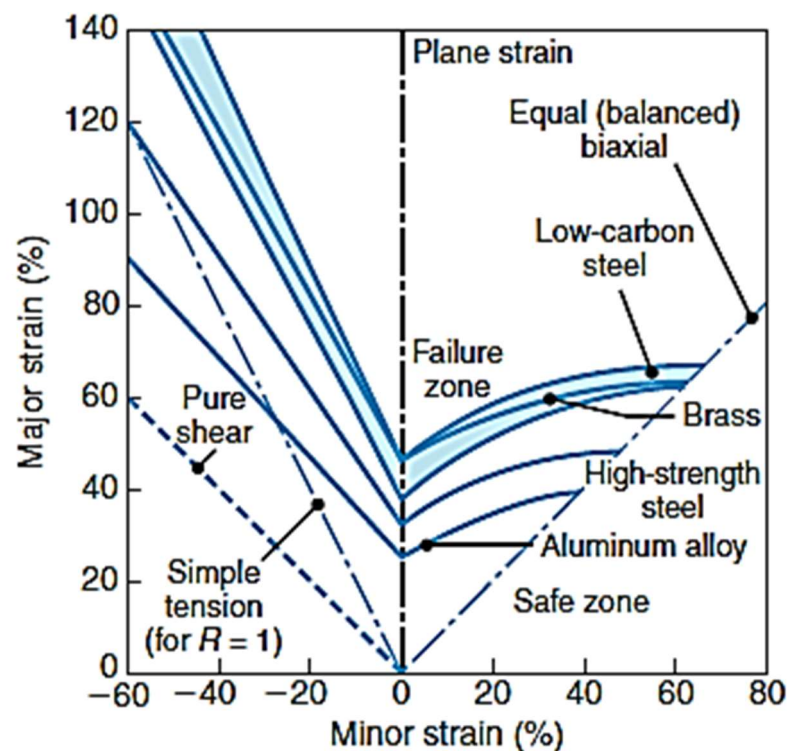


Fig. 1.7 Forming-limit diagrams (FLD) for various sheet metals [40].

Keeler [37] pioneered the concept of the Forming Limit Diagram (FLD), which correlates the major and minor strains observed at necking while sheet metal samples are stretched over a punch. Keeler's curve was limited to predicting failure for all

positive strains (biaxial strain, tension-tension), so the practical application is limited. Goodwin [38] introduced the limiting strains in the tension-compression region into Keeler's FLD curve, which could now predict the failure along the side of the punch or in corners during the stamping operations [39].

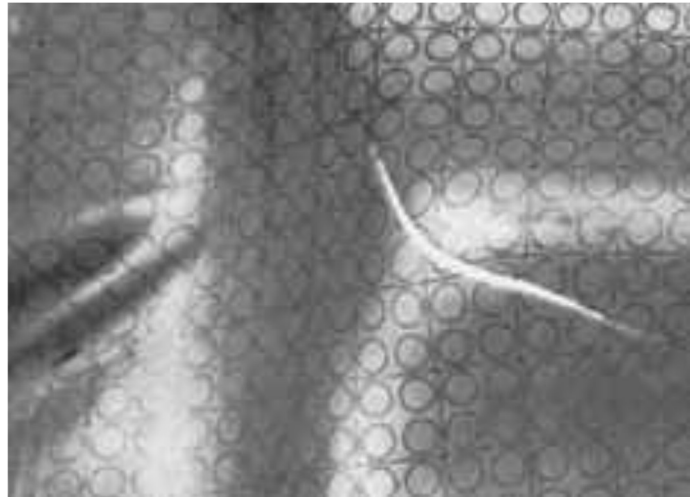


Fig. 1.8 The deformation of the grid pattern and tearing during forming [37].

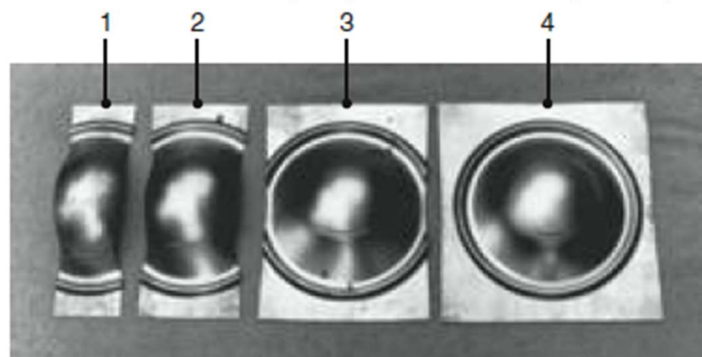


Fig. 1.9 The stretch deformed sheets of various widths [40].

Hecker [33] proposed a standard technique for obtaining limit strains in various states of strain. This method involves deforming blanks of varying widths using a hemispherical bottom punch of 101.6 mm diameter until visible necking or failure occurs on the blank. The clamping area decreases as the blank width decreases, resulting in a change in the mode of deformation. A circular draw bead present on the dies is used to clamp the blank. The circular grid method is frequently employed to

quantify the strain on the deformed sample. Nakazima [41] suggested a modified blank geometry for the evaluation of FLDs.

A forming-limit diagram (FLD) for a particular sheet metal is constructed by marking the flat sheet with a grid pattern of circles ( $\Phi 2.5$  to 5 mm in diameter), using chemical or laser marking techniques. The blank then is stretched over a punch, and the deformation of the circles is observed and measured in regions where failure (necking and tearing) has occurred, as shown in Fig 1.8.

In order to develop unequal stretching to simulate actual sheet-forming operations, the flat specimens are cut to varying widths (Fig. 1.9) and then tested. The specimen 4 (farthest right in the figure) produces equal biaxial stretching, whereas a narrow specimen 1 (farthest left in the figure) approaches the state of uniaxial stretching. After a series of such tests is performed on a particular sheet metal with different widths, a forming-limit diagram is constructed showing the boundaries between failure and safe regions.

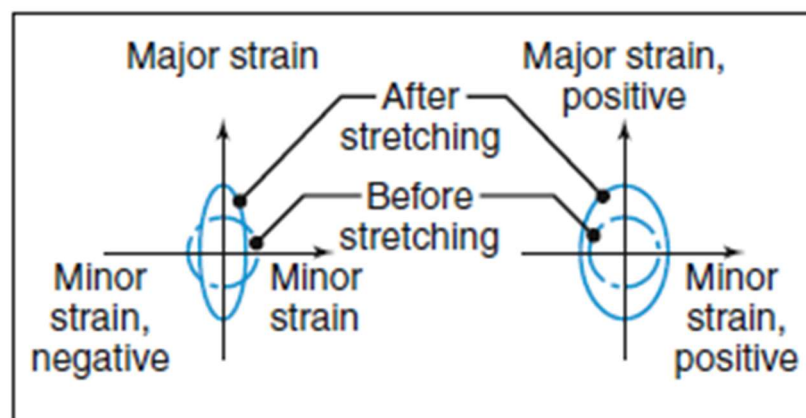


Fig. 1.10 Strains in deformed circular grid patterns [40].

In order to develop a forming-limit diagram, the major and minor engineering strains, as measured from the deformation of the original circles, are obtained. The original

6

circle has deformed into an ellipse. The major axis of the ellipse represents the major direction and magnitude of stretching, as shown in Fig 1.10. The major strain is the engineering strain in this direction and is always positive, because the sheet is being stretched. The minor axis of the ellipse represents the magnitude of the stretching or shrinking in the transverse direction. The minor strain can be either positive or negative.

## 1.5 Factors affecting formability

Formability describes the material's ability to undergo deformation processes without wrinkling, cracking, or localised necking. In the context of manufacturing and engineering, formability is crucial for shaping materials into desired geometries through processes such as bending, stretching, drawing, stamping, and other forming operations. The evaluation of formability helps ensure that materials can be successfully processed into components with complex shapes without failure. Various tests, as discussed in previous section, such as the Erichsen cupping test, Swift cup drawing test, and others, are used to evaluate the formability of sheet metal. Computational tools are often employed to simulate and predict the formability of materials under different processing conditions. In summary, formability is a critical property that influences the manufacturing and shaping of materials in various industries. The successful implementation of forming processes relies on selecting materials with suitable formability characteristics and optimizing process parameters to achieve desired shapes and components. Sheet formability is determined by a vast number of variables that interact in a complex way. These factors are divided into three categories: (a) process variables, (b) design parameters, and (c) material properties.

The process variables that significantly affect the formability by various parameter like mode of deformation, strain path, and lubrications. The design parameters are the most important factor that affects the formability of sheet, such as punch corner radius, die entry radius and punch and die clearance. The materials properties, such as strength and ductility, strain hardening exponent ( $n$ ), normal anisotropy ( $\bar{R}$ ), and strain rate sensitivity index, influence formability.

### 1.5.1 Strain hardening exponent

The strain hardening exponent ( $n$ -value) is a crucial parameter that significantly affects the formability of materials, particularly in metal forming processes. The strain hardening exponent is a measure of material's strength as it undergoes plastic deformation. The  $n$ -value primarily influences the stretchability during a forming operation. A higher  $n$ -value increases the uniformity of strain distribution in the presence of a stress gradient. It is a key factor in understanding the stress-strain behaviour of a material during plastic deformation. A little effect of  $n$  value is observed in deep drawing operations. The strain hardening exponent [42] is often associated with the power-law relationship between stress ( $\sigma$ ) and strain ( $\epsilon$ ) in the form of  $\sigma = K\epsilon^n$ , where:  $\sigma$  is the true stress,  $\epsilon$  is the true strain,  $K$  is strength coefficient, and  $n$  is the strain hardening exponent.

### 1.5.2 Normal and planar anisotropy

In most sheet metals, grains tend to have preferred crystallographic planes or directions that correspond to previous working directions. As a result, slip systems are orientated, allowing for easier deformation in certain directions than others. This situation results in plastic anisotropy in which properties are different in different directions. The plastic anisotropy is classified into two types: Normal and planar anisotropy. The

normal anisotropy ( $\bar{R}$ ) is a phenomenon that occurs in materials where the mechanical properties, such as yield strength, tensile strength, and elongation, vary with the direction of testing or deformation. This directional dependence of mechanical properties can significantly impact the formability of materials, especially in sheet metal forming processes. Normal anisotropy specifically refers to the variation of properties in the plane normal to the rolling or forming direction. Engineers need to carefully consider the directional dependence of mechanical properties when designing components or selecting materials for applications involving significant plastic deformation. Optimization strategies and informed material selection can help achieve the desired balance between anisotropy and formability.

The mechanical properties of sheet metals vary depending upon the rolling direction (RD). This dependency of mechanical properties on orientation is referred to as anisotropy. The plastic strain ratio ( $R$ ) is defined as the ratio of strain in width ( $\epsilon_w$ ) to strain in thickness ( $\epsilon_t$ ), and it is used to analyze anisotropy in sheets. The plastic strain ratio ( $R$ ) [31] defined as:

$$R = \frac{\epsilon_w}{\epsilon_t} \quad (1.1)$$

The plastic strain ratio ( $R$ ) is calculated by using experimental results from tested specimens cut at  $0^\circ$ ,  $45^\circ$ , and  $90^\circ$  to the RD. The determined values of  $R$ , are  $R_0$ ,  $R_{45}$ , and  $R_{90}$ , respectively. Planar anisotropy ( $\Delta R$ ) is measured by the average variation [31], which may be written as:

$$\Delta R = (R_0 - 2R_{45} + R_{90}) / 2 \quad (1.2)$$

The normal anisotropy ( $\bar{R}$ ) or average plastic strain ratio is written as:

$$\bar{R} = (R_0 + 2R_{45} + R_{90}) / 4 \quad (1.3)$$



When  $R$  is larger than '1' in any orientation, it means that the thickness direction has a higher strength value than the other directions. The drawability is improved and the thinning impact is lessened when  $R$  is higher.

## CHAPTER 2

### LITERATURE REVIEW

1

Formability is the ability of a given sheet metal to undergo plastic deformation without being damaged. The plastic deformation capacity of metallic materials is limited to a certain extent, beyond which the material could experience fracture or tearing. Knowledge of the material formability is very important for the design and layout of any industrial forming process. In this chapter, a detailed review of available literature on factors affecting the formability of the clad sheet is carried out.

#### 2.1 Clad sheet metal forming

Several studies exploring the mechanical properties, formability and springback in bending have been conducted on the most commonly used material combinations like 2-ply clad sheet of aluminium/stainless steel, aluminium/copper, aluminium/iron, and 3-ply clad sheet of zinc/aluminium/stainless steel, aluminium/copper/steel, austenitic stainless steel/aluminium/ ferritic stainless steel [43–46].

The combination of different materials is intended to compensate for the disadvantages of other materials while also leveraging the positive properties of each constituent material, which together offer a singularly complex function affecting the plastic behaviour of the clad sheet [47]. The mechanism of plastic deformation in a clad sheet is also influenced by several factors, including the properties of the individual layers, thickness, the stacking sequence of different layers, surface characteristics, bonding mechanism and parameters, and heat treatment [48,49].

Akramifard et al. investigated the mechanical properties of cold roll bonded AA1050/AISI304 clad sheet. The bonding mechanism was attributed to the extrusion

of aluminium into surface cracks of 304L due to strong Al–Fe affinity, confirmed by the XRD patterns. Annealing at 500–600 °C, an intermetallic layer comprising  $\text{Al}_{13}\text{Fe}_4$ , FeC and  $\text{Al}_8\text{SiC}_7$  was formed at the interface. After 600 °C, longitudinal cracking occurred between the intermetallic layer and aluminium, causing debonding.

To estimate the mechanical properties of the Al/ stainless steel clad sheet, tension tests at room temperature were performed. The results showed a significant drop in flow stress after the maximum point of the stress–strain plots (UTS) corresponding to the debonding of the interface. The UTS values were much lower than the tensile strength of the parent material, 304L stainless steel (722MPa), but were found to be significantly higher than that of the annealed Al (72 MPa). A marked drop in flow stress beyond the UTS was linked to interface debonding [50].

Choi et al. investigated the deformation behaviour of stainless steel clad aluminum sheet under uniaxial tension. The warping phenomenon was observed and the radius of curvature decreased with increasing uniaxial strain. A difference in plastic strain ratio of component layers of the bilayer sheet gives rise to warping of the tensile specimen. Consequently, the flow stresses of the bilayer sheet follow the rule of mixtures [51].

Lee and Kim investigated the application of rule of mixtures to predict the flow stress in stainless steel-aluminium-stainless steel sandwich sheets. The rule of mixtures, an average of component properties weighted by volume fractions, could be applied to the tensile strengths and strength coefficients of the sandwich specimens. The yield strengths of the sandwich sheets showed a positive deviation from the rule of mixtures due to big differences between elastic moduli of components. It was also concluded

that the rule could be applied to uniform elongations, strain hardening exponents and strain rate sensitivities of the sandwich sheets [52].

Masoumi and Emadoddin carried out the research work on formability and bond strength between two and three-layered Al-Al/11%SiC clad sheets, manufactured by the cold roll bonding process with different thickness reductions and different number of layers, by Erichsen cupping test and lap shear test. The bond strength of the multilayer sheet increased with increasing rolling reduction. In contrast, the bond strength of multilayer sheet decreased with increasing the number of layers in sheets. The dome height decreases with the addition of reinforcing particles in the aluminium matrix. Also, the dome height did not change significantly with increasing the number of layers [53].

Yoshida and Hino investigated the formability of two and three ply steel-aluminium clad sheets. It was observed that in the analytical predictions based on Hill's theory of localized necking and the experimental observations, the FLDs of the laminates lie between those of their component sheet metals. The effect of pre-strain due to thickness reduction in the roll-bonding process resulted in a significant reduction of the formability. It was also observed that when a sheet of low formability was clad by other sheets of higher formability, the clad sheet metal had much higher formability than the low-formability component [54].

Kim et al. fabricated AA1050/low-carbon steel/AA1050 laminated clad sheets using roll bonding to investigate the effects of heterostructure on mechanical behavior and formability. The results showed that the interfaces were well bonded without cracks or brittle intermetallics, although mechanical incompatibility existed between the aluminum and steel layers. The clad sheets exhibited simultaneous improvement in

both strength and ductility from those estimated by the rule of mixtures, attributed to interface synergy, which increased rapidly up to 5% strain and correlated with the evolution of geometrically necessary dislocations (GNDs). During deformation beyond necking, internal stress concentration between layers led to microcrack formation and eventual delamination at fracture sites. Enhanced strain hardening from interface synergy and controlled debonding during forming improved the Erichsen index compared to the rule of mixtures. The delamination helped delay fracture by absorbing energy, inhibiting crack initiation, and slowing crack propagation, demonstrating that interface synergy and controlled delamination together enhanced both formability and fracture resistance of the laminated sheets [55].

42 Cao et al. fabricated Ti/Al/Ti laminated clad sheet by hot pressing at 450–600 °C to examine the influence of interfacial bonding strength on their microstructure, mechanical properties, and formability. All composites exhibited well-bonded interfaces with micron-scale  $\text{TiAl}_3$  intermetallic phases. As the hot-pressing temperature increased, the Ti/Al interface became more curved, leading to higher interfacial bonding strength and microhardness. However, the ultimate tensile strength (UTS) decreased at higher temperatures due to increased shear fracture tendency at curved interfaces and material softening. Between 450 °C and 550 °C, both yield strength and UTS exceeded the rule of mixtures predictions, attributed to intermetallic strengthening, back-stress effects, and interface strengthening.

The Erichsen index value, indicating formability, showed a nonlinear trend, decreasing from 450 °C to 550 °C and then increasing at 600 °C, reflecting the influence of interfacial strength on crack initiation and propagation. At lower temperatures, weak

interfacial bonding promoted local debonding that enhanced ductility and energy absorption, resulting in better damage tolerance and higher Erichsen values [56].

Manesh et al. fabricated aluminum-steel clad sheets through cold rolling, followed by annealing which led to the formation of brittle Al–Fe intermetallics at the interface. The formability of the clad sheet was evaluated using the Erichsen cupping test, and bond strength was assessed through macroscopic examination of fractured surfaces. Results revealed that both annealing temperature and time strongly influence bonding and formability due to intermetallic growth. Maximum formability and good bond strength, were achieved at 450 °C for 16 hours. Additionally, the thickness of the intermetallic layer increased with higher annealing temperatures, which could adversely affect ductility and bonding quality [57].

5 Basril et al. investigated the effect of heating temperature on formability of different metal sheets like Mild steel, Stainless steel, and Aluminum during the deep drawing of a square cup. The thickness distribution in the deep drawn square cup was compared for three different temperatures, at different tooling locations by using a numerical and experimental approach. It was observed that the uniform thickness distribution in the square cup was achieved by utilizing the die heating technique to maintain a temperature of 150°C [58].

Jayahari et al. investigated the warm deep drawing behavior of ASS 304 stainless steel sheets using a specially designed experimental setup with a hydraulic press and induction furnace to enable forming at elevated temperatures. Circular blanks of 1 mm thickness and 60 mm diameter were tested under varying punch speeds and blank holding pressures to determine optimal forming conditions. Molycote® grease lubrication and a water-cooling system were employed to manage friction and

temperature. Results showed that blank holding pressure significantly influenced formability. At low pressure (10 bar), severe wrinkling and tearing occurred due to inadequate material flow, while high pressure (25 bar) restricted flow and caused fractures at the punch corner. The best results were obtained at an intermediate pressure of 20 bar, where defect-free cups were formed, indicating this as the optimal blank holding pressure at room temperature. Punch speed was then varied (10, 15, and 20 mm/s) at constant pressure (20 bar) and different temperatures (room temperature, 150 °C, and 300 °C). It was observed that higher punch speeds and temperatures reduced formability, consistent with dynamic strain aging behavior in ASS 304, where dislocation interactions cause unusual strengthening. Metallographic studies revealed that increased punch speed promoted martensite formation and grain refinement at the punch corner, raising strength but lowering ductility. Load–displacement data confirmed that punch load decreased with increasing temperature but slightly increased at 300 °C and higher speeds due to dynamic strain aging [59].

Ghosh et al. carried out the warm deep drawing to investigate the forming behavior of two Al-Mg-Si alloys. Among the selected parameters, the temperature was found to be significantly influencing the force-displacement curve, whereas the anisotropy was found to be significantly influencing the earing profile. The number of ears observed remains the same, but the amplitude decreases with an increase in temperature. At room temperature, a reduction in the friction force led to an increase in ear height. When the temperature was raised to 250 °C, the ear height decreased, which could be attributed to changes in frictional conditions or plastic anisotropy. The dominant cube texture orientation was responsible for the uniform reduction in ear height along both the rolling direction and the transverse direction [60].

Alinia et al. investigated the process parameter optimization for the warm deep drawing experiments of 1 mm thick ASS304 Steel using a specialized developed setup, over a temperature range from room temperature to 300 °C. A Box Behnken Design combined with Response Surface Methodology was used to analyze the effects of process parameters. Results showed that temperature and matrix cavity corner radius had the greatest influence on the limiting drawing ratio (LDR), which reached its maximum at higher matrix radii and temperatures up to 150 °C before decreasing beyond that point. The most uniform thickness distribution occurred at medium blank holding force (BHF) values, with optimal conditions achieved at high punch radius, low matrix radius, and around 255 °C. Lower BHF reduced the maximum punch force required, and larger corner radii of both punch and matrix, along with higher temperatures, further minimized punch force, leading to reduced equipment costs. The optimal combination of parameters for best overall performance was identified as BHF of 2.2 kN, punch corner radius of 7.5 mm, matrix radius of 5 mm, and temperature of 160 °C. Analysis of variance confirmed that temperature was the dominant factor affecting thickness distribution and punch force, while matrix cavity radius had the strongest effect on LDR [61].

Goud et al. investigated the formability of EDD Steel at the elevated temperature. The stretch forming operation was carried out by using warm forming tooling setup (Ni-based superalloy dies) to generate the Forming Limit Diagram (FLD) for room temperature and elevated temperature. It was observed that the formability increased with the increase in temperature due to the decrease in mean flow stresses except at the temperature of 450°C. The low formability was observed at the temperature of 450°C due to dynamic strain regime [62].



Basak et al. conducted a comprehensive study on the formability and fracture behavior of as-received and pre-strained EDD and AA5052 sheet materials, through both experimental investigations and finite element (FE) simulations. The pre-straining conditions included as 5% and 10% equi-biaxial pre-strains, 10% plane strain pre-strain, and 10% uni-axial pre-strain, applied through a laboratory-scale setup. Three yield models, Hill48-r, Hill48- $\sigma$ , and Yld2000-2d, were incorporated into the FE simulations to predict material behavior, while formability was assessed using Marciniak-Kuczynski forming limit diagrams (MK-FLDs) and fracture behavior was predicted using a newly developed anisotropic Bai-Wierzbicki fracture model. The results revealed that the limiting drawing ratio of pre-strained materials decreased with increasing effective pre-strain, with the 10% effective strain condition exhibiting the lowest drawability and maximum thinning at the cup bottom corner. Among the yield models, the Yld2000-2d model coupled with MK-FLD most accurately predicted the experimental LDR and thickness distribution, while the Hill48-r and Hill48- $\sigma$  models either over- or under-estimated the LDR for both materials. Further, the Yld2000-2d model combined with MK-FLD achieved excellent correlation between experimental and simulated results, with maximum errors of 1.52% and 1.69% for EDD and AA5052 sheets, respectively. The incorporation of the BW fracture model enabled accurate prediction of fracture initiation, with errors as low as 2.5% and 4.1% for EDD and AA5052 sheets, respectively. Moreover, applying the BW fracture model significantly improved the accuracy of cup height prediction across all pre-strained conditions. Overall, the integration of the Yld2000-2d yield model with the anisotropic BW fracture criterion provided an accurate and reliable framework for predicting the

formability and fracture of both as-received and pre-strained EDD and AA5052 sheet materials [63].

Singh et al. studied the deep drawing behavior of commercially pure titanium (CP Ti), focusing on predicting and minimizing earing defects using the CPB06 plasticity theory within a finite element model validated by experiments. The investigation established the limiting drawing ratio of 2.143 at a constant blank holding force of 23 kN, with the maximum cup height occurring along the drawing direction and an earing height of about 13.7% of the total cup height, indicating significant non-uniform material flow. To address this, a two-stage blank modification method was developed based on anisotropy in tensile yield strength and r-value, leading to an 83% reduction in earing height with only a minor 6% decrease in minimum cup height. The CPB06 anisotropy model, formulated using experimental tensile and compression data, was integrated into the finite element framework along with the Swift hardening law, successfully replicating experimental trends in material flow, earing profile, and thickness distribution. Furthermore, the optimized blank design not only minimized earing but also resulted in a 22% reduction in peak forming load and a 45% decrease in thickness variation at the cup top edge, demonstrating improved formability and material utilization [64].

Lin et al. investigated the effect of plastic anisotropy of ZK60 magnesium alloy sheet on its forming characteristics during deep drawing process. The earing behavior of the sheet during deep drawing was studied by both experimental and finite element analyses. The ZK60 alloy sheet exhibits higher plastic strain ratio (r) value in 45° than those in 0° and 90° to rolling direction, and the r value decreases with temperature increasing in various loading directions. A negative planar anisotropy value results in

2

earing in 45° to rolling direction. With drawing ratio increasing, the average earing ratio first increases to a peak and then drops, showing a bell-shape curve. The average earing ratio of cylindrical drawn cup increases as the deep drawing proceeds. At the shoulder region of drawn cups, the most reduction in thickness strain occurs in 45° to rolling direction of the sheet. At the necking region, the minimum thickness strain in 0° is lower than those in 45° and 90° directions [65].

Atrian et al. investigated the forming behaviour of SS/Brass laminated sheet through deep drawing experiments and finite element simulations of composite blanks. The simulation results showed that the drawing force was slightly overestimated by about 10%. A linear relationship was established between the initial blank diameter and the maximum drawing force, an increase in diameter from 7.5 cm to 10 cm nearly doubled the required load. Similar to single-layer deep drawing, the peak punch force occurred when the outer diameter of the drawn part reached approximately 77% of the initial blank diameter. The stacking sequence of layers was found to significantly influence forming behavior, with simulations revealing its dependency on frictional conditions. Further analyses indicated that the punch profile radius region was the most critical area prone to fracture [66].

Atrain et al. investigated the wrinkling behaviour in deep drawing process of Al3105/polypropylene/SS304, experimentally and through finite element simulations, examining the effects of blank holder force on wrinkling of blank's flange and punch force. The results indicate a reduction in wrinkling of the deep drawn cups with increase in blank holder force. The results showed that increasing the blank holding force from 6.4 kN to 12.8 kN reduced wrinkling and produced high-quality cups, while higher holding force values caused tearing. Finite element simulations slightly

underestimated the punch force by about 10% compared to experiments. The thickness strain analysis revealed that the most critical region prone to tearing was around 45 mm from the center [67].

Pazand et al. investigated the formability of three-layered clad sheet metal of AA3004/SUS304/Cu1011. The investigation demonstrated a notable impact of layer arrangement relative to the punch on the Forming Limit Diagram (FLD). Notably, when the innermost layer of AA3105 was made to contact with the punch during forming operation, followed by Cu1011 sandwich layer in the middle, and SUS304 as the outer layer, a marked improvement in the formability of the clad sheet was observed. It was concluded that the higher FLD was achieved when the layer in contact with the punch was a material's layer with the lowest strength [68].

Karajibani et al. performed the numerical and experimental analysis of deep drawability of two-layered (AA/Steel) clad sheet to evaluate the influence of parameters such as individual layer thickness, die and punch corner radius, friction coefficients at the punch-blank and die-blank interfaces, and material lay-up on the limiting draw ratio. Results showed that the limiting drawing ratio of the clad sheet lies between those of its individual layers, depending on their thickness proportions. Increasing the thickness of the high formability component or the die corner radius improved formability. The LDR also increased with higher friction between the blank and punch but decreased with higher friction between the blank and die. Additionally, placing the more formable layer in contact with the punch significantly enhanced the limiting drawing ratio [69].

Afshin and Kadkhodayan conducted a thorough experimental study on the deep-drawing operation at elevated temperature of a two ply AA1050/SS304 laminated

sheet at three different temperatures. In order to achieve diverse grain sizes, aluminium sheet was annealed at three different temperatures for one hour. It was found that with a higher grain size, the coefficient of friction enhanced too, which also resulted in an adverse influence on the material's formability. Although, the formability was significantly influenced by increasing the blank holder force, the warm deep-drawing could be carried out at elevated temperatures with a lower load demand [70].

A higher temperature above  $0.55T_m$  (where  $T_m$  is melting temperature) is the point at which hot forming is carried out resulting in stress free grain refinement via simultaneous recrystallization. The typical temperature range for warm forming is 0.35 to 0.55 times the metal's melting point [71]. On the other hand, by reducing the yield stress, warm forming enhances a material's requirement for forming loads. Because of the higher flow stress of the material being deformed at warm forming temperature range, forming processes require comparatively higher forming pressures for deformation than hot forming processes but lower forming loads compared to the forming at room temperature [72]. To lower forming forces and improve formability, warm forming is applied to various alloy steels [73], magnesium alloys, aluminium alloys, etc [74]. Warm forming of aluminium alloys involves age-hardening which necessitates the understanding of the relationships between temperature, degree of deformation, precipitation kinetics, and exposure period [75]. It is also observed that precipitation during warm forming of blank can affect the drawing force and maximum force, depending on the dwell time at a particular temperature with certain lubrication conditions. In warm forming, the friction at the interface of tooling/workpiece severely affects sheet metal's formability in addition to the material's characteristics [76]. The main issues encountered during warm temperature forming procedures include

excessive wear of the tooling surface and higher friction caused by the sheet metal's strong adhesion to the tooling surface, resulting in fatigue of the forming tools. It is a fact that interface friction is higher in warm forming conditions compared to the friction in cold forming. The tribology of warm and hot metal forming is a complex phenomenon because of the several factors contributed by choice of materials, surface coatings, lubricants, contact pressure, and temperature [77].

## 2.2 Analytical model

Analytical models are vital in deep drawing because they allow for the speedy and cost-effective prediction of process outcomes and parameter optimization without the need for physical experimentation. They aid in understanding the impact of elements like as friction, strain hardening, and material qualities on forces, dimensions, and limits, which is useful for initial design and optimization.

The analytical model to predict the punch force during deep drawing of monolithic sheet was developed by Leu, incorporating the normal anisotropy based on the Hill's yield criterion. This analytical model predicted the results of drawing loads for sheets of ferrous alloys with an error of about 5% with the experimental results. The predictions of punch force for copper and aluminium alloys were in the range of 15% to 28% of the experimental results [78].

Another analytical model developed by Azodi et al. predicted the punch force for monolithic sheet using the Barlat-89 anisotropic yield criterion using a constant value of material parameter,  $a=2$ , for all the materials. The predictions based on Barlat-89 and Hill's anisotropic yield criterion were found to be similar, attributed to the same value of material parameter incorporated in both the models [79]. It was suggested to consider the value of the material parameter to be 6 and 8 for BCC and FCC metals,

respectively, in the Barlat-89 yield criterion [80].

2 Aghchai et al. investigated the formability of two-layer Al1100-St12 laminated sheet. Theoretical and experimental approaches have been used to obtain the forming limit diagram of the two-layer Al1100-St12 sheet, and the obtained results are compared. Also, the forming limit diagram of the two-layer sheet is compared with the formability of its metallic components. Results showed a good agreement between theoretical and experimental results. It is also shown that the two-layer metallic sheet formability is better than its lower formability component [81].

2 Bagherzadeh et al. developed the analytical model to investigate the stress analysis and instability condition in hydro-mechanical deep drawing of cylindrical Al/Carbon Steel cups. Based on these models, several parametric studies were performed regarding to the effect of thickness of layers, setting condition of layers, drawing ratio and frictional condition on key parameter of critical fluid pressure of process. The experimental works were performed on Aluminum (1050-H0)/Carbon steel (St13) two-layer sheets for verification of analytical results and the prediction of actual working pressure window. It was demonstrated that the fluid pressure range for a successful forming could be rapidly predicted with a reasonable accuracy by the analytic model compared to lengthy and costly FEA or experimentation [82].

## 2.3 Microstructure evolution

Microstructure analysis is very important in deep drawing because it explains and forecasts how a material will react throughout the process, which has a direct impact on the quality and success of the final output. It aids in the optimization of process parameters to obtain desired qualities like ductility, strength, and formability by

recognizing how elements like grain size, texture, and flaws influence failures like wrinkling, cracking, or excessive thinning.

Li et al. investigated the interfacial and microstructural evolution of the corrugated roll-bonded Cu/Al clad, revealing strong interfacial bonding without intermetallic compound formation. SEM and EDS analysis confirm a tightly bonded, wavy interface with elemental diffusion but no formation of intermetallic compounds. EBSD results show significant grain refinement near the interface, especially at the trough position, where grains are smaller and more elongated due to higher strain. Misorientation angle analysis shows that high-angle grain boundaries (HAGBs) dominate in Cu, while low-angle grain boundaries (LAGBs) are prevalent in Al, with variations linked to local strain [83].

Dhib et al. studied the microstructure and mechanical properties of hot roll bonded low carbon steel/austenitic stainless steel clad composite. It was observed that the bonding process led to the formation of a decarburized ferrite zone and a carburized austenite zone along the interface, caused by the diffusion of elements like carbon, Ni, and Cr. This carburized layer, being brittle, was a crucial factor in the formation of interface cracks during fracture [84].

Liu et al. investigated the microstructure evolution of stainless steel /carbon steel clad laminate processed through corrugated rolling and flat rolling. The EBSD analysis revealed significant microstructural differences between the two rolling methods. In the SS 316L layer, LAGBs increased from peak to trough, with average misorientation decreasing from 21.8° to 12.2°, indicating greater grain refinement at the trough due to higher equivalent plastic strain. Conversely, in the carbon steel layer, LAGBs decreased and misorientation increased from peak to trough. These trends were



influenced by differences in stacking fault energy (SFE) and crystal structures: 316L (FCC, low SFE) promotes dislocation entanglement and twin formation, while carbon steel (BCC, high SFE) favoured dynamic recovery. Flat rolled sheet's bonding showed intermediate values in peaks and troughs as compared to corrugated rolled sheets [85]. Wu et al. investigated the microstructure of the Mg/Al laminated composite and found that it evolved significantly during accumulated roll bonding. Mg grains were refined during the initial sandwich preparation and became more homogenized due to high temperature deformation and interval annealing. With increasing rolling cycles, especially up to the second cycle, the microstructure remained stable, enhancing the strength. However, in the third cycle, microstructural degradation occurred due to the cracking of coarse Mg/Al intermetallic compounds and the rupture of Al layer, contributing to reduced mechanical integrity along the rolling direction [86].

Li et al. studied that in the asymmetrical roll-bonded Al/Cu laminated composites, severe deformation by extrusion enhanced the interfacial bonding. Subsequent high-temperature annealing promoted the atomic diffusion and intermetallic compound formation, with peak bonding strength achieved at 300 °C due to solution strengthening. Grain refinement in the matrix improved the tensile strength, and a thin interfacial layer facilitated the dislocation movement to enhance ductility. However, an excessive intermetallic growth can cause interface delamination, negatively affecting the composite's mechanical performance [87].

Wang et al. investigated the microstructural evolution of AZ31B Mg/5052 Al laminates after two-step roll bonding, corrugated rolling followed by a flat rolling. In the case of corrugated rolled sheets, coarse  $\alpha$ -Mg grains were refined by dynamic recrystallization, producing fine equiaxed grains and twins, especially near the

interface. Whereas, in flat rolled sheet, both Mg and Al grains were refined and further annealing resulted in equiaxed grains. Enhanced interface bonding, refined microstructure, and texture strengthening resulted in improved tensile properties and dimensional stability in the composite sheet [88].

Nie et al. studied the microstructure of Al/Mg/Ag clad sheets after four-pass rolling (71% reduction) and annealing. In the Al layer, low-angle grain boundaries dominated due to high dislocation density, with minimal recrystallization. The Mg layer shows significant dynamic and static recrystallization, with high-angle grain boundaries and highly recrystallized grains. The clad sheet exhibited improved strength and ductility compared to monolithic Mg sheet [89].

Han et al. studied the effect of annealing (350–450 °C) on the microstructure and mechanical properties of corrugated roll-bonded Cu/Al clad sheets. The layers of intermetallic compounds, including  $\text{CuAl}_2$ ,  $\text{Cu}_9\text{Al}_4$ , and  $\text{CuAl}$ , formed unevenly due to varying plastic deformation. The interface layer growth was fastest in highly deformed areas, especially the front waist of the peak, due to enhanced atomic diffusion from high dislocation density and grain boundaries. Optimal bonding strength was achieved at 350 °C for 60 min, due to refined microstructure and controlled transition layer growth [90].

Carpenter et al. examined the texture evolution in a Zr–Nb composite produced through accumulative roll bonding with intermittent annealing. The resulting textures differed significantly from those in conventionally rolled and non-annealed materials. Neutron diffraction revealed a strong fiber texture in the Nb phase of the 92 nm composite, dominated by  $\{001\}\langle 110 \rangle$  texture, with additional peaks at  $\{115\}\langle 110 \rangle$  and near  $\{334\}\langle 110 \rangle$  textures [91].

Kolahi et al. examined the microstructure evolution of interstitial free (IF) steel processed through hot rolling, followed by accumulated roll bonding (ARB). The microstructural refinement of IF steel through ARB and warm rolling displayed comparable trends, with minor distinctions. Initially equiaxed grains deformed into elongated structures with increasing strain, developing substructures, and evolving into ultrafine grains, especially under higher strains. Hot roll bonding led to more uniform grain refinement across the sample, attributed to its repeated layering and complex strain paths [92].

## 2.4 Research gaps

After an extensive literature survey on the topic of formability of a multiple ply clad laminated sheets, it has been found that the following issues have not been attempted so far:

1. Several analytical models for deep draw force sheet materials are available in literature, still there is a lack of analytical models of deep draw force using anisotropic yielding criteria for clad sheet metals, incorporating the anisotropy of individual parent sheet.
2. Effect of individual sheets on deep drawability and drawing force at elevated temperature for a 2-ply laminate composite has not been explored to the fullest.
3. Although several stress-strain curves for parent metals have been published at elevated temperatures, the behaviour of the composite laminate, due to interfacial interactions, remains largely unknown throughout temperature ranges.

4. Residual stresses, bonding quality, and mismatched coefficients of thermal expansion can all influence the mechanical performance of 2-ply laminates. These impacts are rarely measured experimentally.
5. Although various numerical simulations have been performed to investigate the influence of individual layer thickness and stacking sequence on the thinning, strain distribution, forming limit curves, limit drawing ratio, and thickness distribution at room temperature, an elaborate investigation at elevated temperatures is required.

## 2.5 Research objectives

Suitable grades of 2-ply clad of stainless steel and aluminium alloy are chosen as per the application in the automotive components, aerospace sheet metal parts, utensils for domestic usage etc. involving deep drawing operations. Forming such laminated composite sheets is inherently complex due to the differing mechanical and thermal properties of the constituent materials. Understanding the effects of both process parameters and material characteristics becomes crucial, especially under elevated temperature conditions. Considering these challenges and the research gaps, the objectives of the present research are presented as below:

1. Characterization of tensile properties of 2-ply laminate composite sheet metal and its individual parent sheets at ambient and elevated temperatures.
2. Development of an analytical model for prediction of punch force in deep drawing operation with incorporation of anisotropy of individual sheets.
3. Finite element analysis of Deep drawing operation at ambient and elevated temperatures.

4. Experimental validation of Deep draw force, Limiting Draw ratio, Forming Limit diagram of a 2-ply laminate composite sheet metal and its individual parent sheets at ambient and elevated temperatures.

## CHAPTER 3

### DEVELOPMENT OF ANALYTICAL MODEL

The analytical model is developed to predict the required punch force in the deep drawing of the two-ply clad sheet based on the Barlat-89 anisotropic yield criterion [93], which accommodates different value of material parameter for distinct materials in combination. Fig. 3.1 illustrates the various regions in a circular blank during the deep drawing process. During this process, the sheet undergoes different stress states across different regions. In the flange region, radial tension and circumferential compression occur as the material is drawn inward, causing a slight increase in thickness. The cup wall region is under tension in both directions, leading to thinning, which is most pronounced near the punch corner radius. In the punch bottom region, the sheet wraps around the punch and undergoes tensile stresses in both directions, but the thickness remains nearly unchanged.

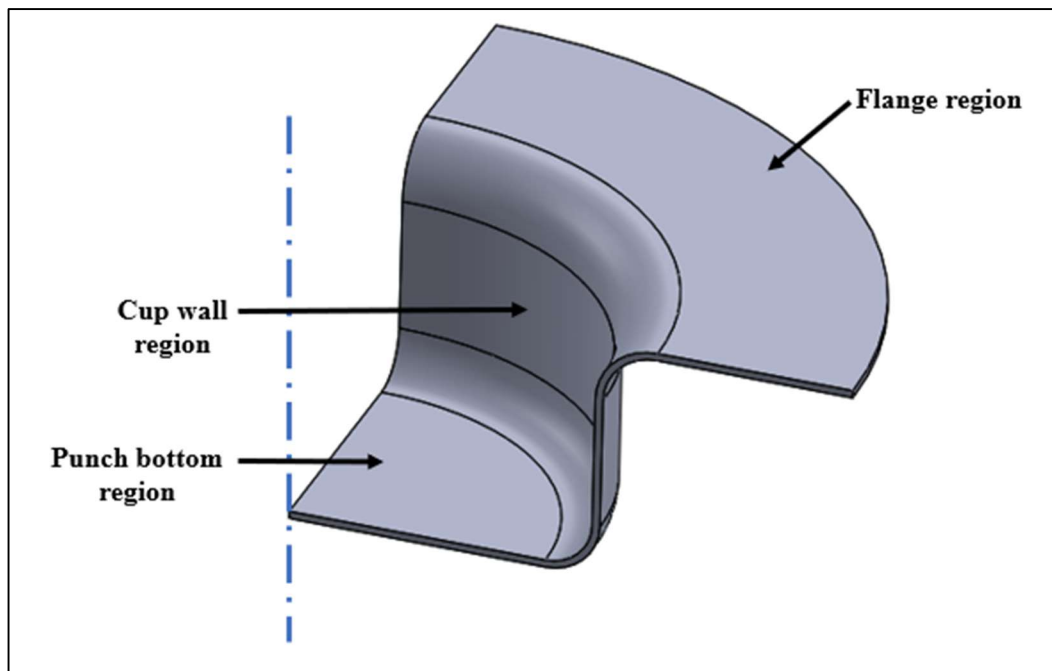


Fig. 3.1 A quarter segment of a circular blank in deep drawing operation.

The analytical model has been developed based on the following assumptions to determine the punch force for the deep drawing of the 2-ply clad sheet:

1. Plane stress condition and plane strain condition (thickness strain,  $\varepsilon_z = 0$ ) is assumed in the flange region.
2. Planar isotropy is assumed ( $R_0 = R_{90} = R$ ).
3. Blank holding pressure is assumed to be acting only on the outer rim.

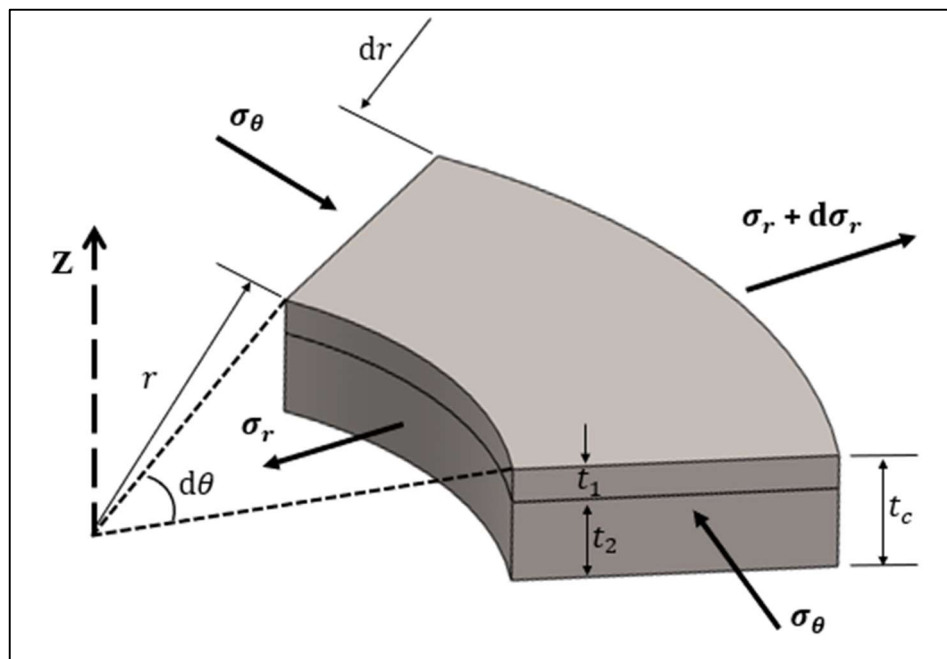


Fig. 3.2 Radial element in the flange region of the sheet during deep drawing

A radial element in the flange region, as shown in Fig. 3.2, with the radial and tangential directions as the principal directions. Where  $t_1$  and  $t_2$  are the layer thicknesses of individual sheets,  $\sigma_{ri}$  and  $\sigma_{\theta i}$  are radial and tangential stresses acting on the layer,  $t_c$  is the layer thickness of the clad sheet, and  $\sigma_{rc}$  is the radial stress acting on the clad.

Now the condition of force equilibrium on the element of layer 1 in flange region, is expressed by:

$$\frac{t_1}{r}(\sigma_{r1} + \sigma_{\theta1}) + t_1 \frac{d\sigma_{r1}}{dr} = 0 \quad (3.1)$$

The condition of force equilibrium on the element of layer 2 in flange region, is expressed by:

$$\frac{t_2}{r}(\sigma_{r2} + \sigma_{\theta2}) + t_2 \frac{d\sigma_{r2}}{dr} = 0 \quad (3.2)$$

The combined force equilibrium equation for the 2-ply clad sheet can be expressed by combining the above two equations of individual components, which is given as:

$$\frac{d(t_1\sigma_{r1})}{dr} + \frac{d(t_2\sigma_{r2})}{dr} + \frac{t_1}{r}(\sigma_{r1} + \sigma_{\theta1}) + \frac{t_2}{r}(\sigma_{r2} + \sigma_{\theta2}) = 0 \quad (3.3)$$

The radial flow stress in the clad sheet can be estimated by the rule of mixtures, an average of flow stresses in the individual components weighted by volume fractions, which is expressed as follows:

$$t_c\sigma_{rc} = (t_1\sigma_{r1} + t_2\sigma_{r2}) \quad (3.4)$$

Substituting the radial flow stress of the clad sheet, estimated by the rule of mixtures (Eq. 3.4) into the force equilibrium equation of the radial element of the clad sheet (Eq. 3.3), we get:

$$\frac{d(t_c\sigma_{rc})}{dr} + \frac{1}{r}[t_1(\sigma_{r1} + \sigma_{\theta1}) + t_2(\sigma_{r2} + \sigma_{\theta2})] = 0 \quad (3.5)$$

Here, considering Barlat & Lian 1989 anisotropic yield criterion for plane stress condition, represented in terms of principal stresses is expressed as-

$$|k_1 + k_2|^a + |k_1 - k_2|^a + \frac{c}{2-c} |2k_2|^a = \frac{2}{2-c} \bar{\sigma}^a \quad (3.6)$$

$$\text{where, } k_1 = \frac{\sigma_1 + h\sigma_2}{2} \quad k_2 = \frac{\sigma_1 - h\sigma_2}{2}$$

$$c = 2 \left( \sqrt{\frac{R_0}{1+R_0} \frac{R_{90}}{1+R_{90}}} \right) \quad h = \sqrt{\frac{R_0}{1+R_0} \frac{1+R_{90}}{R_{90}}}$$

Here  $\sigma_1$  and  $\sigma_2$  are the principal stresses,  $\bar{\sigma}$  is the effective stress associated with the



uniaxial flow stress, and,  $a$  is the material parameter which is assigned a specific integer value based on the material's crystal lattice. It was suggested to consider the value of the material parameter to be 6 and 8 for BCC and FCC metals, respectively. Considering planar isotropy ( $R_0 = R_{90} = R$ ), the constants  $c$  and  $h$  simplifies as follows:

$$c = \frac{2R}{1+R} \quad h = 1$$

The stress tensor invariants  $k_1$  and  $k_2$  are simplified as follows:

$$k_1 = \frac{\sigma_1 + \sigma_2}{2} \quad ; \quad k_2 = \frac{\sigma_1 - \sigma_2}{2}$$

So, for the planar isotropy ( $h = 1$ ), the simplified expression for Barlat-89 yield criterion will be written as:

$$f \equiv |\sigma_1|^a + |\sigma_2|^a + \frac{c}{2-c} |\sigma_1 - \sigma_2|^a = \frac{2}{2-c} \bar{\sigma}^a \quad (3.7)$$

Now, for the yield criterion, the associated flow rule relates the stresses to the plastic strain increment as per the Levy-Mises equation stated below:

$$d\varepsilon_{ij} = d\lambda \frac{\partial f}{\partial \sigma_{ij}} \quad (3.8)$$

where,  $\lambda$  is the plastic multiplier and  $f$  is the plastic potential, defined as a scalar function described by the yield criterion.

The flow rule combined with the yield criterion (Eq. 3.7) can be written as:

$$\frac{d\varepsilon_1}{|\sigma_1|^{a-1} + \frac{c}{2-c} |\sigma_1 - \sigma_2|^{a-1}} = \frac{d\varepsilon_2}{|\sigma_2|^{a-1} - \frac{c}{2-c} |\sigma_1 - \sigma_2|^{a-1}} = \frac{d\bar{\varepsilon}}{\frac{2}{2-c} \bar{\sigma}^{a-1}} \quad (3.9)$$

where,  $d\varepsilon_1$  and  $d\varepsilon_2$  are the plastic strain incremental components along the principal directions.  $d\bar{\varepsilon}$  is the effective strain increment.

The radial element of the blank in the flange region has stresses in two principal

directions, i.e., the tensile radial stress ( $\sigma_r$ ) pulling the material inwards and the compressive circumferential stress ( $\sigma_\theta$ ) responsible for reduction of blank diameter.

Substituting the principal stresses in the flow rule (Eq. 3.9) with,

$$\sigma_1 = \sigma_r, \text{ and}$$

$$\sigma_2 = -\sigma_\theta \text{ (Compressive in nature),}$$

and further simplifying the flow rule we will get the following expression:

$$\sigma_r + \sigma_\theta = \bar{\sigma} \left( \frac{d\varepsilon_r - d\varepsilon_\theta}{d\bar{\varepsilon}} \right)^{\frac{1}{a-1}} \cdot \frac{1}{c^{\frac{1}{a-1}}} \quad (3.10)$$

The effective strain increment can be calculated using the incremental plastic work per unit volume as:

$$\bar{\sigma} d\bar{\varepsilon} = \sigma_1 d\varepsilon_1 + \sigma_2 d\varepsilon_2 + \sigma_3 d\varepsilon_3 \quad (3.11)$$

Considering the principal strains as radial strain ( $\varepsilon_r$ ), circumferential strain ( $\varepsilon_\theta$ ) and thickness strain ( $\varepsilon_z$ ),

$$d\varepsilon_1 = d\varepsilon_r; \quad d\varepsilon_2 = d\varepsilon_\theta; \quad d\varepsilon_3 = d\varepsilon_z = 0 \text{ (thickness strain)}$$

Also, considering the volume constancy during the material flow, and ignoring the thickness variation leads to:

$$d\varepsilon_r = -d\varepsilon_\theta \quad (3.12)$$

then, the effective strain using Eq. (3.10) to Eq. (3.12), can be written as follows:

$$\bar{\varepsilon} = \left( \frac{2}{c} \right)^{\frac{1}{a}} \cdot \varepsilon_r \quad (3.13)$$

Considering the power law of hardening  $\bar{\sigma} = K \cdot \bar{\varepsilon}^n$ , where  $K$  and  $n$  are the strength coefficient and strain hardening exponent, respectively. The effective stress in a plane strain condition can be written as  $\bar{\sigma} = K' \cdot \bar{\varepsilon}^n$ , where  $K'$  is the strength coefficient in plane strain condition, which is expressed as [94]:

$$K' = K \left( \frac{4}{3} \right)^{\frac{n+1}{2}} \quad (3.14)$$

Considering the power law of hardening in plane strain condition  $\bar{\sigma} = K' \cdot \bar{\epsilon}^n$  and using Eq. (3.10) and Eq. (3.13), we get:

$$(\sigma_r + \sigma_\theta) \left( \frac{d\bar{\epsilon}}{d\epsilon_r - d\epsilon_\theta} \right)^{\frac{1}{a-1}} \cdot c^{\frac{1}{a-1}} = K' \cdot \left[ \left( \frac{2}{c} \right)^{\frac{1}{a}} \cdot \epsilon_r \right]^n$$

Simplifying the above equation, we get:

$$(\sigma_r + \sigma_\theta) = K' \cdot \left( \frac{2}{c} \right)^{\frac{n-1}{a} + \frac{1}{a-1}} \cdot \epsilon_r^n \quad (3.15)$$

The radial stress in the clad sheet in the flange region is obtained by using Eq. (3.5) and Eq. (3.15), which is expressed as follows:

$$\sigma_{rc} = \frac{1}{t_c} \int_{r_0}^r \frac{1}{r} \{ t_1(\sigma_{r1} + \sigma_{\theta1}) + t_2(\sigma_{r2} + \sigma_{\theta2}) \} dr \quad (3.16)$$

The total radial stress on the element in the flange region is evaluated by integrating Eq. (3.16) from the initial blank radius  $r_0$  to the instantaneous blank radius  $r$ , with the boundary conditions,  $\sigma_{rc} = \frac{\mu_{avg} * F_{bh}}{2\pi r_0 t_c}$ , at  $r = r_0$  (initial blank radius). The radial stress in the blank at the start of the deep drawing process is equal to the frictional force acting on the outer rim of blank occurring at the blank-die contact and blank-holder contact. The friction coefficient  $\mu_{avg}$ , is the average of the friction coefficient of both the top and bottom surfaces of the clad sheet.

The total radial stress in the 2-ply clad sheet is expressed as:

$$\sigma_{rc} = \frac{M_1 \left( \ln \frac{r_0}{r} \right)^{n_1+1}}{n_1+1} + \frac{M_2 \left( 1 - \frac{r_0}{r} \right)^{n_2+1}}{n_2+1} + \frac{\mu_{avg} * F_{bh}}{2\pi r_0 t_c} \quad (3.17)$$

where,  $F_{bh}$  is the blank holding force,

$$\mu_{avg} = \frac{(\mu_1 + \mu_2)}{2},$$

$$M_1 = \frac{t_1}{t_c} K'_1 \left( \frac{2}{c_1} \right)^{\frac{n_1-1}{a_1} + \frac{1}{a_1-1}}, \text{ and}$$

$$M_2 = \frac{t_2}{t_c} K'_2 \left( \frac{2}{c_2} \right)^{\frac{n_2-1}{a_2} + \frac{1}{a_2-1}}.$$

The radial stress in the flange region is transferred to the cup wall stress ( $\sigma_{wc}$ ) through the die corner radius. The material undergoes bending and unbending at the die corner radius. The bending and unbending of the sheet along the die corner can be compared to the analogy of the motion in belt and pulley. The wall stress,  $\sigma_{wc}$ , is written as:

$$\frac{\sigma_{wc}}{\sigma_{rc}} = e^{\mu_{avg} \cdot \frac{\pi}{2}} \quad (3.18)$$

The total punch force,  $F_{dr}$ , required to deep draw a circular blank into a cup of radius  $r_p$ , is estimated by the total force induced in the cup wall region due to the wall stresses resisted by the cross-sectional area of the cup, which is expressed by:

$$F_{dr} = \sigma_{wc} \cdot 2\pi r_p t_c, \text{ where } r_p \text{ is the punch radius.} \quad (3.19)$$

Combining Eq. (3.17) to Eq. (3.19), the expression for the required punch force during deep drawing is obtained as:

$$F_{dr} = 2\pi r_p t_c \cdot e^{\mu_{avg} \cdot \frac{\pi}{2}} \cdot \left[ \left\{ \frac{t_1}{t_c} K'_1 \left( \frac{2}{c_1} \right)^{\frac{n_1-1}{a_1} + \frac{1}{a_1-1}} \frac{(\ln \frac{r_0}{r})^{n_1+1}}{n_1+1} \right\} + \right. \\ \left. \left\{ \frac{t_2}{t_c} K'_2 \left( \frac{2}{c_2} \right)^{\frac{n_2-1}{a_2} + \frac{1}{a_2-1}} \frac{(\ln \frac{r_0}{r})^{n_2+1}}{n_2+1} \right\} + \frac{\mu_{avg} \cdot F_{bh}}{2\pi r_0 t_c} \right] \quad (3.20)$$

The total punch force required to draw a blank of radius  $r_0$ , into a cylindrical cup of radius  $r_p$ , is determined by Eq. (3.20). The developed analytical model incorporates the Barlat-89 yield surface criterion, using material parameter,  $a$ , which is having an

integer value dependent on material crystal structure. In the present work the SS/AA 2-ply clad sheet is being considered, for which the parameter,  $a$ , has a value of 6 for stainless steel layer as it has BCC structure, and 8 for aluminium layer which is having FCC structure. The previously developed analytical models as discussed in literature review section used common value of,  $a = 2$ , for all materials irrespective of the crystal structure. Also, the present developed model incorporates the constant,  $c$ , which represents the anisotropy of material, and the strain hardening exponent,  $n$ , for each individual constituent layers separately.

## CHAPTER 4

### PREDICTION OF PUNCH FORCE IN DEEP DRAWING PROCESS BY FINITE ELEMENT METHOD

The Finite Element Method (FEM) is a numerical approach used to solve problems defined by partial differential equations. It divides a complex domain into smaller, simpler parts called finite elements, over which the solution is approximated using an interpolation function or a shape function defined at nodal points. FEM possesses several distinctive features that make it one of the most powerful and versatile numerical techniques for solving engineering and scientific problems. One of its primary features is the piecewise approximation of physical fields, in which the complex geometry of a continuum is divided into smaller, manageable finite elements [95]. This local approximation capability allows FEM to model irregular geometries and complex boundary conditions more effectively than traditional analytical methods. Another key feature is the locality of formulation, which leads to the generation of sparse and well-structured system matrices. Because each element only interacts with its neighbouring elements through shared nodes. Additionally, FEM offers flexibility in handling different material properties, loading conditions, and geometries, making it applicable to a wide range of problems in structural mechanics, heat transfer, fluid flow, and electromagnetics.

FEM involves a systematic sequence of steps to approximate the solution of complex engineering problems. The process begins with discretization, where the entire domain is divided into a finite number of smaller subregions called elements, interconnected at nodes. This network of elements forms the finite element mesh, which serves as the foundation for numerical analysis. Suitable interpolation functions, usually

polynomial, are then selected to represent the variation of field variables within each element. In the next step, the element properties are derived by formulating element equations using methods such as the variational or Galerkin approach [96]. These individual element equations are then assembled into a global system of equations, and appropriate boundary conditions are applied. The global equation system, typically sparse and symmetric, is then solved to obtain the nodal values of the unknown field variables. Finally, in the post-processing stage, additional quantities such as strains, stresses, or temperature gradients are computed, and the results are visualized for analysis.

#### **4.1 About the software**

In the present study, the simulations of deep drawing of the clad sheet are performed using ABAQUS (version 6.14) software. ABAQUS- Explicit solution procedure is applied for the simulation of material flow in flange region, bending and unbending in the die corner radius region, and, plastic deformation in the cup wall region. The explicit method is capable of overcoming the convergence issues faced during solving the non-linear simulation.

#### **4.2 Modelling and simulations of deep drawing process**

The current work considers the deep drawing process of clad sheet as a non-linear problem. In general, nonlinearity can originate from three sources: nonlinearity in the material, nonlinearity in the boundary, and nonlinearity in the geometry. The presence of more than one metal in a clad sheet, along with the anisotropic behaviour makes the material non-linear. Also, the material behaviour is non-linear in the plastic region, attributed to the strain hardening of the material.

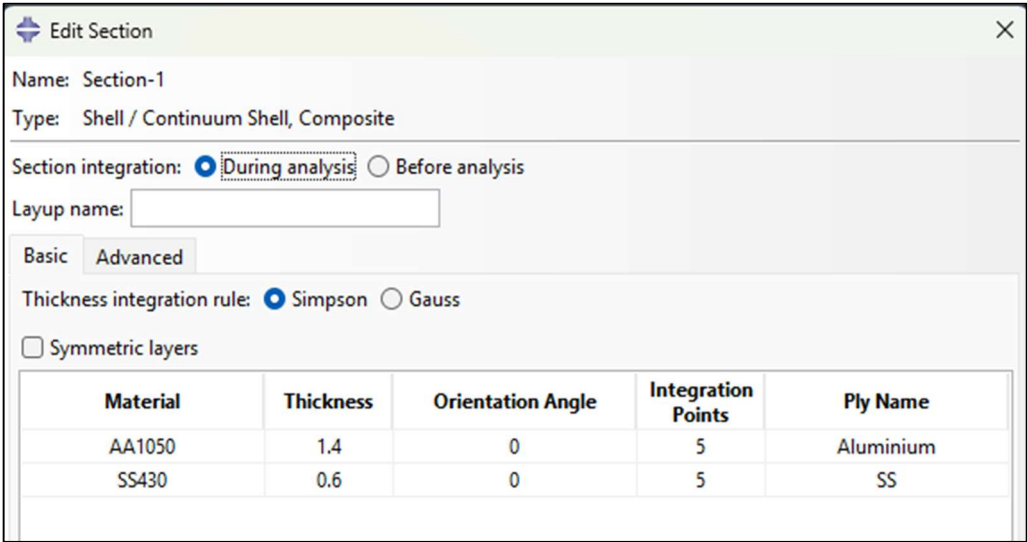
As with the forming process, boundary nonlinearity results from changes in the boundary conditions. The sheet metal is first placed on the die during the deep drawing operation, allowing just the bottom surface of the sheet metal to come into contact with the die surface. The top surface of the sheet metal comes into contact with the blank holder bottom surface and locks the sheet. Punch travels and makes contact with the upper surface of the sheet metal to draw it into the die cavity; the material then undergoes plastic deformation. Contact boundary conditions cause a significant and instantaneous change in the model's response when a contact happens during a simulation, leading to non-linearity. The third cause of nonlinearity has to do with how a model's geometry evolves as it is being analysed. When a sheet of metal is undergoing bending and unbending at die corner radius, it deforms significantly and the punch force is not parallel to the bent sheet. The presence of non-linearity in the model results in the requirement of numerous increments. For these reasons, ABAQUS-Explicit is a suitable fit for non-linear analysis.

In order to understand the influence of the temperature and lubrication condition on the required punch force for deep drawing of the 2-ply clad sheet of stainless steel and aluminium, simulations were performed by incorporating different material model for different temperatures. The results of the FEA are compared with the developed analytical model and experimental results.

A quarter symmetric 3D model is created, with a dynamic explicit step that overcomes the convergence issues faced during solving the non-linear simulation. The blank is modelled as a deformable member with a continuum shell composite section, with defined shell thickness for each layer separately as shown in Fig. 4.1. The aluminium layer with 1.4 mm thickness is the top layer that comes in contact with the punch,



whereas the stainless steel layer is the bottom layer having a thickness of 0.6 mm. For simulation, the value for thickness integration by Simpson rule with five points integration was used for both the constituent layers individually. Three types of integration schemes like the Gauss, Simpson, and Lobatto integration methods are suggested for use in Finite Element simulations. The integration scheme and integration sites across sheet thickness determine the prediction of formability [97]. Many researchers have demonstrated in their investigations that the accuracy of formability prediction is unaffected by the inclusion of more than 5 to 7 integration points [98,99]. Because formability is a function of stretching moment, which is a function of stress distribution in sheet thickness, shell elements necessitate numerical integration of stress and strain through thickness in order to calculate the force required for plastic deformation [100]. The Simpson rule with five integration points for each constituent layer method was chosen since the number of integration points directly impacts the simulation time.



**Edit Section**

Name: Section-1

Type: Shell / Continuum Shell, Composite

Section integration: ☒ During analysis ☐ Before analysis

Layup name:

Basic **Advanced**

Thickness integration rule: ☒ Simpson ☐ Gauss

☐ Symmetric layers

Material	Thickness	Orientation Angle	Integration Points	Ply Name
AA1050	1.4	0	5	Aluminium
SS430	0.6	0	5	SS

Fig. 4.1 Shell section modelled for clad sheet

The blank is meshed as a combination of a 4-node doubly curved quadrilateral shell element with reduced integration and hourglass control (S4R) at the outer regions that

is in contact with the die and the blank holder and the central region which is in the contact with the punch surface is meshed as a 3-node triangular shell element with reduced integration and hourglass control (S3R) as shown in Fig. 4.2. The meshing is divided in above mentioned two regions, so as to avoid the higher rotation of the elements in the blank at the die corner radius region, and the punch center region. At the die corner radius region, non-linearity prevailed due to the bending and unbending of the sheet, leading to errors caused by higher rotation of elements. This is overcome by using quadrilateral-dominated elements with a sweep pattern having a finer mesh size. But the quadrilateral elements would converge all the elements at a single point at the punch center, where the aspect ratio of the elements would become very high, which would again lead to error due to the higher rotation of elements in this region. To overcome this error, a free meshing technique using a combination of both triangular and quadrilateral elements is employed in the region where the blank is in contact with the punch bottom.

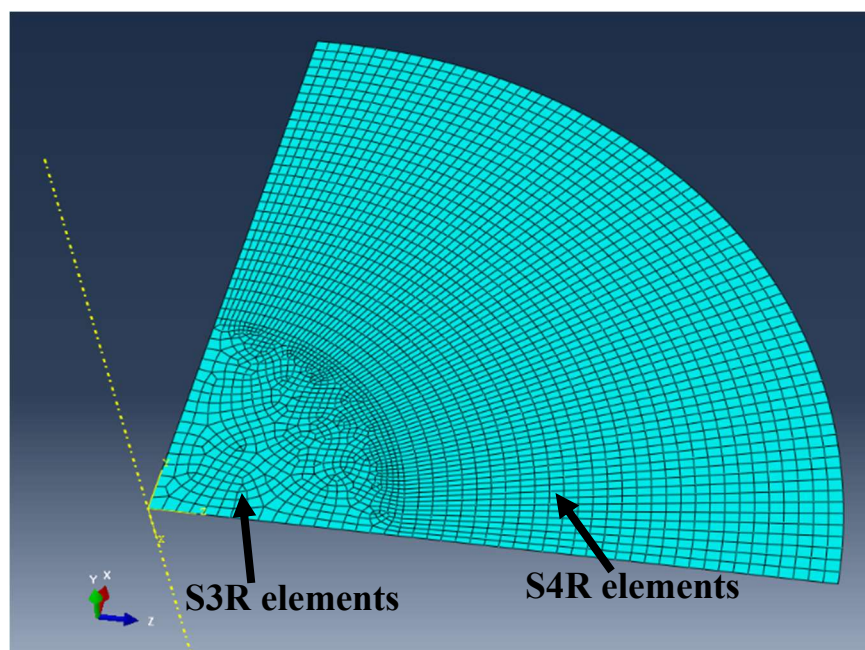


Fig. 4.2 Meshed blank with shell section

The material model is defined by providing the plastic region data acquired from the experimental tensile test data of individual constituent layers. In the present research, convergence studies are conducted by gradually increasing the mesh density and observing the changes in the results. Convergence studies are helpful in determining the optimal mesh size for accurate results. The mesh refining process is continued until the results no longer change significantly.

Table 4.1 shows the details of elements and nodes for a 100 mm diameter blank of clad material used in the present investigation. The blank diameter is varied to determine the limiting draw ratio for a given material model for any specific temperature and lubrication condition.

Table 4.1 Details of elements and nodes for the simulations of 100 mm diameter blank.

Total number of nodes	3174
Total number of elements	3100
Linear quadrilateral elements	3074
Linear triangular elements	26

The die, blank holder and punch are the non-deformable members that are also the tools to perform the forming operation, and are modelled as discrete rigid members. Furthermore, discrete rigid parts are allocated with coarse meshing in the quarter symmetric model to reduce the simulation time. The die and the blank holder are meshed as the linear quadrilateral R3D4 (3-node bilinear quadrilateral rigid) elements, whereas the punch is meshed as a combination of the linear quadrilateral R3D4 and the linear triangular R3D3 (3-node triangular rigid) elements. The punch is designed with profile radius of 5 mm, the die with a corner radius of 10 mm, and the blank holder with a radius of 10 mm. A finer mesh size of the elements in the profile radius

region in all the tools is used, in order to avoid the excessive rotation of the blank due to bending and unbending in the region. A quarter-symmetric 3D assembly model of a deep drawing setup, with all tools modelled using ABAQUS explicit, is depicted in Fig. 4.3.

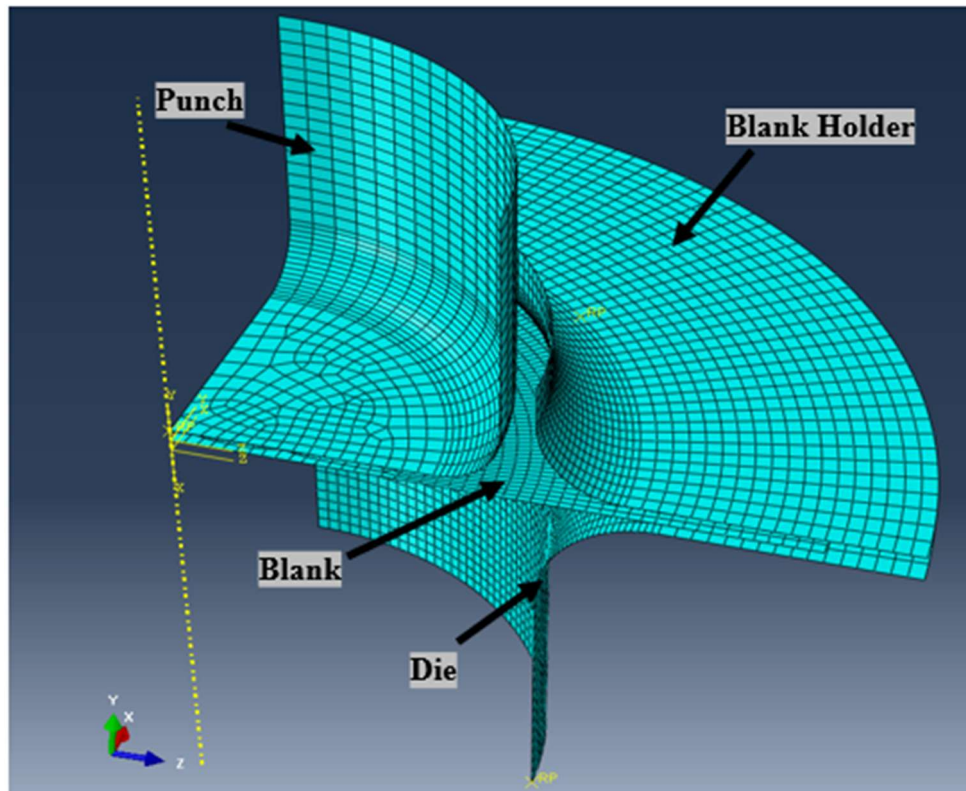


Fig. 4.3 A quarter symmetric 3D model of deep drawing assembly.

### 4.3 Material model

The stress strain behavior in the plastic regime of a material reveal key aspects of its nonlinear response. Elastic strains correspond to reversible deformation, while plastic strains are associated with permanent deformation. The true stress vs true strain curve obtained from a uniaxial tensile test clearly shows that the sheet material undergoes uniform plastic deformation between the yield point and the ultimate tensile strength. During this stage, strain hardening follows the power-law relationship  $\sigma = K \epsilon^n$  where  $n$  is the strain-hardening exponent and  $K$  is the strength coefficient.

Also, most sheet metals exhibit anisotropy, typically characterized by the plastic strain ratio ( $r$  - value), which quantifies directional differences in plastic flow. This anisotropy is often incorporated into finite element models to more accurately simulate the material's behaviour. Hill's plasticity model, also known as Hill's 1948 yield potential, is an extension of the Mises yield function for anisotropic materials. Abaqus uses the six anisotropic yield stress ratios,  $R_{11}$ ,  $R_{22}$ ,  $R_{33}$ ,  $R_{12}$ ,  $R_{13}$  and  $R_{23}$ , to incorporate the anisotropy into the finite element analysis. The six yield stress ratios are given by the material's yield stresses along the rolling, transverse, thickness, and diagonal directions [101].

For the sheet metals, the yield stress in the thickness direction is difficult to determine. Therefore, using the following formulas, the anisotropy yield stress ratios are calculated using equation below:

$$R_{11} = R_{12} = R_{23} = 1 \quad (4.1)$$

$$R_{22} = \sqrt{\frac{R_{90} (R_0 + 1)}{(R_0 + R_{90})}} \quad (4.2)$$

$$R_{33} = \sqrt{\frac{R_{90} (R_0 + 1)}{R_0 (1 + R_{90})}} \quad (4.3)$$

$$R_{13} = \sqrt{\frac{3 R_{90} (R_0 + 1)}{(R_0 + R_{90})(1 + 2R_{45})}} \quad (4.4)$$

where,  $R_0$ ,  $R_{45}$  and  $R_{90}$  are the experimentally obtained plastic strain ratios for the specimens orientated with respect to the rolling direction at  $0^\circ$ ,  $45^\circ$ , and  $90^\circ$ . The experimentally obtained values of anisotropy yield stress ratios for the SS430 and AA1050 constituent materials at room temperature,  $180^\circ\text{C}$ ,  $220^\circ\text{C}$  and  $300^\circ\text{C}$ , are presented in Table 4.2. The elastic and plastic properties of the material, along with

the anisotropy ratio is assigned to the geometry in the simulation, as shown in Fig. 4.4.

The plastic behaviour is incorporated in the model using the experimental stress and strain data from the yield point to the ultimate tensile strength, for each temperature.

Table 4.2 Anisotropy yield stress ratios for the constituent materials at different temperatures.

Temperature	Material	R <sub>11</sub>	R <sub>22</sub>	R <sub>33</sub>	R <sub>12</sub>	R <sub>13</sub>	R <sub>23</sub>
Room Temperature	SS430	1	1.023260	1.076978	1	0.936710	1
	AA1050	1	0.851782	0.876038	1	1.087627	1
180°C	SS430	1	1.072230	1.029297	1	0.867792	1
	AA1050	1	0.955118	1.013991	1	1.158250	1
220°C	SS430	1	1.212338	1.010861	1	0.992077	1
	AA1050	1	0.970440	1.015895	1	1.076055	1
300°C	SS430	1	1.175296	0.993955	1	0.890989	1
	AA1050	1	0.987763	1.014145	1	1.026103	1

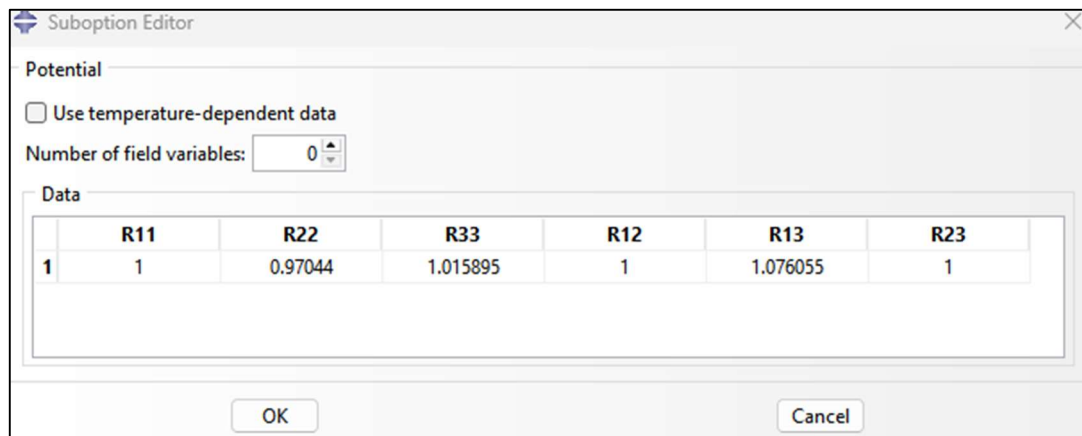


Fig. 4.4 The anisotropy ratios incorporated in the material properties in Abaqus.

7

#### 4.4 Contact and boundary conditions in simulations.

In the assembly module, the specimen for deep drawing is placed on the encastered die in such a way that SS430 is in contact with the die surface, which is also the outer surface of the formed cup. The AA1050 is the top surface of the 2-ply sheet facing the punch and is thus, the inner layer. Fig. 4.5 illustrates the edges of the shell blank are assigned boundary condition of X-symmetry and Z-symmetry to maintain the axisymmetry conditions of the quarter model of blank.

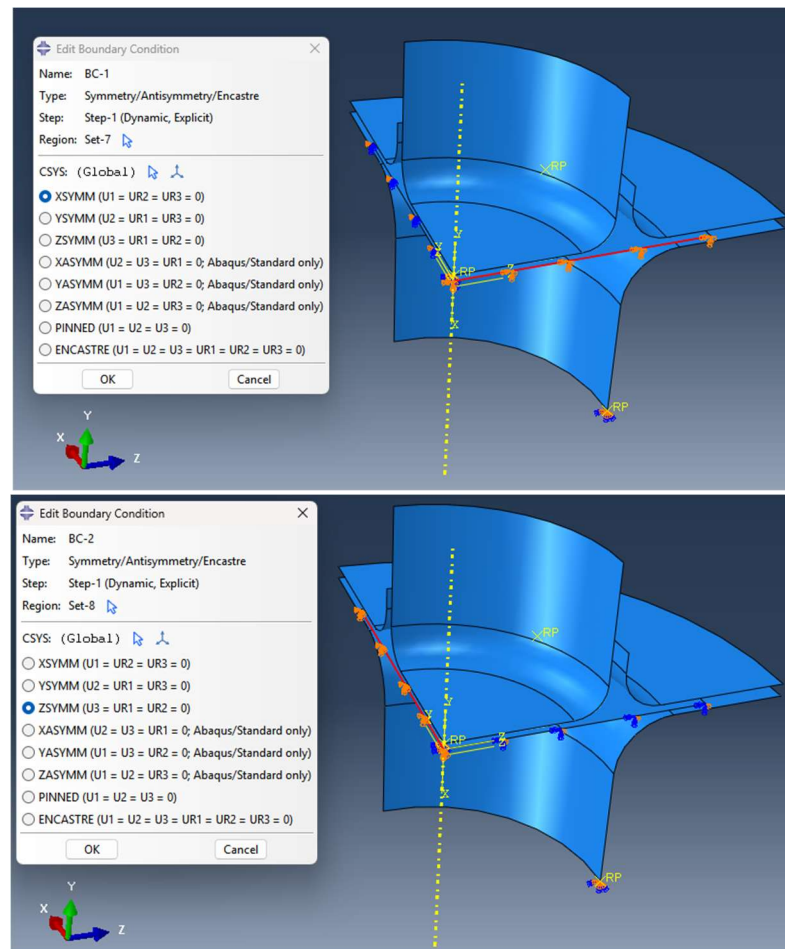


Fig. 4.5 X-symmetry and Z-symmetry boundary condition assigned to blank.

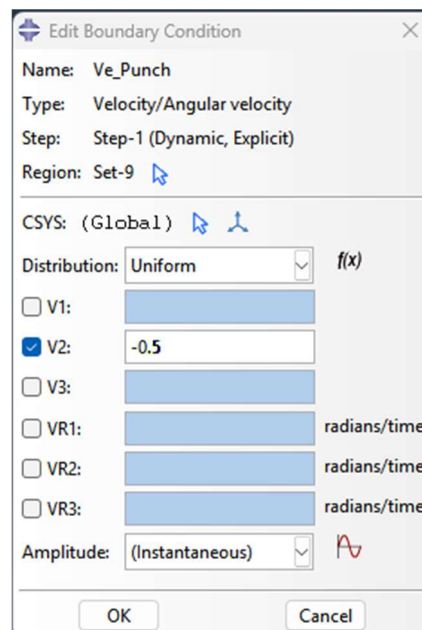


Fig. 4.6 Velocity provided to the punch.



7

The blank holder holds the blank specimen from top which applies a holding force of about 2-3 kN, in order to avoid wrinkling. The die, holder and the punch surfaces are defined as the master surfaces and the deformable blank is the slave surface. Before running the simulation for analysis, a gap equal to blank thickness of the clad sheet was provided between the holder and die where middle surface of the shell was considered. The punch travel in the negative Y direction with a velocity of 0.5 mm/s as shown in Figure 4.6.

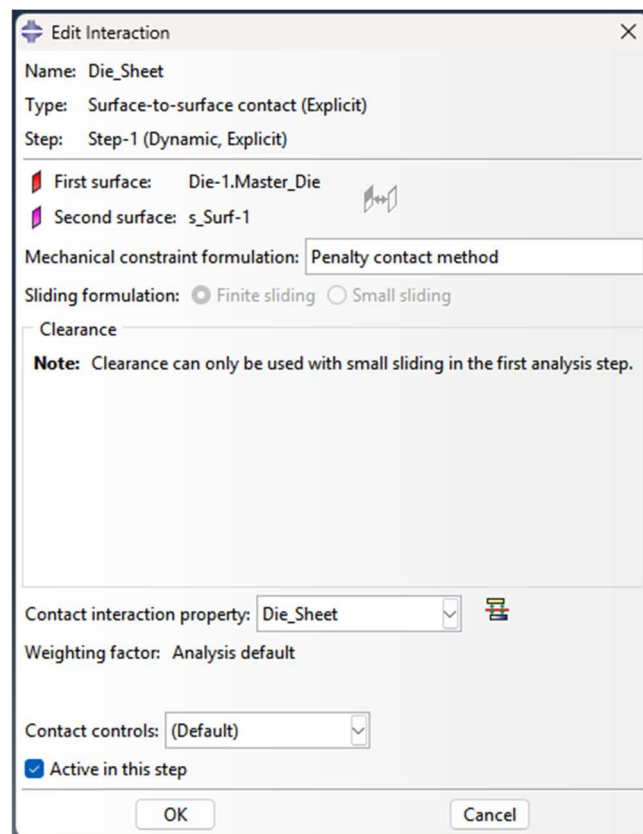


Fig. 4.7 Interaction properties defined for the surfaces in contact.

7

A pair of different contact properties are established by defining the surface-to-surface contact between the tools and the blank, with friction formulated as penalty contact method by assigning a coefficient of friction value at the interface of tools and blank, as shown in Fig 4.7. The friction between the tools and blank interface at different



temperature and lubricating conditions is taken from the experimental results of coefficient of friction for both SS430 and AA1050 in contact with die steel. The experimental results of coefficient of friction is shown in Table 4.3 for both the materials.

Table 4.3 Variation of Coefficient of friction on the SS side and AA side of the clad specimen at different temperatures under different lubrication condition.

Temperature (°C)	SS430		AA1050	
	No Lubrication	MoS <sub>2</sub> Lubrication	No Lubrication	MoS <sub>2</sub> Lubrication
RT	0.08	0.06	0.12	0.09
180°C	0.10	0.06	0.19	0.10
220°C	0.17	0.09	0.31	0.11
300°C	0.21	0.10	0.42	0.13

## CHAPTER 5

### EXPERIMENTAL PROCEDURE

The following section discusses the experimental methodology to determine the tensile properties and the formability of the 2-ply clad sheet at different temperatures. The tensile properties and the anisotropy of the clad sheet and the constituent layers are determined at ambient and elevated temperatures. The formability of the clad sheet is analysed by determining the forming limit diagram and the limiting draw ratio in deep drawing process, at different temperatures and lubrication condition. The experimental results of punch force are compared with the analytical and numerical predictions. The comparison of the microstructure evolution of the clad sheet interface due to deformation at different temperatures is analysed through electron back scatter technique.

#### 5.1 Material selection

Clad sheets are increasingly favoured for their superior formability, heat transfer efficiency, and uniform heating, making them ideal for use in cookware and heat exchangers. In the present investigations, a commercially available two-ply clad sheet consisting of 0.6 mm thick stainless steel SS430 and 1.4 mm thick aluminium AA1050 as constituent layers, is procured in an annealed condition. The aluminium AA1050 is clad with SS430 which is a corrosion and heat-resistant ferritic grade steel.

The spark-based spectroscopy revealed the chemical composition of elements present in both the materials of the clad sheet, and the results are shown in Table 5.1. In this method, a spark is created on the sample which results in rapid heating causing vaporization on its surface which further produces plasma assisted spectrums from the element present in the sample. Then, a machine compares the amount of light from the

sample to that of known standards to identify the element, and calculates the quantity of that element.

Table 5.1. Chemical constituent's results obtained by spark-based spectroscopy.

Chemical Composition (in % wt.)	C	Al	Cr	Ni	Sn	Si	Mn	V	Fe
SS430	0.07	0.004	16.09	0.22	0.02	0.29	0.4	0.05	Rest
AA1050	-	Rest	0.01	0.03	0.01	0.06	0.01	0.01	0.21

## 5.2 Determination of mechanical properties

### 5.2.1 Characterisation of tensile properties

To determine the tensile properties of 2-ply clad sheet metals, the specimens for uniaxial tension test are cut through CO<sub>2</sub>-Laser cutting machine, as shown in Fig 5.1.

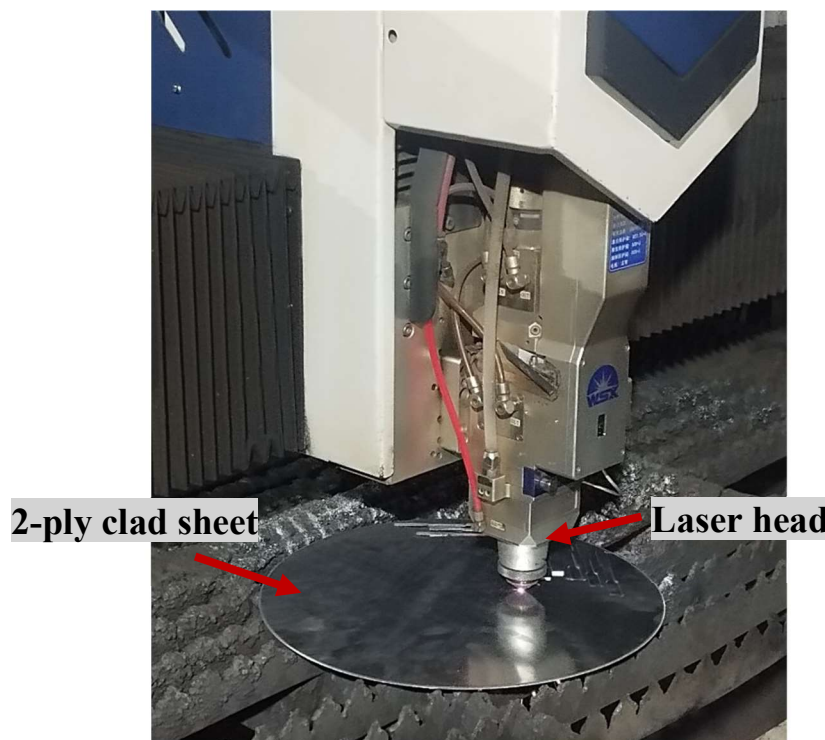


Fig. 5.1 Laser cutting of tensile samples in progress

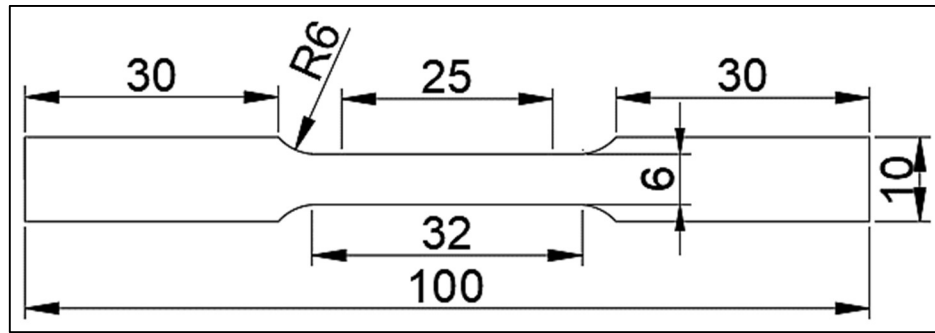


Fig. 5.2 Size description of sub size sample of tensile test as per ASTM E8M standard  
(All dimensions are in mm)

The specimens are prepared along the rolling direction of the clad sheet as per the ASTM-E8M standard as shown in Fig 5.2. Tensile properties are determined for the clad sheet and also for the both constituent layers. The tensile samples of stainless steel layer is claimed from 2-ply clad sheet by dissolving aluminium layer, a required set of the tensile samples are immersed in a glass beaker containing a solution of sodium hydroxide. To claim the aluminium layer from the 2-ply sheet, the layer of stainless steel is removed by fine controlled facing operation on a sub-sized clad specimen to a predetermined depth equal to the thickness of the SS430 layer.

The tensile tests are performed on a 50kN capacity universal testing machine (make: Tinius Olsen), integrated with environmental chamber as shown in Fig. 5.3. All tests are carried out at a constant crosshead speed of 2.5 mm/min, evaluating properties at different warm forming temperatures. The mechanical properties are evaluated at four different temperatures: room temperature (RT), 180°C, 220°C, and 300°C. Each tensile test is performed five times to capture the reproducibility of the experimental data points, as shown in Fig 5.4. The force and position data are logged using HORIZON software to compute the mechanical properties. From the force-elongation data, true stress-true strain curves as well as  $\ln(\text{true stress})$ -  $\ln(\text{true strain})$  curves have been plotted.

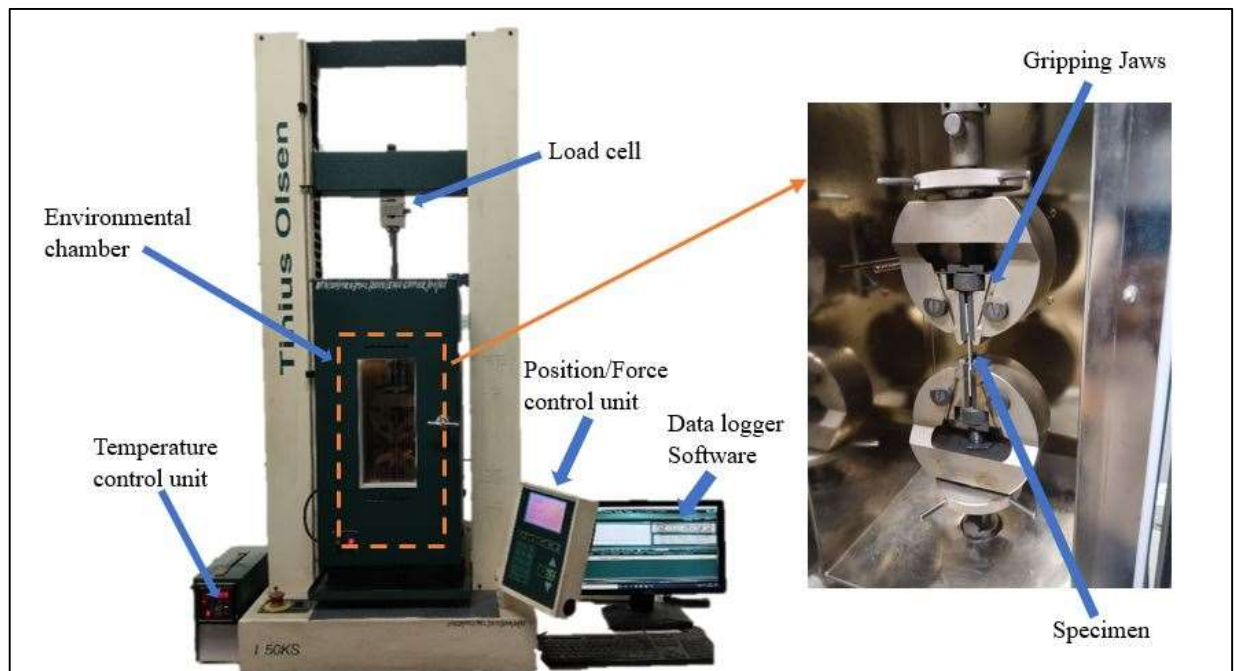


Fig. 5.3 UTM (50 kN capacity) integrated with environmental chamber

To convert engineering stress-strain data into true stress-strain data, the following equations have been employed:

$$\sigma = \sigma_e (1 + \epsilon_s) \quad (5.1)$$

$$\epsilon = \ln (1 + \epsilon_s) \quad (5.2)$$

where,  $\sigma$  is true stress,  $\epsilon$  is true strain,  $\sigma_e$  is engineering stress and  $\epsilon_s$  is engineering strain.

The log-log plots of true stress-true strain give the values of strain hardening exponent ( $n$ ) and strength coefficient ( $K$ ). From the power law of strain hardening ( $\sigma = K \epsilon^n$ ), where  $\sigma$  and  $\epsilon$  represents true stress and true strain, respectively, the values of the strength co-efficient and strain hardening exponent are calculated from true stress-true strain plots, taking into account the data from within the uniform plastic deformation range.

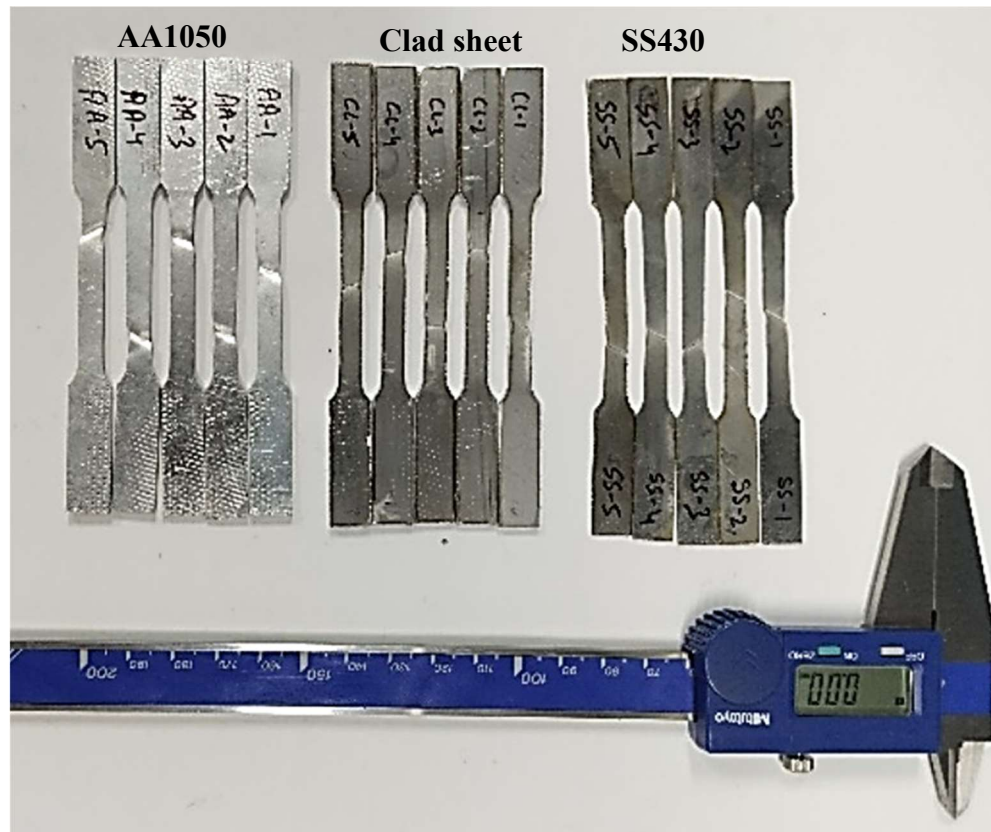


Fig. 5.4 Tensile tested specimens

### 5.2.2 Characterisation of Anisotropy

The anisotropy of the clad sheet and constituent layers is determined by evaluating the plastic strain ratio ( $R$ ) as per ASTM E517 standard, by deforming the specimens prepared with an orientation of  $0^\circ$ ,  $45^\circ$ , and  $90^\circ$  to the rolling direction to a predetermined strain, so that the ratios  $R_0$ ,  $R_{45}$ , and  $R_{90}$  can be determined, as shown in Fig. 5.5. The specimens are deformed to the point just before the occurring of ultimate tensile strength, which is generally 15 to 20 % of gauge length. Tensile specimens are plastically deformed to a specific value of plastic strain and cross heads are halted in automatic mode using the options available in the machine's specific software, Tinius Olsen Horizon. The width and gauge length were measured before and after the test with a digital vernier calliper, and the plastic strain ratio is computed

in all three directions with respect to the rolling direction (RD) using the following equation:  $w_f$

$$R = \frac{\epsilon_w}{\epsilon_t} = \frac{\epsilon_w}{-(\epsilon_w + \epsilon_l)} \quad (5.3)$$

where,  $\epsilon_w$  is true width strain,  $\epsilon_l$  is true longitudinal strain,  $\epsilon_t$  is true thickness strain.

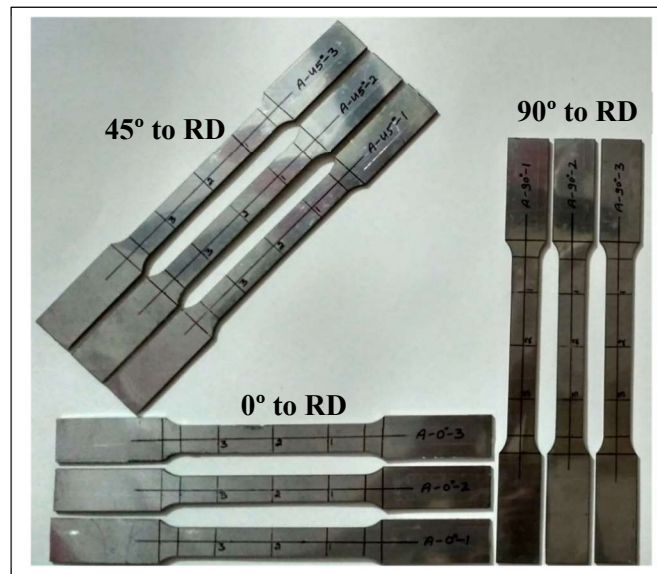


Fig. 5.5 Clad sheet anisotropy tested samples

The normal anisotropy ( $\bar{R}$ ) is calculated using the plastic strain ratio values obtained in three different orientations, using the standard formula as given below [102]:

$$\bar{R} = (R_0 + 2R_{45} + R_{90}) / 4 \quad (5.4)$$

where,  $R_0$ ,  $R_{45}$  and  $R_{90}$  indicate the plastic strain ratio of the tensile specimens oriented at  $0^\circ$ ,  $45^\circ$  and  $90^\circ$  with respect to RD. The  $\bar{R}$  value depends on the precision of the prepared edges' squareness and flatness and is highly susceptible to inaccuracy, particularly in width measurement. Therefore, in order to accurately determine the plastic strain ratio, all of the tensile specimens were prepared by laser cutting.

### 5.2.3 Determination of Residual stresses

The residual stresses are the internal, self-equilibrating stresses retained within a



material after external forces are removed, which can result in uneven material deformation. The residual stress measurement setup (PULSTEC  $\mu$ -X360n) is based on the  $\cos \alpha$  method of the X-ray diffraction technique to study the influence on the residual stresses in the SS and AA layers in the clad sheet after deformation at different temperatures, as shown in Fig. 5.6.

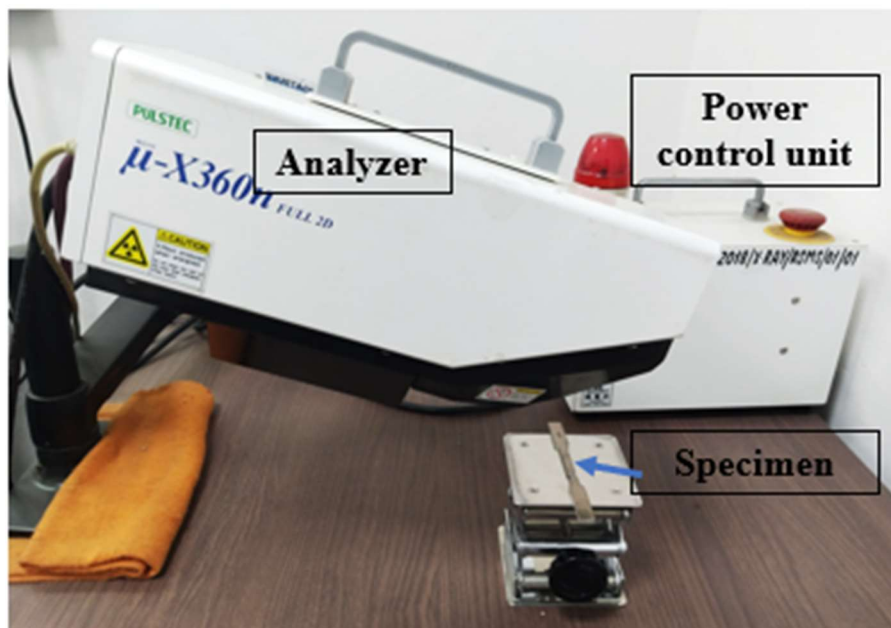


Fig. 5.6 Portable X-ray residual stress measurement setup

X-ray diffraction techniques are used for non-destructive testing of the residual stresses in the material. Taira et al. introduced the  $\cos \alpha$  method through X-ray diffraction, which could measure all plane stress components from one diffraction ring obtained by a single incident X-ray beam [103]. The  $\cos \alpha$  methodology leverages two-dimensional detectors to capture an entire Debye ring in one measurement, accelerating the assessment of residual stresses. Unlike traditional methods that require multiple sample tilts to gather similar data,  $\cos \alpha$  measurements are expedited and simplify the overall process. In the  $\cos \alpha$  technique utilizes the Debye-Scherrer (D-S) ring collected with a single measurement using a 2D detector. This method



incorporates Bragg's law to measure the variation in interplanar distance ( $d_{\psi\varphi}$ ) caused by the residual stress. The strain measurement uses the D-S ring, detected on the 2D detector with a tilt angle  $\psi_0$  from the Z axis, and rotation angle  $\varphi_0$  from the X axis as shown in Fig. 5.7.

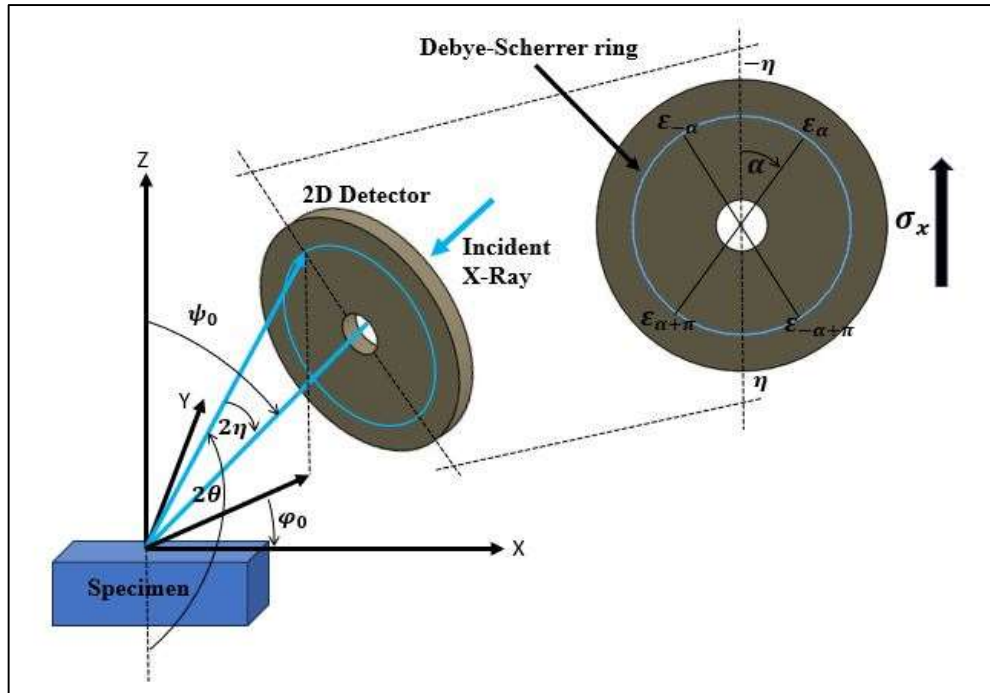


Fig. 5.7 Coordinate system of Cosα technique using a 2D detector

The strain  $\varepsilon_{\psi\varphi}$ , at azimuthal angle  $\alpha$  from  $-\eta$  as illustrated in Fig. 5.7, is expressed as follows:

$$\varepsilon_{\psi\varphi} = \varepsilon_{\alpha} = \frac{d_{\psi\varphi} - d_0}{d_0} = n_1^2 \varepsilon_x + n_2^2 \varepsilon_y + n_3^2 \varepsilon_z + n_1 n_2 \gamma_{xy} + n_2 n_3 \gamma_{yz} + n_1 n_3 \gamma_{xz} \quad (5.5)$$

where  $n_i (i = 1, 2, 3)$  is the direction component of the diffraction vector  $n$  with respect to the sample coordinate system. The diffraction vector  $n$  is expressed as [104]:

$$n = \begin{pmatrix} n_1 \\ n_2 \\ n_3 \end{pmatrix} = \begin{pmatrix} \cos\eta \sin\varphi_0 \cos\psi_0 - \sin\eta \cos\varphi_0 \cos\psi_0 \cos\alpha - \sin\eta \sin\varphi_0 \sin\alpha \\ \cos\eta \sin\varphi_0 \sin\psi_0 - \sin\eta \cos\varphi_0 \sin\psi_0 \cos\alpha + \sin\eta \cos\varphi_0 \sin\alpha \\ \cos\eta \cos\varphi_0 + \sin\eta \sin\varphi_0 \cos\alpha \end{pmatrix} \quad (5.6)$$

Now, the strain translation matrix represented by the equation,  $\varepsilon_{\alpha} = n_i n_j \varepsilon_{ij}$  ( $i, j = 1$  to 3). When combined with Hooke's law, the resulting expression is as follows:

$$\varepsilon_{\alpha} = \frac{1+\nu}{E} n_i n_j \varepsilon_{ij} - \frac{\nu}{E} \sigma_{kk} \quad (5.7)$$

where,  $\nu$  is poisson's ratio,  $E$  is Young's modulus,  $\sigma_{kk}$  ( $k=1-3$ ) is a stress component.

The mean value of the difference of strains at each azimuthal angle ( $\alpha$ ,  $-\alpha$ ,  $-\alpha + \pi$  and  $\alpha + \pi$ ) is used to determine the following two parameters ( $\varepsilon_{\alpha_1}$  and  $\varepsilon_{\alpha_2}$ ), which is expressed as follows:

$$\varepsilon_{\alpha_1} = \frac{1}{2} [(\varepsilon_{\alpha} - \varepsilon_{\alpha+\pi}) + (\varepsilon_{-\alpha} - \varepsilon_{-\alpha+\pi})] \quad (5.8)$$

$$\varepsilon_{\alpha_2} = \frac{1}{2} [(\varepsilon_{\alpha} - \varepsilon_{\alpha+\pi}) - (\varepsilon_{-\alpha} - \varepsilon_{-\alpha+\pi})] \quad (5.9)$$

The slope of the linear relationship between the above two equations and  $\cos \alpha$ , determines the residual stress  $\sigma_x$ , which can be expressed as [105]:

$$\sigma_x = - \left( \frac{E}{1+\nu} \right) \left( \frac{1}{\sin 2\eta \sin \psi_0} \right) \left( \frac{\partial \varepsilon_{\alpha_1}}{\partial \cos \alpha} \right) \quad (5.10)$$

where,  $\left( \frac{\partial \varepsilon_{\alpha_1}}{\partial \cos \alpha} \right)$  is the slope between the parameter  $\varepsilon_{\alpha_1}$  and  $\cos \alpha$ .

#### 5.2.4 Determination of coefficient of friction

The coefficient of friction values of both layers of clad sheet is determined at the above-mentioned temperatures as per the ASTM G133 standard. The test specimen is mounted in a reciprocating tribometer capable of producing smooth, controlled linear motion. A loading mechanism applies a constant uniform normal load to ensure consistent contact conditions throughout the test. A force sensor continuously measures the tangential (friction) force generated during sliding. A calibrated test setup measures for (a) the normal load, (b) stroke length and oscillation frequency, and (c) the friction force sensor in both forward and reverse directions. Appropriate test parameters are selected and documented. These include the normal load in newtons, stroke length ( $L$ ) in millimeters, and oscillation frequency ( $f$ ) in hertz. The test duration

(t) in seconds or the total number of cycles (N) is determined according to the experimental objective. The total sliding distance (X) is calculated using the relation  $X = 0.002 \times t \times f \times L$ , and the number of cycles  $N = t \times f$ . All additional factors like lubricant type, temperature, humidity, and contact geometry (ball diameter) are carefully recorded.

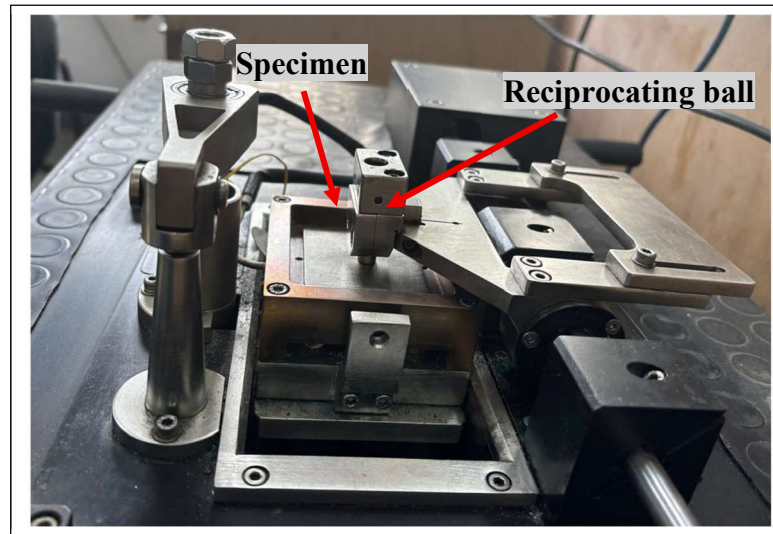


Fig. 5.8 Linear reciprocating tribometer

In the present investigation, the test is performed on the linear reciprocating tribometer (Fig. 5.8) using a steel ball of 6mm diameter to slide on the flat specimen with a stroke length of 10 mm at a frequency of 5 Hz, with a normal load of 10 N. The coefficient of friction (COF) is determined as the ratio of the sliding force to the normal applied force. An average value of the COF is taken from the sliding distance of 90 m. The COF is determined for both SS430 and AA1050 layers, in contact with steel ball, at room temperature, 180°C, 220°C and 300°C. The influence of MoS<sub>2</sub> lubrication on the COF is analysed and compared to the dry conditions at all temperatures for both materials.

### 5.2.5 Determination of Vickers micro-indentation hardness

Hardness tests have been found to be very useful for material characterisation, quality control of manufacturing processes, and in research and development efforts. Hardness, although empirical in nature, can be correlated to tensile strength for many metals, and is an indicator of wear resistance and ductility. Micro-indentation tests extend hardness testing to materials too thin or too small for macro-indentation tests. Micro-indentation tests allow specific phases or constituents and regions or gradients too small for macro-indentation testing to be evaluated.

This test method covers determination of the micro-indentation hardness of materials, made with Vickers indenters. The micro-indentation hardness test is performed using a calibrated machine to force a diamond indenter of specific geometry into the surface of the material being evaluated. The test forces range from 1 to 1000 gf, and the indentation diagonals are measured with an optical microscope after load removal. For any micro-indentation hardness test, it is assumed that the indentation does not undergo elastic recovery after force removal.

Vickers hardness number, HV, is an expression of hardness obtained by dividing the force applied to a Vickers indenter by the surface area of the permanent impression made by the indenter. The formulae presented as per ASTM standard for calculating micro-indentation hardness is presented here. For the Vickers hardness test, in practice, test loads are in grams-force and indentation diagonals are in micrometres. The Vickers hardness number is calculated as follows:

$$HV = 1854.4 (P/d^2) \quad (5.11)$$

where, P is the applied load (gf), and

d is the mean diagonal length of the indentation ( $\mu\text{m}$ ).

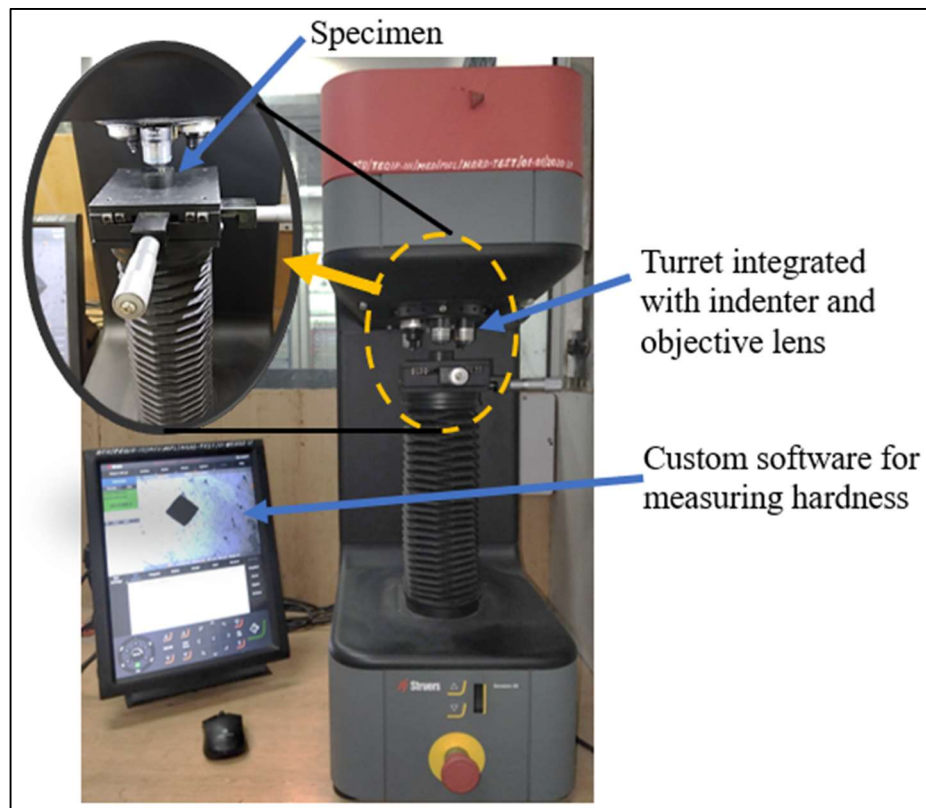


Fig. 5.9 Struers Micro-indentation Hardness tester

In the present investigation, Vickers micro-indentation hardness test setup (Struers Duramin-40) is used to perform the hardness test as per the ASTM E384 standard to analyse the influence of temperature on the hardness of the constituent layers SS430 and AA1050, as shown in Fig. 5.9. A square-base pyramidal-shaped diamond Vickers indenter with face angles of  $136^\circ$  creates an indent on a specimen with a predefined load of 0.5 Kg and dwell time of 10 sec. The dedicated software measures the average diagonal length of the indent, and the hardness is recorded on the scale of HV0.5.

### 5.3 Characterisation of the formability of the clad sheet

Formability of sheet metal is characterised by evaluating its ability to undergo plastic deformation without failure during forming operations. This is commonly assessed using two key parameters: the Forming Limit Diagram (FLD) and the Limiting Draw Ratio (LDR).

The forming limit diagram provides a graphical representation of the strain limits that the sheet can withstand before the onset of necking or fracture. It is obtained by subjecting sheet specimens to different combinations of stretching and drawing conditions to determine the maximum principal strain combinations that cause failure. The FLD helps in predicting safe and failure zones during complex sheet metal forming processes such as stamping or deep drawing.

The limiting draw ratio, on the other hand, is an important parameter specific to the deep drawing process. It is defined as the ratio of the maximum blank diameter that can be drawn into a cup without failure to the punch diameter. A higher LDR indicates better drawability of the sheet material. The LDR depends on material properties, such as yield strength, strain-hardening exponent, and anisotropy, as well as process parameters, including lubrication and die geometry.

Together, the forming limit diagram and limiting draw ratio provide a comprehensive understanding of a sheet material's formability. The FLD focuses on general forming operations, while the LDR specifically assesses deep drawing capability. To determine the FLD and LDR of the clad sheet Die, holder and punch setup is designed separately.

### **5.3.1 Design and development of experimental setup for forming at elevated temperature**

The basic steps involved in development of experimental setup, is first to design and fabrication of the tools, secondly to customize the heating and insulation of the tools. For the present investigation two separate tool setup is need to prepared, as FLD requires stretching operation through limit dome height test, wherein the material is firstly locked using a drawbead and then stretching is performed. Whereas, in the case

of deep drawing to determine the LDR, the material is allowed to flow into the die cavity to form a cup without any locking of the material in the flange region.

### 5.3.1.1 Design of tool setup to develop forming limit diagram

The tooling for conducting formability tests consists of a lower die, upper die and hemispherical bottom punch. Although a cylindrical punch of diameter 101.6 mm with hemispherical bottom is the standard punch size recommended by Hecker [33], a 50 mm diameter punch has been used in the present work due to the limited availability of 2-ply clad sheets of SS430/AA1050. Accordingly, the blank size has also been reduced. To accommodate the clad sheet of 2 mm thickness, the lower die was fabricated by providing an appropriate punch-die clearance of 2.6 mm. The recommended clearance between the die and punch is to be 20-40 % times the sheet thickness [106]. The die entry radius must be 5-10 times the sheet thickness, so a die entry radius or die corner radius of 10 mm was provided in the lower die to prevent tearing of the blank at the die entry [107]. The sheet metal will be locked on the die with the help of a draw bead of diameter 82 mm, with a profile radius of 4.5 mm. A 6 mm diameter hole is drilled at a distance of 12 mm from top surface to accommodate the thermocouple, for temperature measurement of die. The thermocouple will penetrate up to a depth of 40 mm radially into the die. The engineering drawings of the lower die with all the dimensions are shown in Fig. 5.10.

To guide the punch into the die, a clearance of 0.5 mm was provided between the punch and the blank holder (upper die). All the tools were fabricated using hot working tool steel of H13 grade, which is a chromium hot-work tool steel with a chemical composition that includes approximately 0.32-0.45% carbon, 4.75-5.5% chromium,



1.1-1.75% molybdenum, and 0.8-1.2% vanadium, as well as other elements like silicon, manganese, phosphorus, and sulphur in smaller amounts [108].

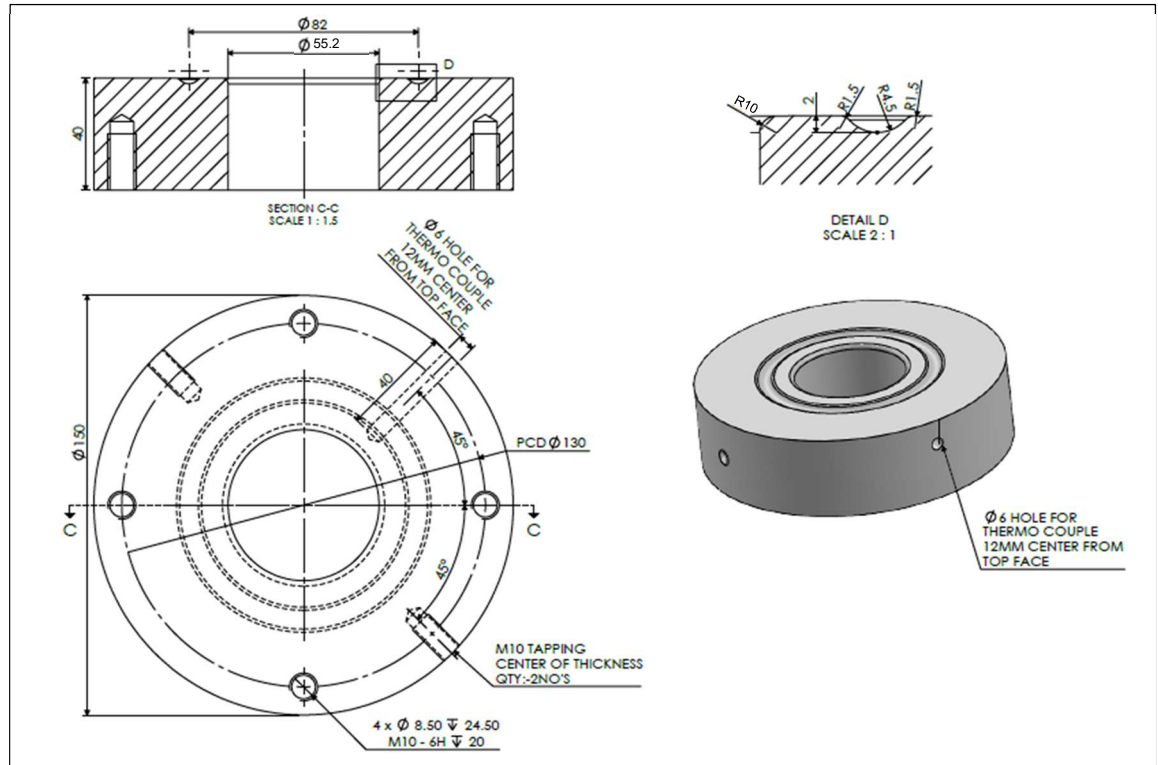


Fig. 5.10 Engineering drawing of lower die with dimensions and solid model

The H13 grade is high in strength, hardness, and resistance to heat and wear, making it suitable for hot-working applications. The punch is attached directly to the main ram of hydraulic press whereas the upper die was attached to the secondary ram by using a mild steel (MS) upper plate. For insulation 20 mm thick high-performance mica sheet is placed between the MS plate and the die. A mica sheet for insulation up to 1500°C is composed of mica flakes (a group of silicate minerals suitable for higher temperatures) with a binder, resulting in a material with approximately 30-35% alumina ( $\text{Al}_2\text{O}_3$ ), 40-55% silica ( $\text{SiO}_2$ ), 6-8% magnesia ( $\text{MgO}$ ), and trace amounts of other elements like calcium and iron. This composition gives it excellent heat resistance ability.



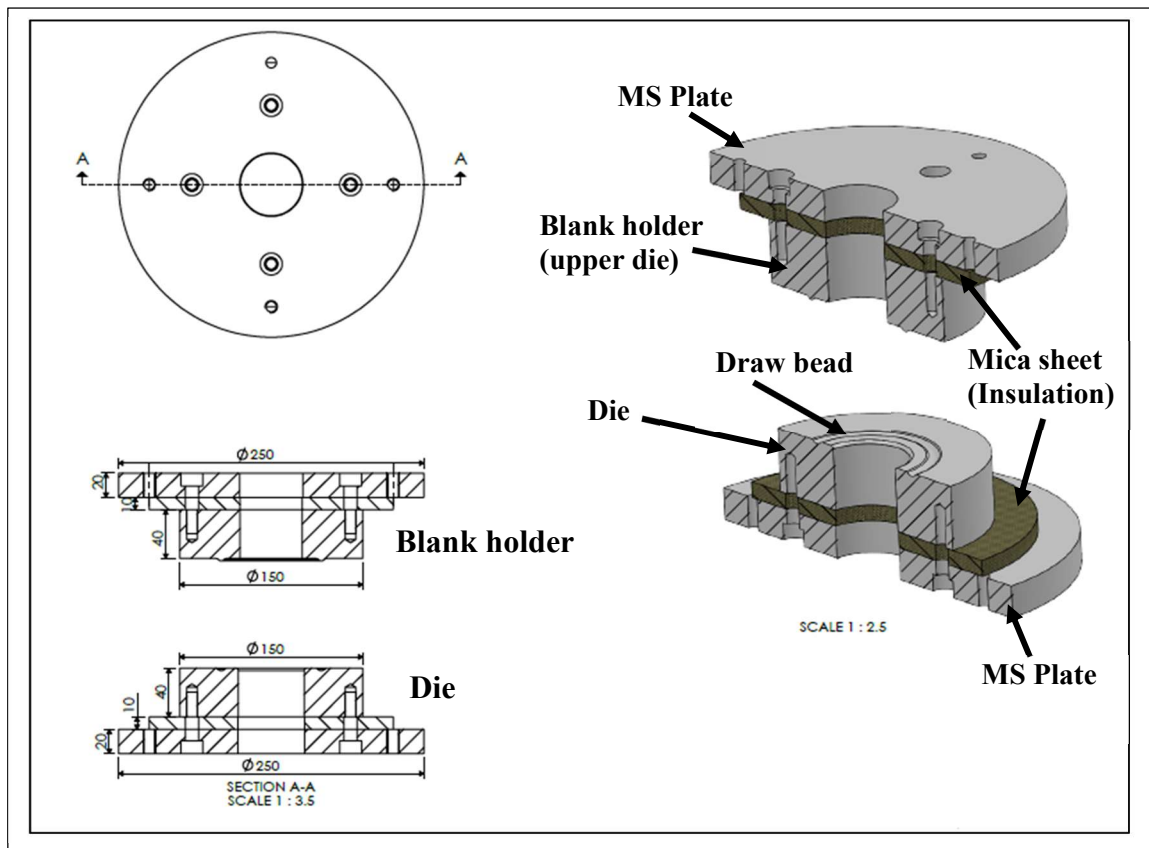


Fig. 5.11 Engineering drawing and solid model of the die and blank holder assembly

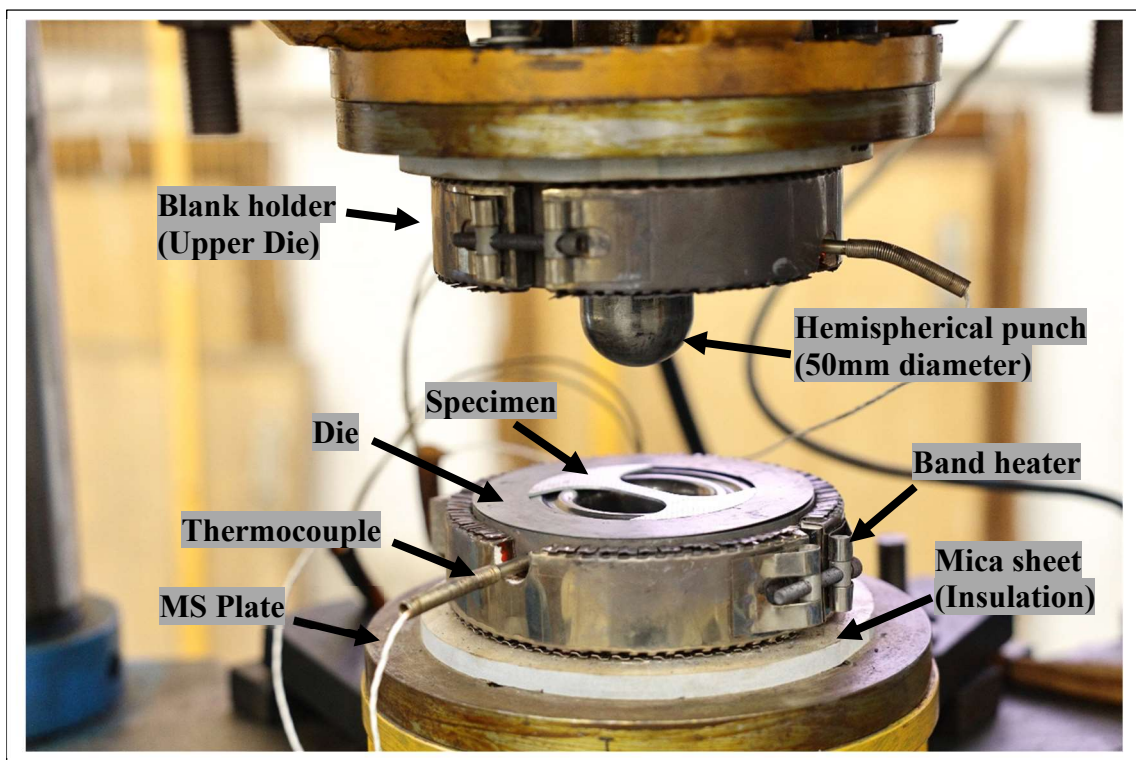


Fig. 5.12 Die, blank holder, punch with heater and thermocouple assembly

The lower die is placed on the MS plate, which is further clamped on a fixture, which is placed on the hydraulic press bed. The similar mica sheet of 20 mm thickness is used in between of the MS plate and the lower die as shown in Fig. 5.11. The mica sheet insulates the press bed from the heat flowing from the die through conduction. The fabricated tools using H13 grade tool steel and air hardened to a hardness value of 55 HRC, are assembled and shown in Fig. 5.12.

### 5.3.1.2 Design of tool setup for deep drawing analysis

The deep drawing analysis, also known as the swift cupping test, is a widely used experimental method for evaluating the deep drawing formability of sheet metals. It provides a quantitative measure of a material's ability to undergo plastic deformation to form a cup without failure during the drawing process. The most important parameter obtained from this test is the limiting draw ratio, which represents the maximum ratio of the blank diameter to the punch diameter that can be successfully drawn into a cup without rupture. In this analysis, a circular blank of the clad sheet is held between a blank holder and a die, with a significant amount of holding pressure applied to prevent wrinkling while allowing smooth material flow into the die. A punch then moves forward to draw the blank into the die cavity, forming a cup. The materials flow freely into the die cavity, without any locking by the draw bead, just as in the case of a stretching test, such as a limiting dome height test. There is no presence of a draw bead in the die setup for deep drawing. Die of inner radius 55.2 mm with die corner radius of 10 mm is designed for smooth flow over the die entry. A die-punch clearance of 2.6 mm is given, in order to accommodate the clad sheet of 2 mm thickness. Four holes in a circular arrangement of pitch circle diameter of 130 mm, is drilled to accommodate M10 threaded bolts of pitch 0.75 mm as shown in Fig. 5.13(a).

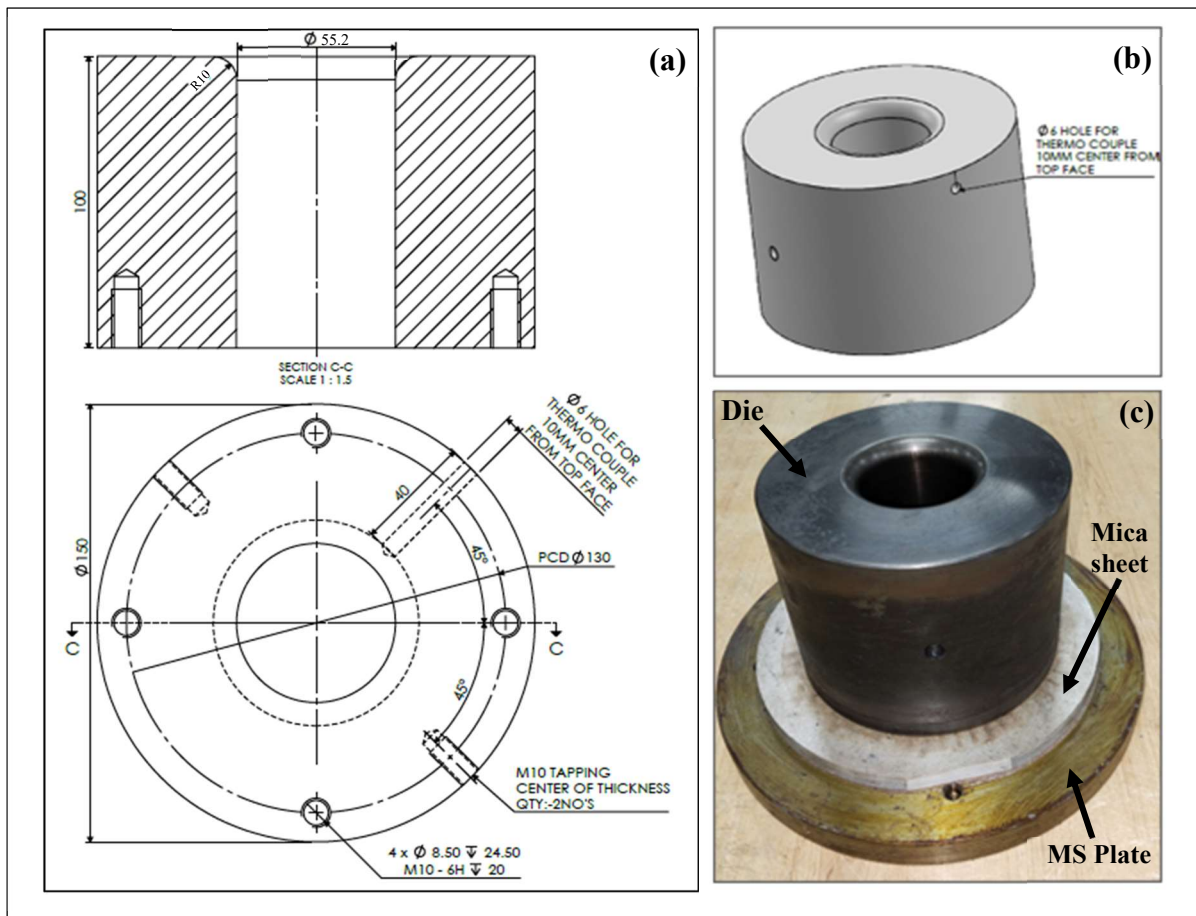


Fig. 5.13 (a) Engineering drawing, (b) solid model, and (c) fabricated die for deep drawing. The bolts are used to fix the die, mica sheet and MS plate together which will be placed on the hydraulic press bed as shown in Fig. 5.13 (c). A 6 mm diameter hole is drilled at a distance of 12 mm from top surface, as shown in Fig. 5.13 (b), to accommodate the thermocouple, for temperature measurement of die, which will penetrate up to a radial depth of 40 mm. A 50 mm diameter cylindrical flat nose punch is used to perform the deep drawing operation. Fig. 5.14 illustrates the assembly of the die, blank holder and punch with heating arrangement on the hydraulic press.

### 5.3.2 Heating system and temperature control

Heating of the blanks to the required temperatures can be achieved by different heating methods i.e external heating, internal heating or combined heating. In external heating, the blanks are heated separately in a furnace and then transferred to the cold tools. In

the internal heating method, the blank is placed between the heated dies and closed for some time to achieve the test temperature through heat conduction from the tools.

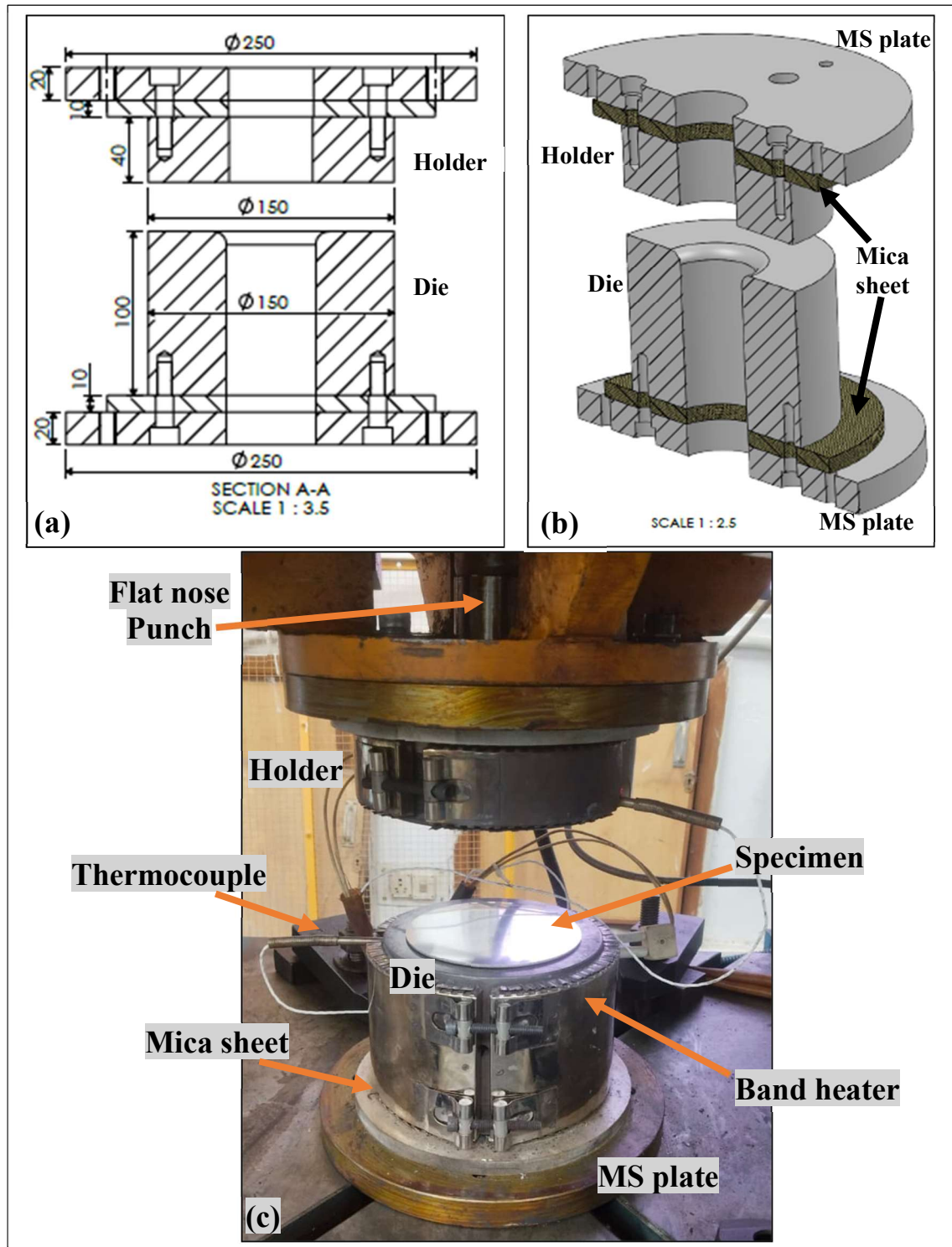


Fig. 5.14 (a) Engineering drawing, (b) solid model, and (c) fabricated assembly setup for deep drawing

In the present study, the internal heating method has been adopted to avoid any microstructural changes in the material due to rapid cooling while shifting the material from furnace to press. Punch is heated using cartridge heaters. Die and blank holder are heated using the band heaters to achieve temperatures up to 300°C. Nichrome (80% nickel and 20% chromium) is used to fabricate heating wire in the cartridge and magnesium oxide core is provided between the heating element and the casing to absorb moisture between the heating wire and the surroundings. The temperature in the tools is measured using a K type thermocouple which is controlled and monitored by a proportional-integral-derivative (PID) temperature controller. The band heaters with a rating of 750 watts for the stretching die and 1500 watts for the deep drawing die is used in this study. The wattage of heating elements is estimated as shown below:

#### Wattage calculation for band heater for the stretching die

Volume of the hollow cylinder

$$\begin{aligned} V &= \pi (R^2 - r^2) h \\ &= \pi (7.5^2 - 2.76^2) \times 4 \\ &= 610.82 \text{ cm}^3 \end{aligned}$$

where,  $h$  is height,  $R$  is outer radius and  $r$  is inner radius of die.

Density of H13 tool steel = 7.80 g/cm<sup>3</sup>

Mass of the die to be heated = 7.80 x 610.82 = 4764.42 g = 4.764 kg

Heat required,  $q = m c_p \Delta T$

Specific heat of tool steel is  $c_p = 0.46 \text{ J/g K}$

$\Delta T = 300^\circ\text{C} - 25^\circ\text{C} = 275^\circ\text{C} = 548 \text{ K}$

Therefore  $q = 4764.42 \times 0.46 \times 548 = 1201014.73 \text{ J}$

Time requirement for initial heating is 30min (1800s)

Power consumption or rate of heating is  $q / t = 1201014.73 \text{ J} / 1800\text{s} = 667.23 \text{ Watt}$



So, casing heaters of **750 watts** have been used to heat the dies, considering the heat loss to the surroundings from the tools during heating, which was neglected in the above calculations.

### **Wattage calculation for band heater for the deep drawing die**

Volume of the hollow cylinder

$$\begin{aligned} V &= \pi (R^2 - r^2) h \\ &= \pi (7.5^2 - 2.76^2) \times 8 \\ &= 1527.06 \text{ cm}^3 \end{aligned}$$

where,  $h$  is height,  $R$  is outer radius and  $r$  is inner radius of die.

Density of H13 tool steel =  $7.80 \text{ g/cm}^3$

Mass of the die to be heated =  $7.80 \times 1527.06 = 11911.04 \text{ g} = 11.911 \text{ kg}$

Heat required,  $q = m c_p \Delta T$

Specific heat of H13 tool steel is  $c_p = 0.46 \text{ J/g K}$

$\Delta T = 300^\circ\text{C} - 25^\circ\text{C} = 275^\circ\text{C} = 548 \text{ K}$

Therefore  $q = 11911.04 \times 0.46 \times 548 = 3002536.83 \text{ J}$

Time requirement for initial heating is 40min (2400s)

Power consumption or rate of heating is  $q / t = 3002536.83 \text{ J} / 2400\text{s} = 1251.06 \text{ Watt}$

So, casing heaters of **1500 watts** have been used to heat the dies, considering the heat loss to the surroundings from the tools during heating, which was neglected in the above calculations.

### **5.3.3 Hydraulic press assembly with the designed tools**

In the present study 100 tonne capacity double acting hydraulic press is used to perform the stretching and the deep drawing operation. The CAD assembly of the hydraulic press is shown in Fig. 5.15, integrated with the designed tools, showcasing the available working punch displacement for the forming operations.

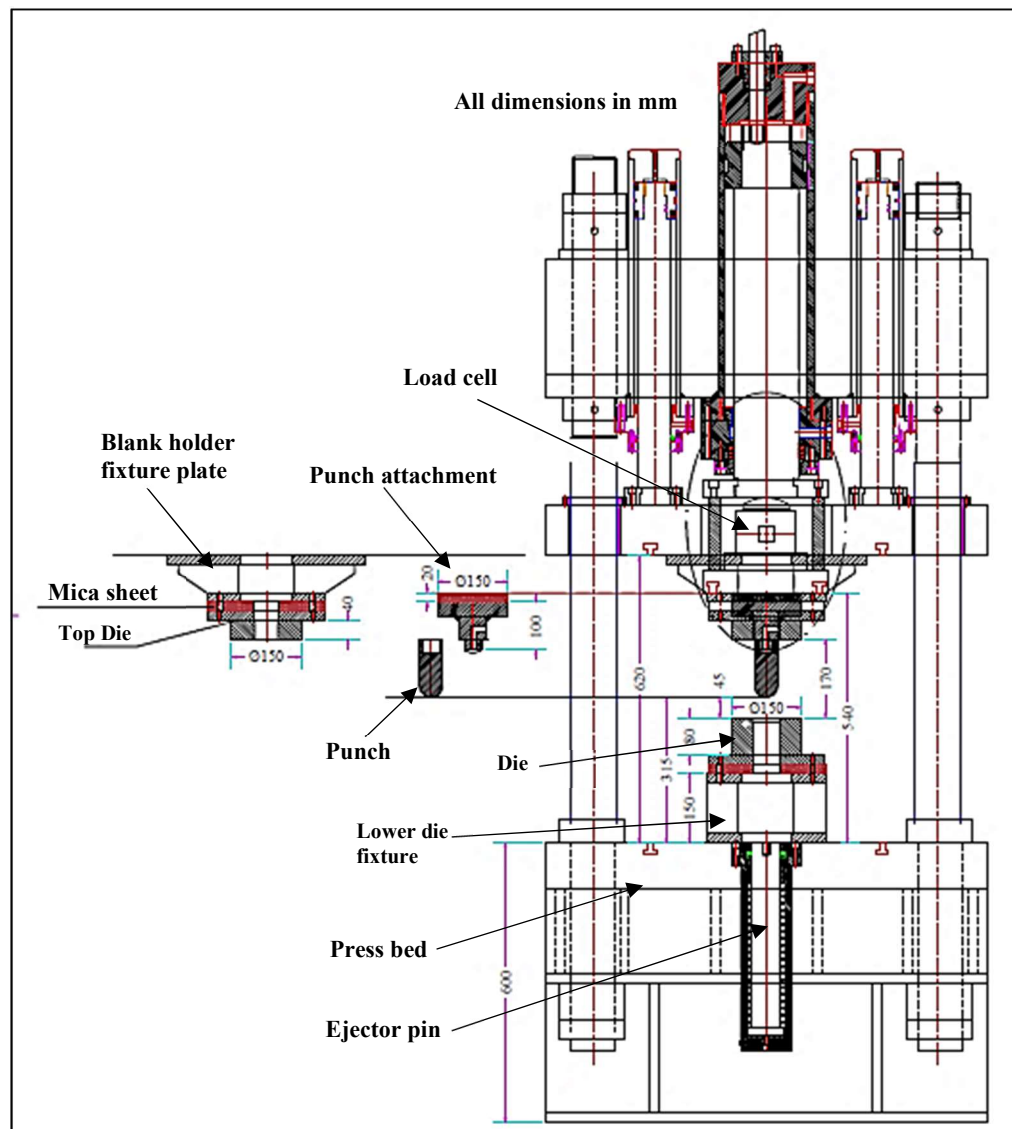


Fig. 5.15 CAD assembly of hydraulic press with the designed tools (all dimensions in mm)

The designed deep drawing die is fixed with the mica sheet (in red) and MS plate to the lower die fixture, which is further placed on the hydraulic press bed. Similarly, the blank holder is clamped to the holder bed (ram), through the mica sheet and the fixture. The mica sheet on the holder side shields the load cell from the elevated temperature, which could hamper its functioning. The maximum daylight gap (distance between the lower die bed to upper die bed) of the hydraulic press is 620 mm. The available working distance of the punch for the assembled tool setup was seen to be 110 mm.

which is sufficient for the present investigation operations. The final fabricated tools assembled with the hydraulic press are shown in Fig. 5.16. The programmable logic controller (PLC) converts the analog signals hydraulic valve and rotary encoder into digital signal, which helps to ensure proper flow of the hydraulic oil and hence the ram speed could be controlled during the operation.

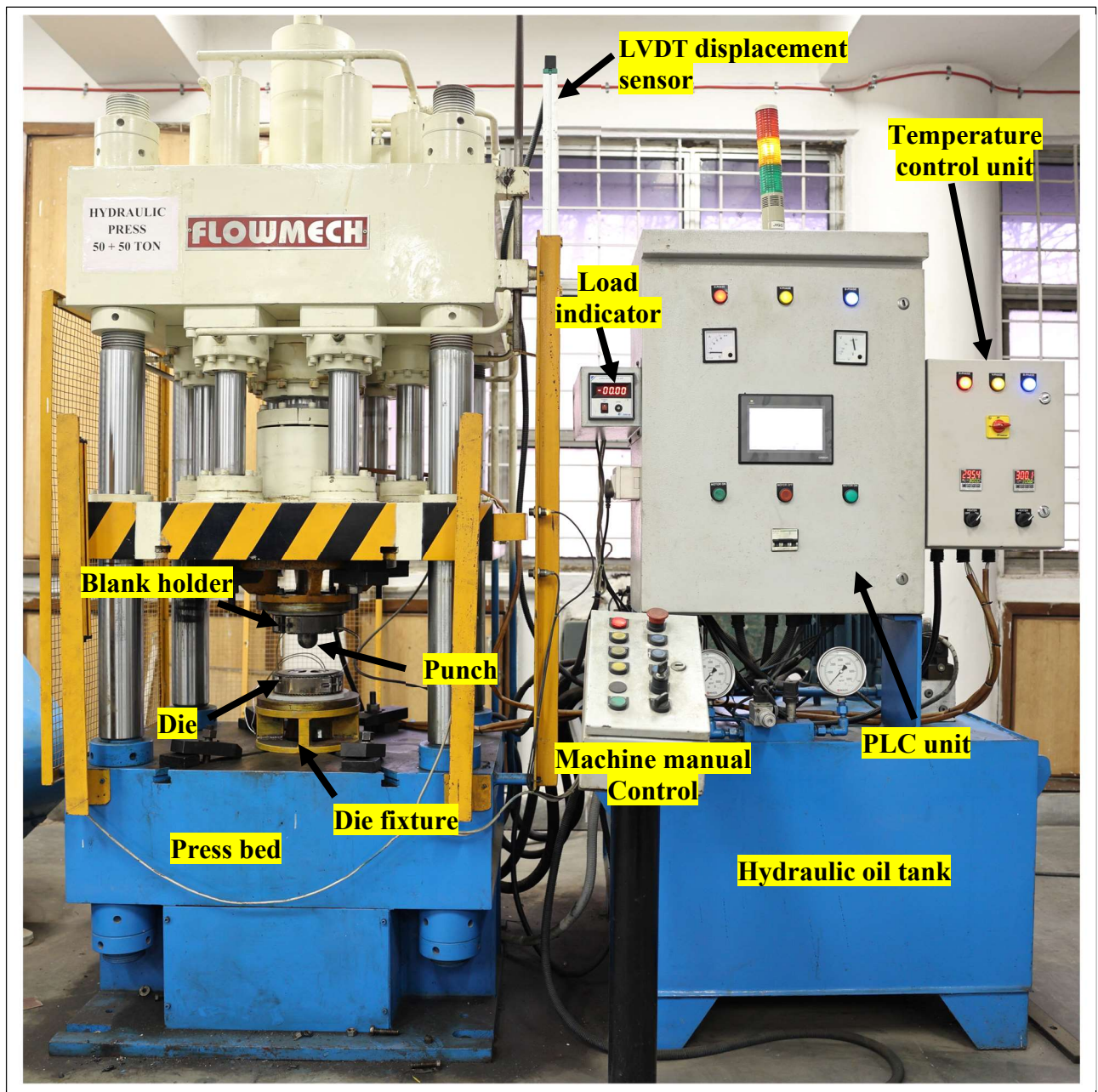


Fig. 5.16 Experimental setup showing assembly of fabricated tools integrated with 100 tonne capacity hydraulic press



### 5.3.4 Determination of forming limit diagram

Forming limit diagrams (FLDs) of the SS430/AA1050 2-ply clad sheet of 2 mm thickness are determined through Hecker's testing method by using a 50mm diameter hemispherical punch. Formability is determined at four different temperatures, i.e. room temperature, 180°C, 220°C, and 300°C, in order to determine the effect of temperature on limit strains in the warm working temperature range. The temperature range is selected based on the warm forming temperature of AA1050. Furthermore, when the temperature is increased beyond 300°C, the AA1050 layer becomes stuck to the upper die and punch after the removal of the blank holder. This is attributed to the sticking friction on the aluminium layer. Additionally, it was observed that the SS430 surface became discoloured at approximately 400°C.

Furthermore, the formability of the clad sheet is determined with the clad layup having AA1050 in contact with the punch, and SS430 layer to be in contact with the lower die. Pazand et al. outlined that the higher FLD is achieved when the layer in contact with the punch is a material with the lowest strength in the clad sheet [68]. All tests are performed on a 100-tonne capacity hydraulic press at a punch speed of 0.5 mm/sec. The least count of the load cell is 0.01 tonne. Blanks of ten different widths (10mm, 20mm, 30mm, 40mm, 50mm, 60mm, 70mm, 80mm, 90mm and 100mm.) are used to obtain limit strains in three different modes of deformation i.e., tension-compression, plane strain and biaxial tension as shown in Fig. 5.17. The specimens up to 40mm width result in tension-compression deformation mode, the 50mm specimen results in plane strain and specimens from 60mm to 100mm result in biaxial deformation modes. Blanks were initially marked with a 2.5 mm diameter circular grid, with a 0.5 mm gap between the circles, using a 20W CO<sub>2</sub> laser marking machine, as shown in Fig. 5.18.

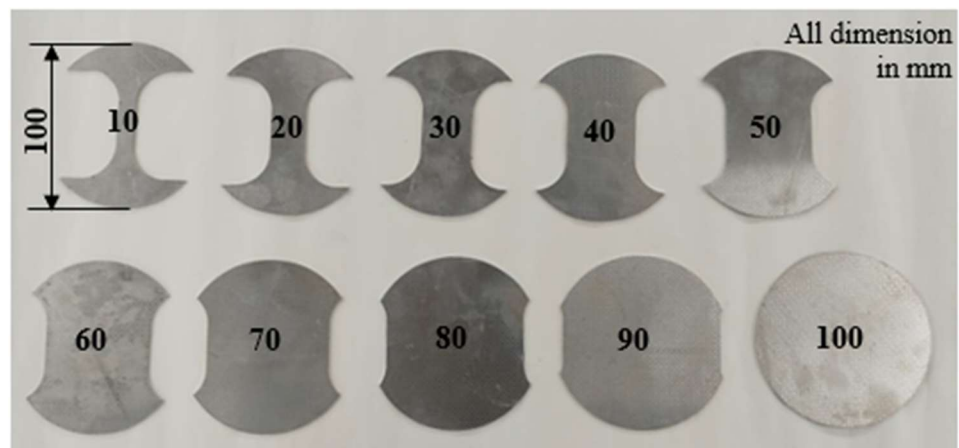


Fig. 5.17 Clad sheet specimens used for the determination of FLD

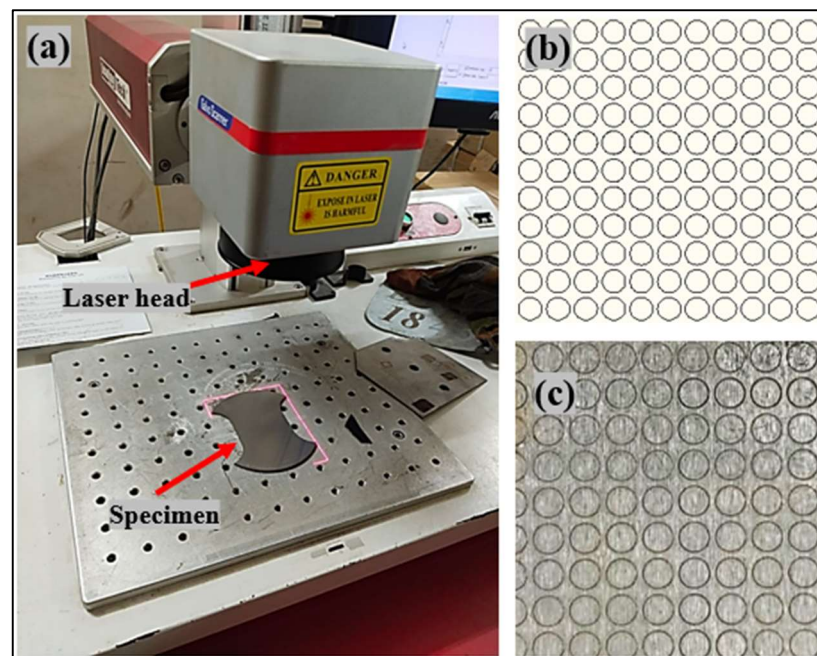


Fig. 5.18 (a) Laser marking in progress with 20W laser head, (b) CAD grid pattern of 2.5mm diameter circles, and (c) laser-marked pattern on clad specimen

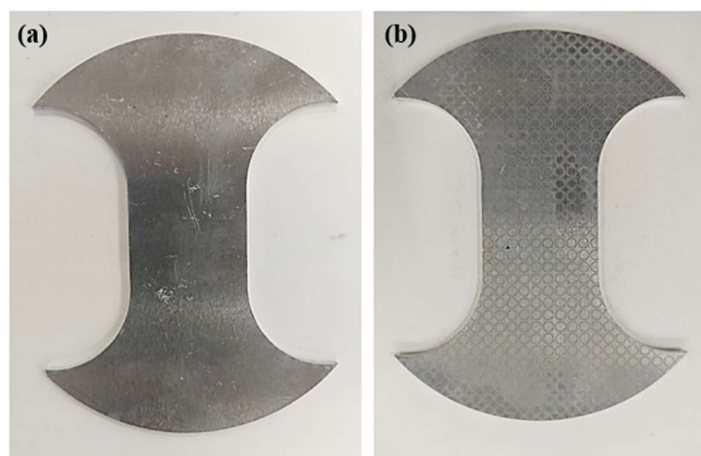


Fig. 5.19 Clad specimen (a) before, and (b) after laser marking

Fig. 5.19 shows a 30mm width FLD specimen before and after laser marking of 2.5mm diameter circles with 3mm centre distance with adjacent circles. The grid pattern is marked only on the SS430 layer, as the steel layer will be the outer layer of the formed dome, where necking is observed during the stretching process.

1 The specimen is placed between the upper and the lower dies. An optimum blank holding force in the range of 2-3 tonnes is applied manually on the upper die to clamp the blank at the draw bead. The experiment is stopped when a visible neck or initiation of fracture is obtained on the specimen as shown in Fig. 5.20. In all the above stretch forming experiments a data acquisition system consisting of a load cell and a rotary encoder is used to obtain the load - displacement data from the experiments. Amplifier is used to amplify the signals from the load cell and the rotary encoder. These amplified signals are converted to digital signals by analog to digital converter and fed to the computer. From these digital data, a load - displacement curves are plotted.

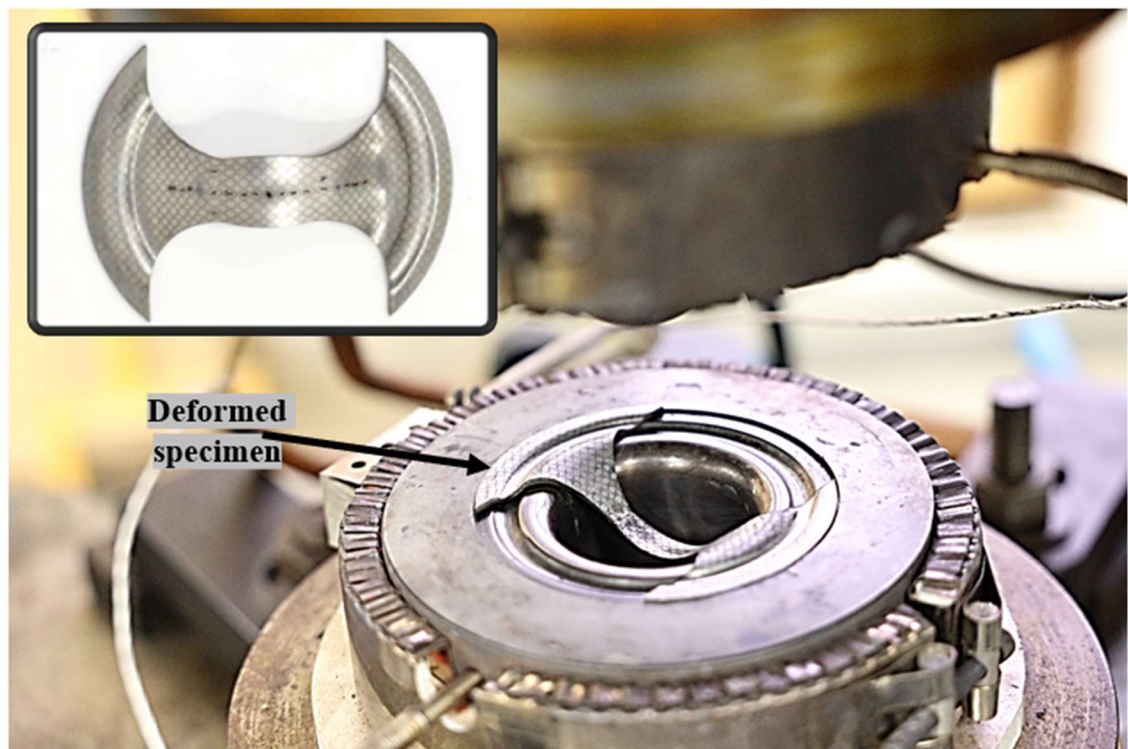


Fig. 5.20 Deformed FLD clad sample at fracture

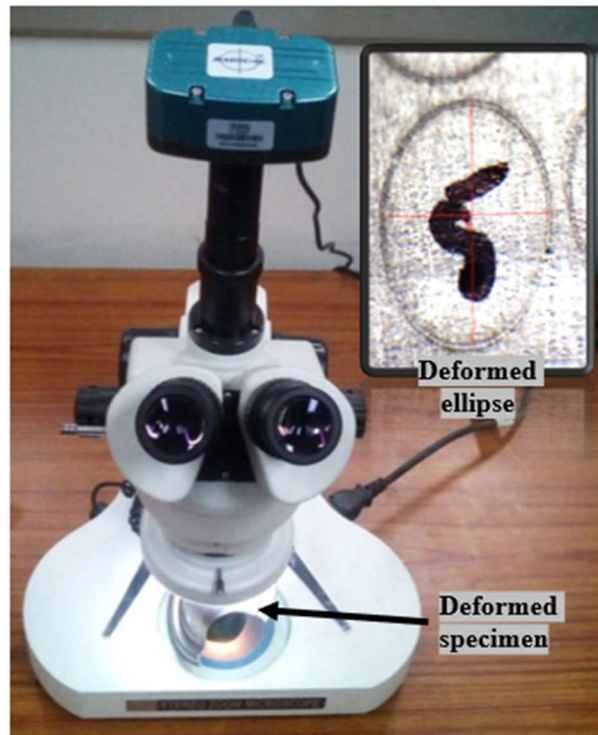


Fig. 5.21 Measurement of strains using stereo zoom microscope on a deformed specimen



Fig. 5.22 Dome height measurement of FLD specimen using vernier height gauge

Major and minor principal strains are calculated by measuring major and minor diameters of ellipses on the deformed samples. A stereo zoom travelling microscope



1 having a least count of 0.001mm is used to measure major and minor diameters of ellipses for strain calculations, as shown in Fig. 5.21. The dedicated software takes 1 photographs and measurement of the images taken by the microscope. The dome height of all the FLD specimens at the point of necking/fracture was measured using a vernier height gauge with a least count of 0.02 mm, as shown in Fig. 5.22.

At elevated temperatures, friction plays a crucial role in the forming of sheet metal components, significantly influencing material flow, surface quality, and overall formability. During warm forming operations, the contact conditions between the tool and the workpiece change due to thermal softening of the material and variations in surface oxidation. High frictional resistance can restrict material flow, resulting in non-uniform thinning, wrinkling, or tearing. Therefore, maintaining an optimal level of friction is essential to ensure a smooth material flow and adequate forming control.

Molybdenum disulfide ( $\text{MoS}_2$ ) is a solid lubricant widely recognised for its excellent high-temperature performance [59]. It possesses a layered crystal structure, where weak forces between layers allow easy shear under load, thereby providing low friction even under extreme pressure and temperature conditions.  $\text{MoS}_2$  can maintain its lubricating properties up to approximately 400°C-450°C in air, inert, or vacuum environments, making it highly suitable for warm forming operations. In the present investigation, the effect of  $\text{MoS}_2$  lubrication on the forming limit diagram is studied, all four temperatures.

### 5.3.5 Deep drawing analysis

The deep drawing experiment is a widely used method for evaluating the formability and drawability of a sheet metal undergoing different modes of deformation in the flange and wall region, respectively. In this test, a circular blank of initial diameter

‘ $D_{\text{blank}}$ ’ is drawn into a cup shape using a flat bottom punch of diameter ‘ $d_{\text{punch}}$ ’. The Limiting Drawing Ratio (LDR), defined as the maximum drawing ratio ‘ $D_{\text{blank}}/d_{\text{punch}}$ ’ that allows successful cup formation without defects, serves as a key index for assessing material’s deep drawability. A higher LDR indicates better formability. During a drawing process, plastic deformation primarily occurs in the flange undergoing compressive hoop stress and the cup wall under the tensile stress. The blank-holder force (BHF) plays a critical role in controlling material flow and ensuring the quality of the drawn component. Excessive BHF can lead to an increase in tensile stresses within the cup wall, potentially surpassing the material’s tensile strength and resulting in a premature fracture. Conversely, insufficient BHF may lead to wrinkling. The deep drawing experiments are performed on a 100 tonne capacity double acting hydraulic press, to determine the LDR of the clad sheet at RT, 180°C, 220°C and 300°C. At all temperatures, the effect of MoS<sub>2</sub> lubrication on the LDR of the clad is observed. The experiment is performed by drawing a circular blank using the flat bottom cylindrical punch of 50 mm diameter and a punch corner radius of 5 mm, through a die of 55.2 mm diameter with a die corner radius of 10 mm. The punch speed is maintained at 0.5 mm/sec for all experiments. The tools are heated using band heater and controlled through an integrated programmable logic controller. The displacement, force, and temperature are measured through the LVDT sensor, load cell, and K-type thermocouple.

## 5.4 Microstructural characterisation

To evaluate the interfacial integrity of the clad interface, a comparative analysis of the clad interfaces of the as-received sheet and the clad sheet samples with 20% plastic

deformation at room temperature and 300°C is done using the EBSD technique.

#### **5.4.1 Sample preparation**

Conventional shearing and sawing operations often induce plastic deformation, resulting in severe damage to the specimen's cross-section and the formation of a burr that hinders accurate microstructural analysis. To avoid these issues, specimens from both the as-received clad sheet and those subjected to 20% plastic strain during tensile testing were carefully sectioned using a diamond abrasive wheel with coolant. This method ensured a smooth, flat cross-sectional surface and minimum unwanted surface irregularities. After shearing, the specimen is polished, using silicon carbide-based emery paper with varying grit sizes ranging between 220 and 2000. Increasing order of grit size is carried, which is in progressive order of fineness. The specimens underwent a final process of fine polishing through electropolishing, resulting in a scratch-free surface for electron backscatter diffraction.

The SS430/AA1050 2-ply clad sheet specimens are dipped in an electrolyte solution of 80% methanol and 20% perchloric acid. The electropolishing is conducted at 14 V DC and 253K for 16 seconds. In EBSD based metallographic investigations, this kind of surface is required.

#### **5.4.2 Electron backscatter diffraction (EBSD)**

EBSD measurements are conducted to analyse the microstructural evolution of the clad sheet interface tested to 20% strain at room temperature and 300°C compared to that of the as received clad sheet. As shown in Fig. 5.23, the three orthogonal axes of the tensile specimen, as rolling direction (RD), normal direction (ND), and transverse direction (TD), are considered during the measurement. For EBSD analysis, the cross section of the clad interface is examined at the specimen mid length, with the TD as

the viewing direction. For EBSD studies, a TSL-EDAX OIM system mounted on an FEI Quanta-3D field emission gun (FEG) scanning electron microscope (SEM) is used as shown in Fig. 5.24.

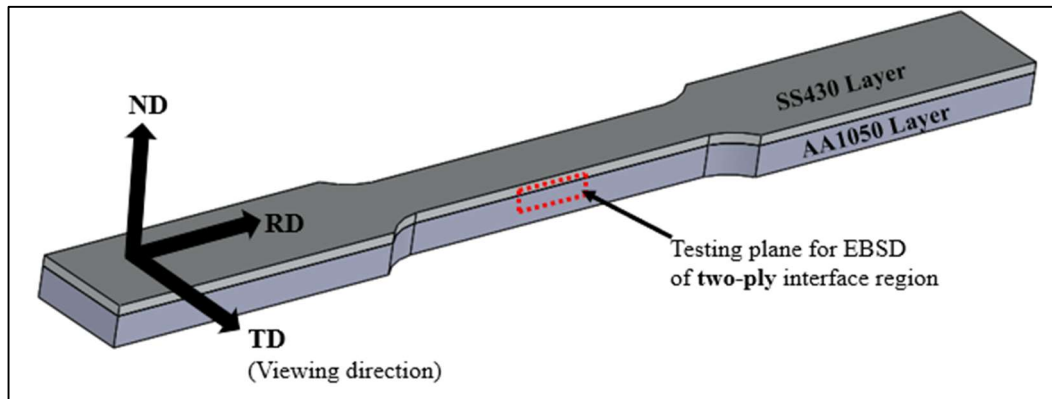


Fig. 5.23 Specimen orientation for EBSD measurement



Fig. 5.24 Field emission gun (FEG) scanning electron microscope (SEM) for electron backscattered diffraction (EBSD) analysis

The results of EBSD are described in the terms of inverse pole figure, grain boundary map, misorientation angle distribution, pole figures, kernel average misorientation, geometrically necessary dislocations, and twin boundary map. Additionally, scanning



electron microscopy with energy-dispersive X-ray spectroscopy (SEM–EDS) is performed on fractured samples to investigate fracture characteristics and elemental composition.

## **CHAPTER 6**

### **RESULTS AND DISCUSSION**

The results of various experiments conducted to characterise the mechanical properties of the SS430/AA1050 2-ply clad are presented and discussed in this chapter. The characterisation of the mechanical properties of constituent layers are also discussed. The forming limit diagrams and the limiting draw ratio of the clad sheet at different temperatures and different lubrication conditions are analysed.

#### **6.1 Mechanical properties**

##### **6.1.1 Tensile properties of 2-ply sheet**

The average mechanical properties from the uniaxial tension test of the SS430/AA1050 clad sheet and the individual parent layers at four temperatures are shown from Table 6.1 to Table 6.3. The true stress vs. true strain plots of the clad sheet and the individual layers separately are shown in Fig. 6.1. The flow stresses of the clad sheet are observed to decrease as the temperature increases. The yield strength (YS) and ultimate tensile strength (UTS) values decrease by 17% and 24%, respectively, whereas the ductility of the clad sheet exhibits an 8% reduction as the temperature increases from RT to 300°C.

The flow stresses of the clad sheet exhibit an average value derived from the flow stresses of the individual SS430 and AA1050 components as illustrated in Fig. 6.2. The strain hardening exponent, which indicates the ability of the material to strengthen itself under plastic deformation, increases from 0.20 to 0.23 as the temperature increases from RT to 300°C. The mechanical properties of the extracted SS430 layer reflect a trend similar to that of the clad sheet. The YS and UTS values exhibit a

decrease of 33% and 22%, respectively, as shown in Fig. 6.3.

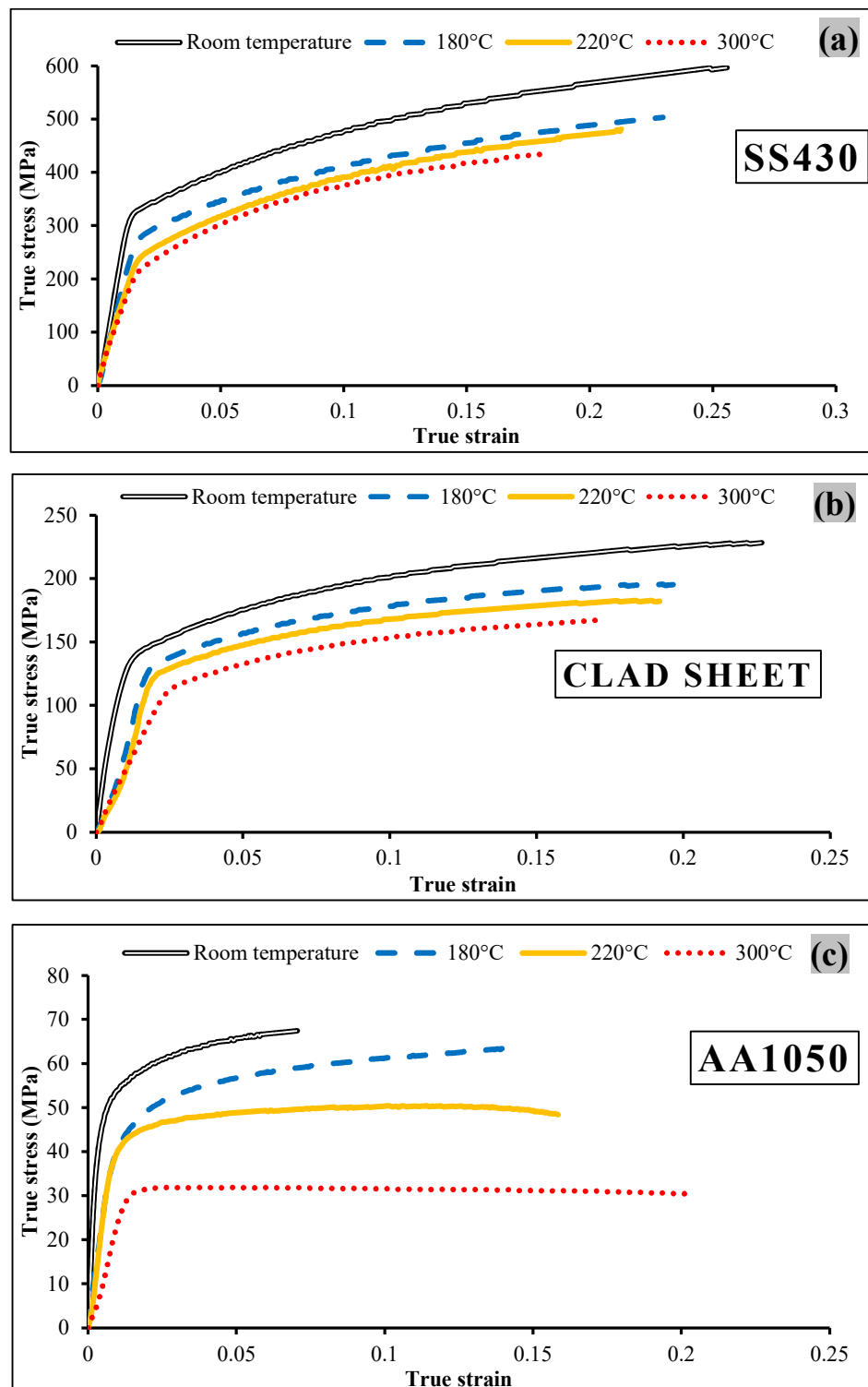


Fig. 6.1 True stress vs. true strain plots at different temperatures of (a) SS430 layer, (b) two-ply clad sheet and (c) AA1050 layer

Also, a 10% drop in ductility for the SS430 layer, when the temperature rises from room temperature to 300°C. The ductility of ferritic steel and both ferritic (SS430) and austenitic (SS304) stainless steels reduces along with the reduction in strength values as the temperature increases [109,110]. The influence of temperature on ductility is associated with several factors in microstructure, like grain boundary map (misorientation), dislocation density, and grain boundary segregation of impurities. The flow stress of the SS430 layer is, on average, 2.3 times greater than that of the clad sheet at any given temperature.

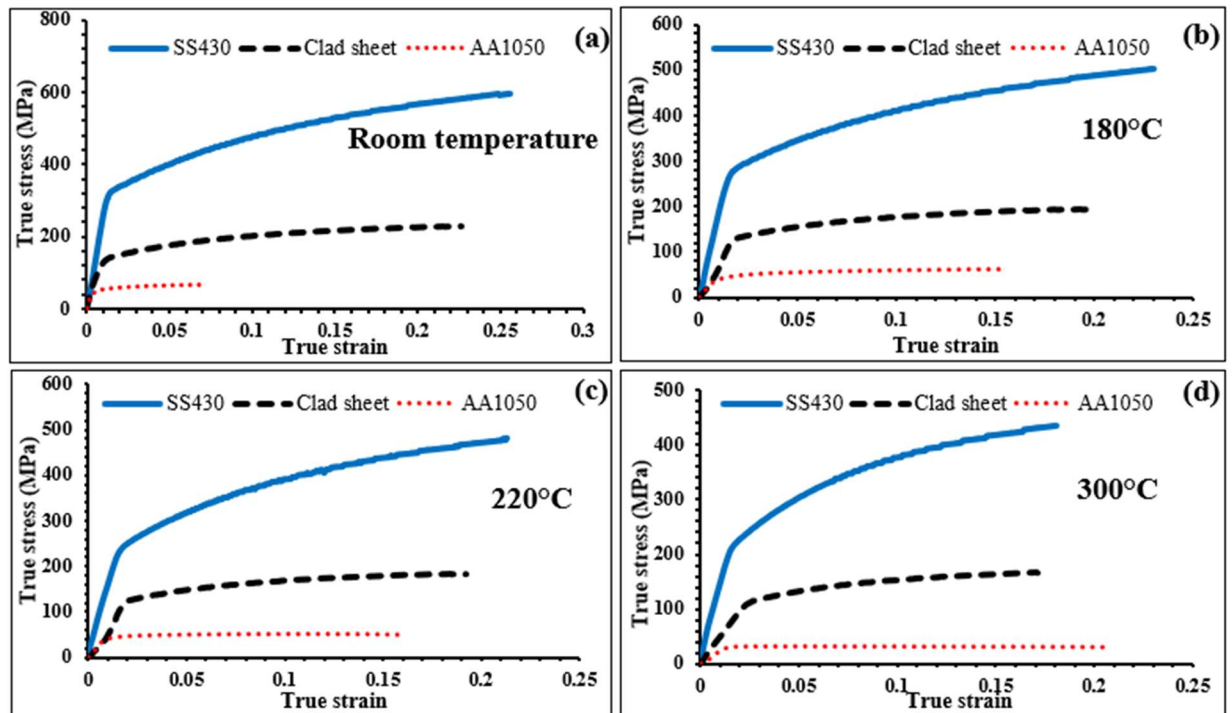


Fig. 6.2 True stress vs. true strain plots of clad sheet, SS430 and AA1050 layers at (a) room temperature, (b) 180°C, (c) 220°C, and (d) 300°C.

The strain hardening exponent values increase considerably from 0.24 to 0.29 as the temperature increases from RT to 300°C, respectively. The YS and UTS values of the extracted AA1050 layer exhibit a 38% and 48% decrease, respectively, accompanied by a 12.5% increase in ductility when the temperature rises from RT to 300°C. The strain hardening exponent values significantly reduce from 0.13 to 0.04 as the

temperature rises from room temperature to 300°C, respectively.

Table 6.1. Tensile properties of SS430 layer

Temperature	Yield strength (MPa)	Tensile strength (MPa)	% elongation	Strain hardening exponent, n	Strength coefficient, K (MPa)	Normal anisotropy, $\bar{R}$
RT	327 ± 4.54	464 ± 5.44	32.62 ± 1.18	0.24	830 ± 6.12	1.13
180°C	273 ± 4.11	402 ± 4.64	29.14 ± 1.31	0.24	785 ± 5.31	1.52
220°C	239 ± 3.68	387 ± 4.08	26.25 ± 1.02	0.25	748 ± 4.92	1.83
300°C	218 ± 4.08	363 ± 2.44	22.15 ± 1.14	0.29	716 ± 4.89	1.95

Table 6.2. Tensile properties of a clad sheet.

Temperature	Yield strength (MPa)	Tensile strength (MPa)	% elongation	Strain hardening exponent, n	Strength coefficient, K (MPa)	Normal anisotropy, $\bar{R}$
RT	133 ± 3.26	186 ± 3.26	30.22 ± 1.28	0.20	316 ± 4.50	0.71
180°C	127 ± 3.09	164 ± 3.74	27.65 ± 1.38	0.22	273 ± 4.02	0.86
220°C	122 ± 2.86	154 ± 2.86	25.82 ± 0.96	0.22	259 ± 3.40	0.95
300°C	110 ± 2.16	141 ± 3.09	22.28 ± 0.67	0.23	214 ± 2.86	1.10

Table 6.3. Tensile properties of AA1050 layer.

Temperature	Yield strength (MPa)	Tensile strength (MPa)	% elongation	Strain hardening exponent, n	Strength coefficient, K (MPa)	Normal anisotropy, $\bar{R}$
RT	47 ± 1.69	63 ± 2.05	13.05 ± 0.35	0.13	98 ± 3.29	0.56
180°C	41 ± 1.41	55 ± 1.69	18.50 ± 0.53	0.11	85 ± 2.49	0.66
220°C	37 ± 1.24	46 ± 2.44	21.89 ± 0.92	0.09	68 ± 2.16	0.79
300°C	29 ± 1.63	33 ± 1.88	25.45 ± 1.18	0.04	36 ± 2.35	0.91

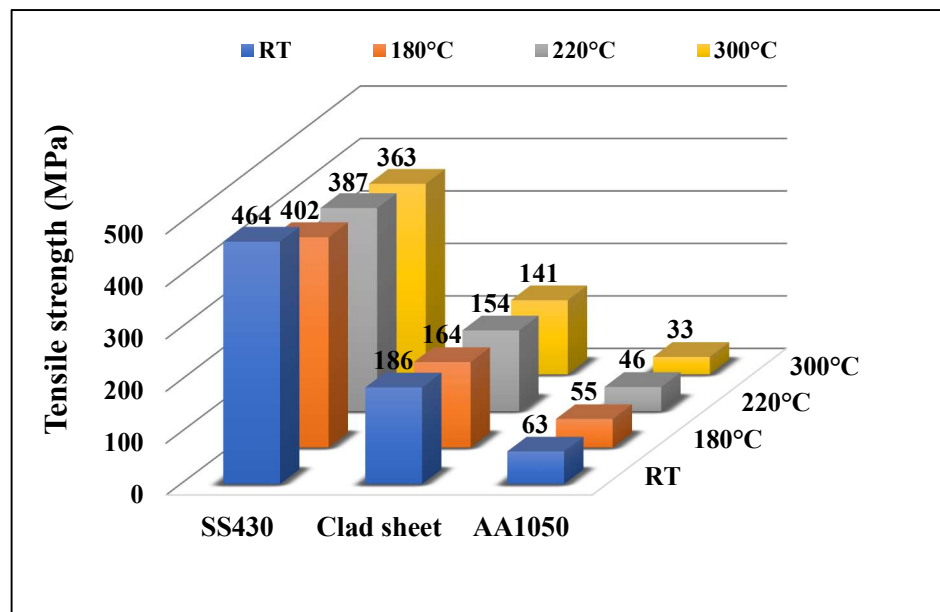


Fig. 6.3 Variation of tensile strength in clad sheet and parent layers with temperature

The normal anisotropy ( $\bar{R}$ ) is a key indicator of a material's ability to resist thickness reduction during deformation, and therefore serves as an important parameter for assessing deep drawability and overall sheet metal formability. For the SS430 layer, the  $\bar{R}$  value shows a significant increase from 1.13 at room temperature to 1.95 at 300 °C. This substantial rise implies that, at elevated temperatures, the stainless-steel layer becomes more resistant to thinning when subjected to tensile stresses in the thickness direction. Higher  $\bar{R}$  values are generally associated with improved deep drawing performance because the material tends to deform more in-plane rather than through thickness reduction. Consequently, the enhanced  $\bar{R}$  at 300 °C directly contributes to the increased formability of the SS430 layer.

In contrast, the aluminium layer (AA1050), although exhibiting a lower  $\bar{R}$  compared to the stainless-steel layer at all temperatures, also shows a positive temperature dependency. Its  $\bar{R}$  value increases from 0.56 at room temperature to 0.91 at 300 °C. While these values are lower overall, the upward trend indicates that aluminium likewise experiences improved resistance to thinning as temperature rises, enhancing its formability to a certain degree.

For the clad sheet, which combines the SS430 and AA1050 layers, the measured  $\bar{R}$  values fall between those of the two constituent materials. The clad structure also follows the same increasing trend with temperature, demonstrating that the combined material benefits from the improved anisotropy characteristics of both layers. Its  $\bar{R}$  value increases from 0.71 at room temperature to 1.10 at 300 °C.

This temperature-enhanced behaviour suggests that warm forming conditions can significantly improve the drawability and overall forming performance of the SS430/AA1050 clad sheet.

### 6.1.2 Residual stresses in Tensile tested 2-ply clad sheet

The residual stress measurement in the material based on the  $\cos \alpha$  method is estimated by mapping the Debye ring as depicted in Fig. 6.4. The nature of residual stress (tensile or compressive) significantly influences the material's response to plastic deformation and is therefore a critical factor in its mechanical characterization. The variation of the residual stresses in SS and AA layers of the deformed clad samples at different temperatures is shown in Fig. 6.5. It is observed that the residual stresses on the SS layer are compressive in nature, and that of AA layer is tensile in nature in the temperature range from room temperature to 300°C.

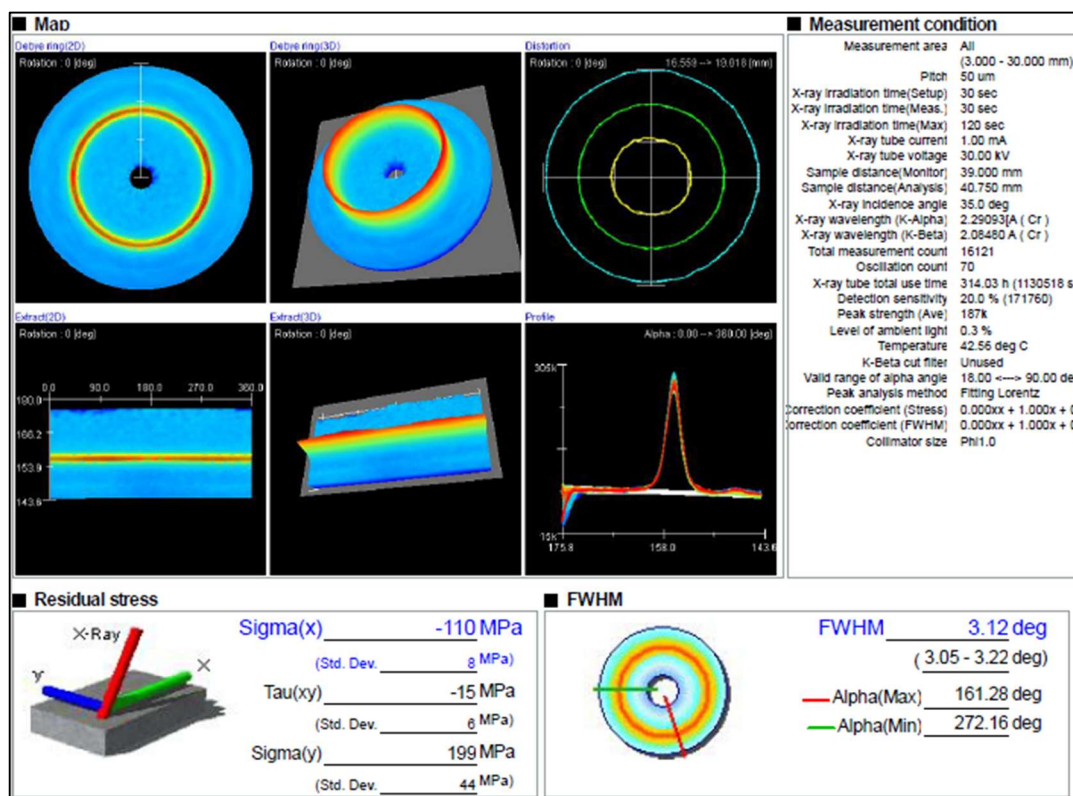


Fig. 6.4 Debye ring and measurement condition for the residual stress measurement in the SS layer of the clad sheet.

This behaviour in the clad sheet is attributed to the higher elastic recovery of the aluminium layer after deformation due to its lower Young's modulus. In contrast, with its higher Young's modulus and lower elastic recovery, the stainless steel layer limits

the extent of elastic recovery in the aluminium by imposing a mechanical constraint, resulting in the tensile nature of residual stress in the AA layer. The residual stress in the SS layer (compressive) decreases from 129 MPa at room temperature to 77 MPa at 300°C. The AA layer (tensile) also showed a similar trend of residual stress, with 26 MPa at room temperature to 9 MPa at 300°C. The lowering of the residual stresses is attributed to the decrease in tensile strength values of the material as the temperature increases [111].

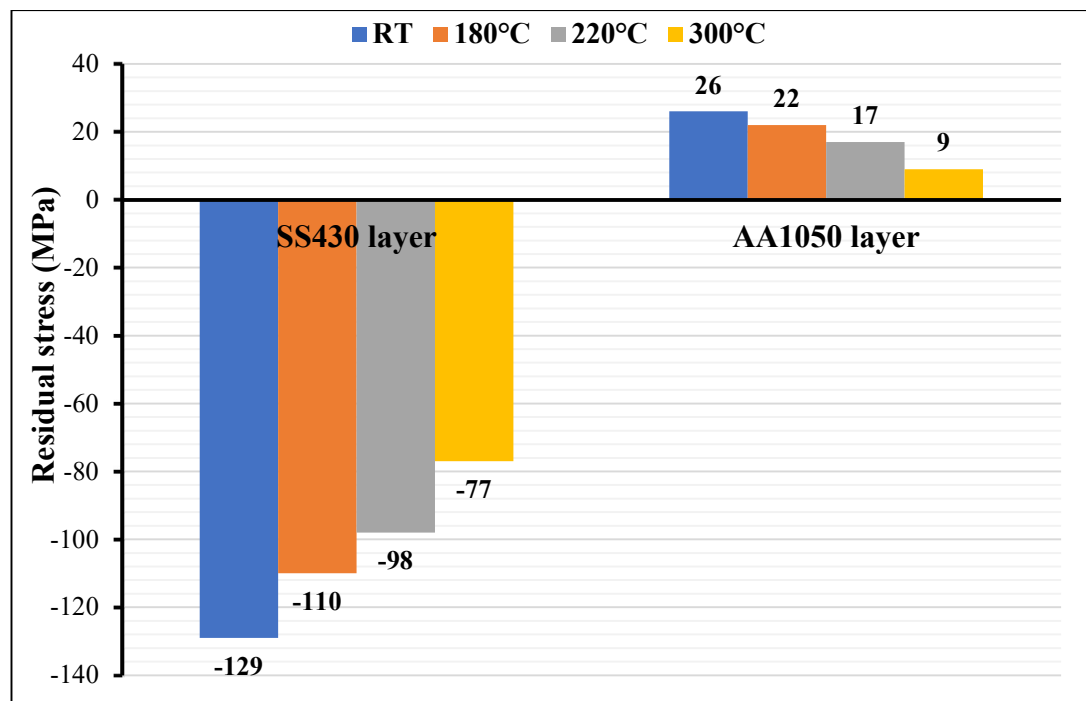


Fig. 6.5 The residual stress values for SS and AA layers at different temperatures

### 6.1.3 Vickers micro-indentation hardness results in clad sheet

The distribution of the micro-indentation Vickers hardness values for the SS430 and AA1050 layers at the four test temperatures is presented in Fig. 6.6. At room temperature, the SS layer exhibits a hardness of 171.66 HV0.5, while the AA layer shows a considerably lower hardness of 38.54 HV0.5, reflecting the inherent difference in mechanical strength between stainless steel and aluminium. As the



temperature increases, both materials experience a progressive reduction in hardness, indicating thermal softening. The Vickers hardness value is inversely proportional to the square of the indent diagonal length. At the room temperature, the average diagonal length of SS430 and AA1050 is 70  $\mu\text{m}$  and 155  $\mu\text{m}$ , respectively, as shown in Fig. 6.7. A Higher indent size indicates that the material plastically deformed by a larger amount, hence a lower value of hardness is observed. At 300 °C, the SS layer shows an overall decrease of approximately 12% in hardness relative to its room-temperature value, whereas the AA layer undergoes a more pronounced reduction of about 51%. This marked decline in the aluminium layer highlights its greater susceptibility to temperature-induced softening compared to the stainless-steel layer.

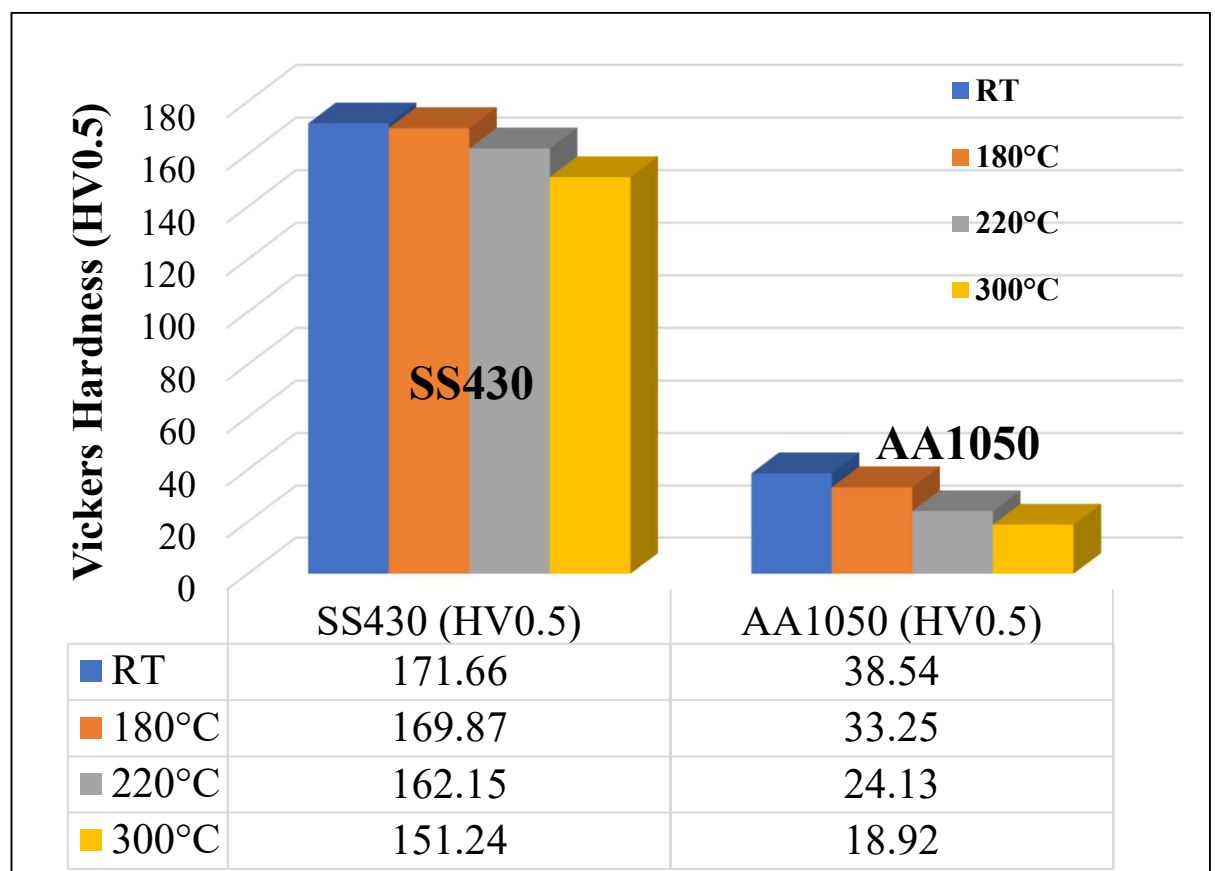


Fig. 6.6 Micro-indentation hardness values for SS and AA layers at different temperatures

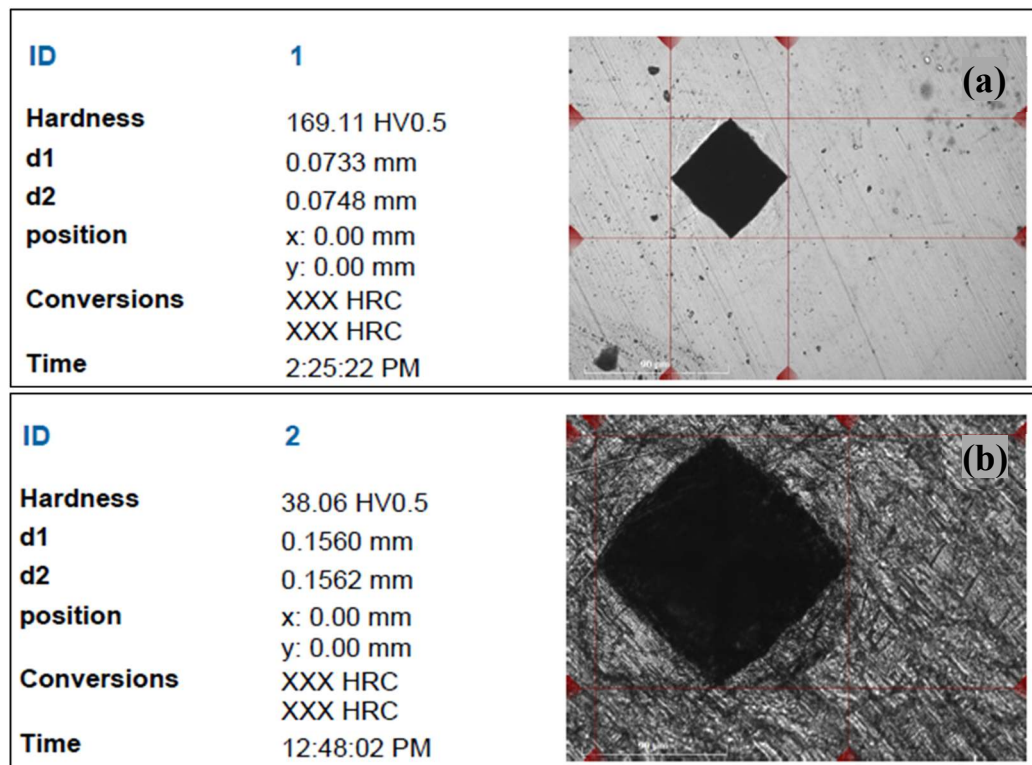


Fig. 6.7 Micro-indentation formed after Vickers hardness test for (a) SS430, and (b) AA1050

The reduction in hardness with increasing temperature is directly associated with the drop in material strength [112]. Elevated temperatures promote enhanced atomic mobility, recovery, and partial annihilation of dislocations, leading to a softer microstructure and diminished resistance to indentation. Consequently, the decreasing hardness values reflect the reduced load-bearing capability of both layers under warm forming conditions. These trends are consistent with the temperature-dependent stress strain behaviour of both materials and play an important role in understanding the mechanical response and formability of the SS/AA clad sheet at elevated temperatures.

#### 6.1.4 Coefficient of friction results of both layers of clad sheet

The results of the coefficient of friction (COF) of the steel and aluminium layers at different temperature is shown in Fig. 6.8 and Fig. 6.9. The detailed COF values at all temperatures for both materials, under no lubrication and MoS<sub>2</sub> lubrication, are

presented in Table 6.4. The COF of both layers of the clad sheet is determined in order to analyse the influence of friction on the formability of sheet metal in forming limit diagram and limiting draw ratio at different temperatures. The coefficient of friction value of AA1050 was observed to be higher than the SS430 layer in dry condition. The friction values reduced significantly under the MoS<sub>2</sub> lubrication condition. The friction values increased with increase in temperature, with COF value of 0.42 for aluminium layer at 300°C in dry condition due to softening behaviour of AA layer.

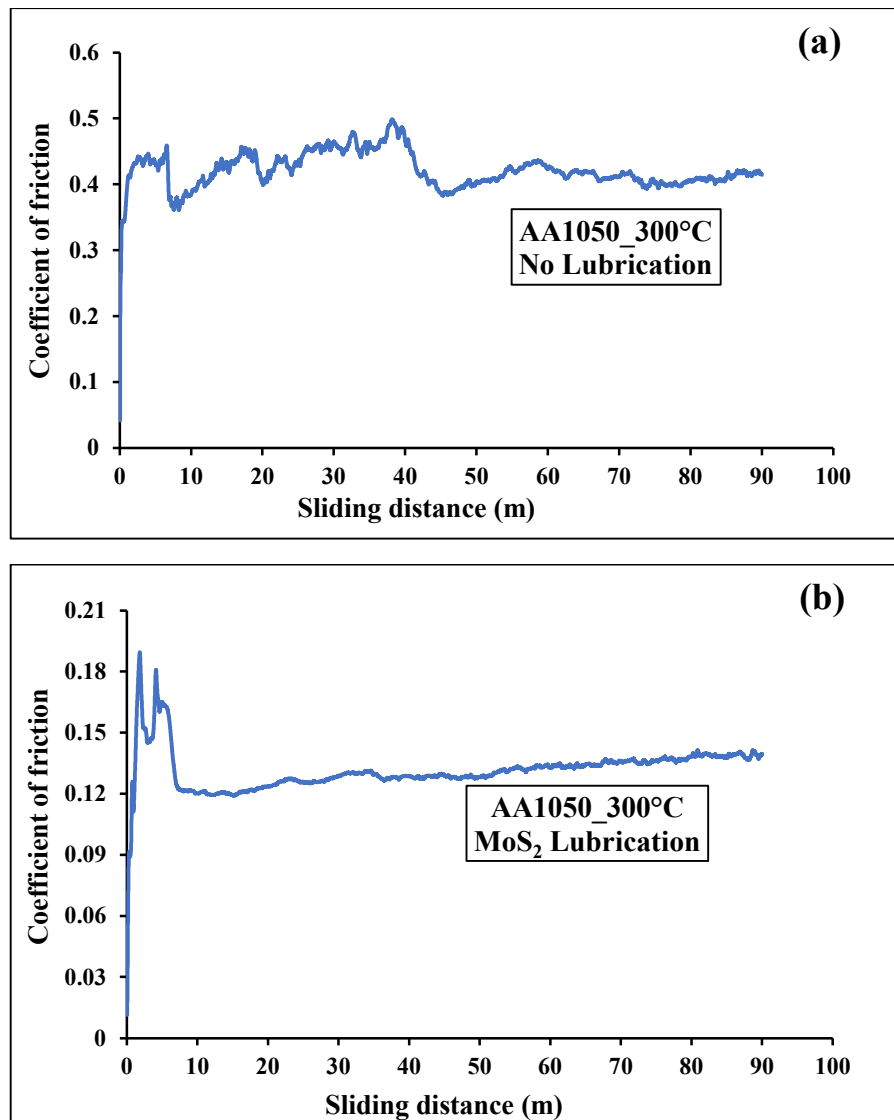


Fig. 6.8 Coefficient of friction plot of AA050 layer under (a) no lubrication, and (b) MoS<sub>2</sub> lubrication at 300°C

This value of friction can lead to sticking friction between the sheet and tools during deep drawing and stretching operations. The friction value of aluminium layer at 300°C with lubrication reduced to 0.13. In the case of SS layer at 300 °C, the friction values are also found to reduce from 0.21 under dry condition without lubrication to 0.1 with lubrication.

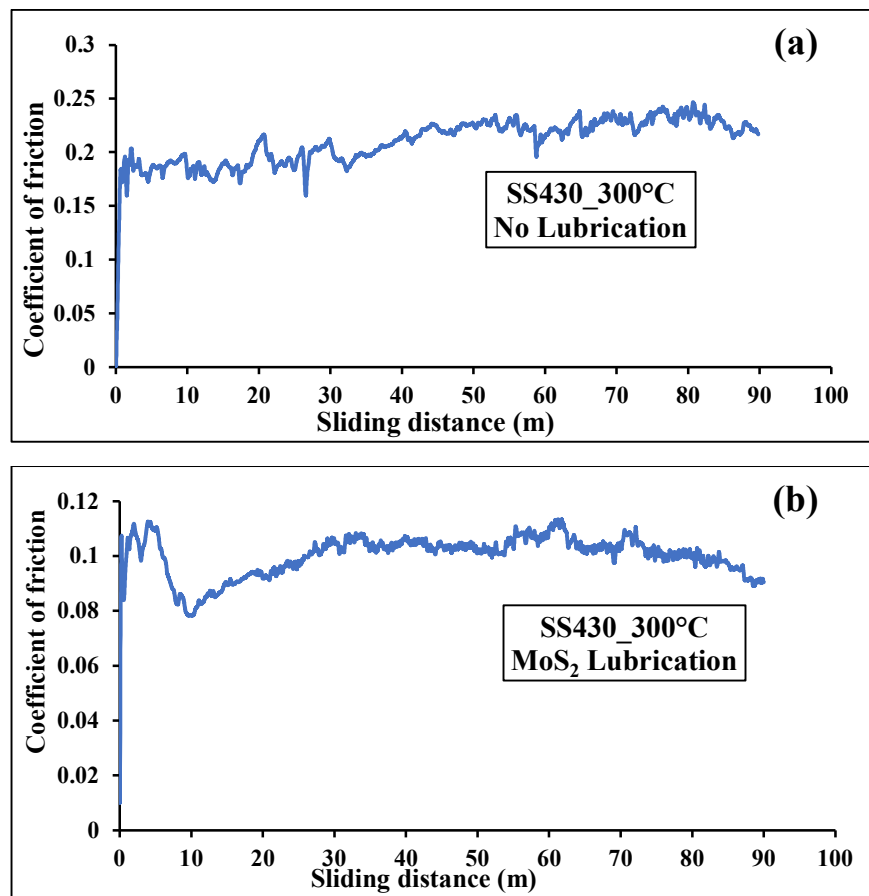


Fig. 6.9 Coefficient of friction plot of SS430 layer under (a) no lubrication, and (b) MoS<sub>2</sub> lubrication at 300°C

Table 6.4 Coefficient of friction values of both materials under different lubricating condition.

Temperature	Coefficient of friction			
	SS430		AA1050	
	No Lubrication	MoS <sub>2</sub> Lubrication	No Lubrication	MoS <sub>2</sub> Lubrication
RT	0.08	0.06	0.12	0.09
180°C	0.10	0.06	0.19	0.10
220°C	0.17	0.09	0.31	0.11
300°C	0.21	0.10	0.42	0.13

## 6.2 Microstructural analysis of the 2-ply clad sheet

### 6.2.1 Microstructure of the parent and the interface layer

The microstructure of the interface region of the as received clad sheet, using EBSD technique is shown in Fig. 6.10 (a). The average grain size of the aluminium and stainless steel components in clad sheet is 33.75  $\mu\text{m}$  and 12.62  $\mu\text{m}$ , respectively. The much elongated grains of aluminium are observed to line up in the direction of plane of the sheet. This indicates that the material's deformation behaviour will vary depending on whether it is examined parallel or perpendicular to the sheet thickness. In the case of SS, the grains are much finer and more or less equiaxed. These grains are observed to be finest nearer to the transition zone. A significant deformation experienced at the interface during cladding is responsible for the development of fine grains (1–2  $\mu\text{m}$ ) in the joint/ transition region. The metallurgical bond is primarily driven by the aluminium side, where elongated and heavily deformed AA grains mechanically interlock with the crevices in the layer of SS430. In contrast, SS430 grains remain equiaxed and contribute minimally to interfacial bonding. The thickness of the interface region is about 118  $\mu\text{m}$ . The interface region exhibits extremely fine grains with a flat or linear boundary pattern. The linear bond interface is a feature of the hot-roll bonding method [84].

Fig. 6.10 (b) shows the microstructure of a 20% deformed clad sheet at room temperature. The grains are seen to be further elongated and the average grain size decreased to 32.54  $\mu\text{m}$  and 10.8  $\mu\text{m}$  for aluminium and steel, respectively. The thickness of the interface region reduced to 77  $\mu\text{m}$ . Fig. 6.10 (c) shows the microstructure of the 20% deformed clad sheet at 300°C.



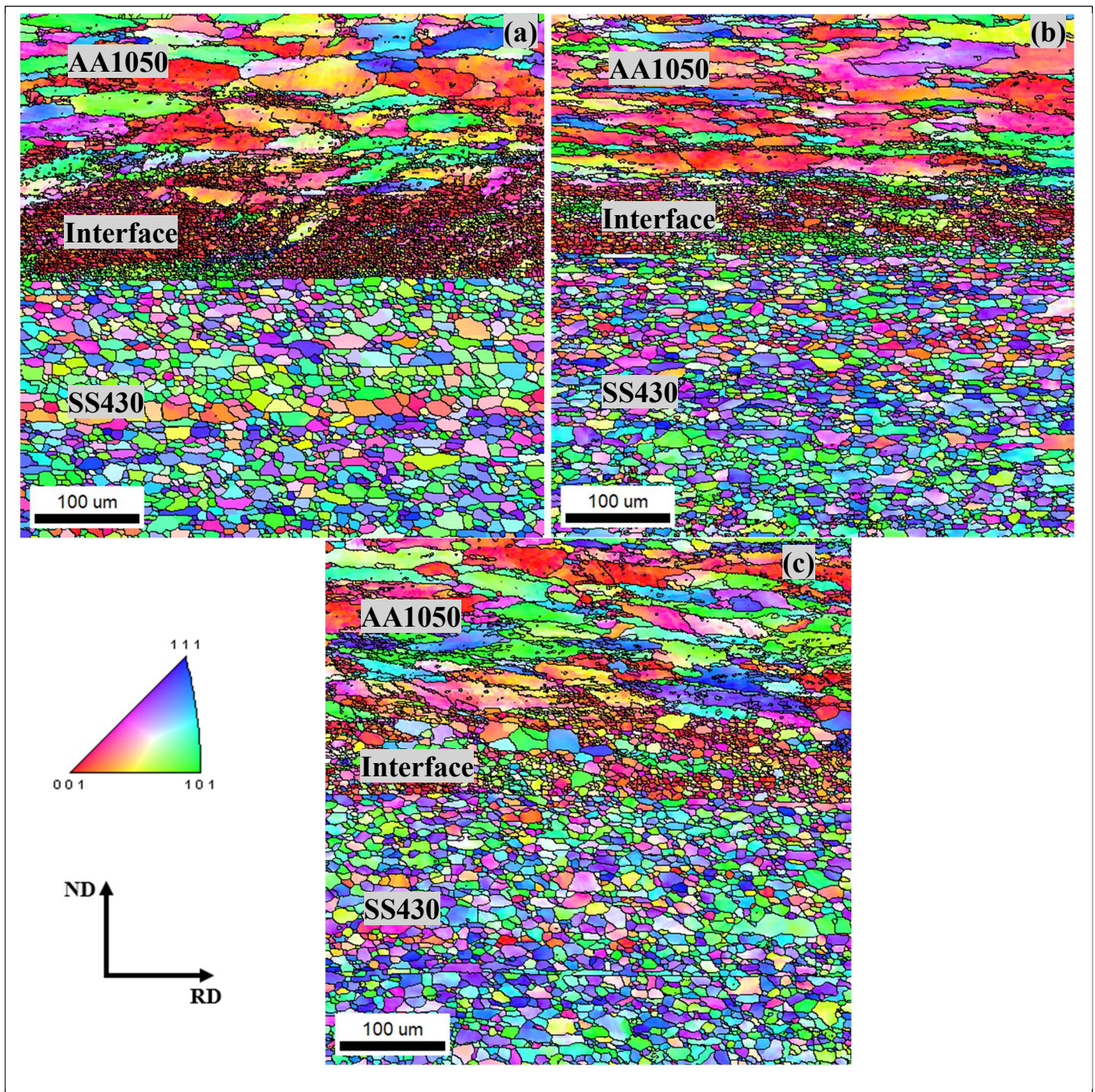


Fig. 6.10. Microstructure of the (a) As-received clad sheet, (b) 20% deformed clad sheet at room temperature and (c) 20% deformed clad sheet at 300°C

In this case also, the grains are elongated in the direction of applied load and the average grain sizes are found to be 36.64 μm and 13.08 μm for aluminium and steel, respectively. The thickness of the interface region is observed to be 84 μm which is



slightly higher than that of the value at room temperature.

### 6.2.2 Inverse pole figures

The inverse pole figure (IPF) maps are shown in the Fig. 6.11. The IPF of the as received clad sheet shows that the grains in AA1050 are oriented along the (001) plane in the [001] direction having a texture intensity in terms of multiples of random distribution (MRD) of 4.980 MRD, whereas the SS430 exhibit a weak texture of 2.165 MRD with grains oriented along the (111) plane in the [100] direction.

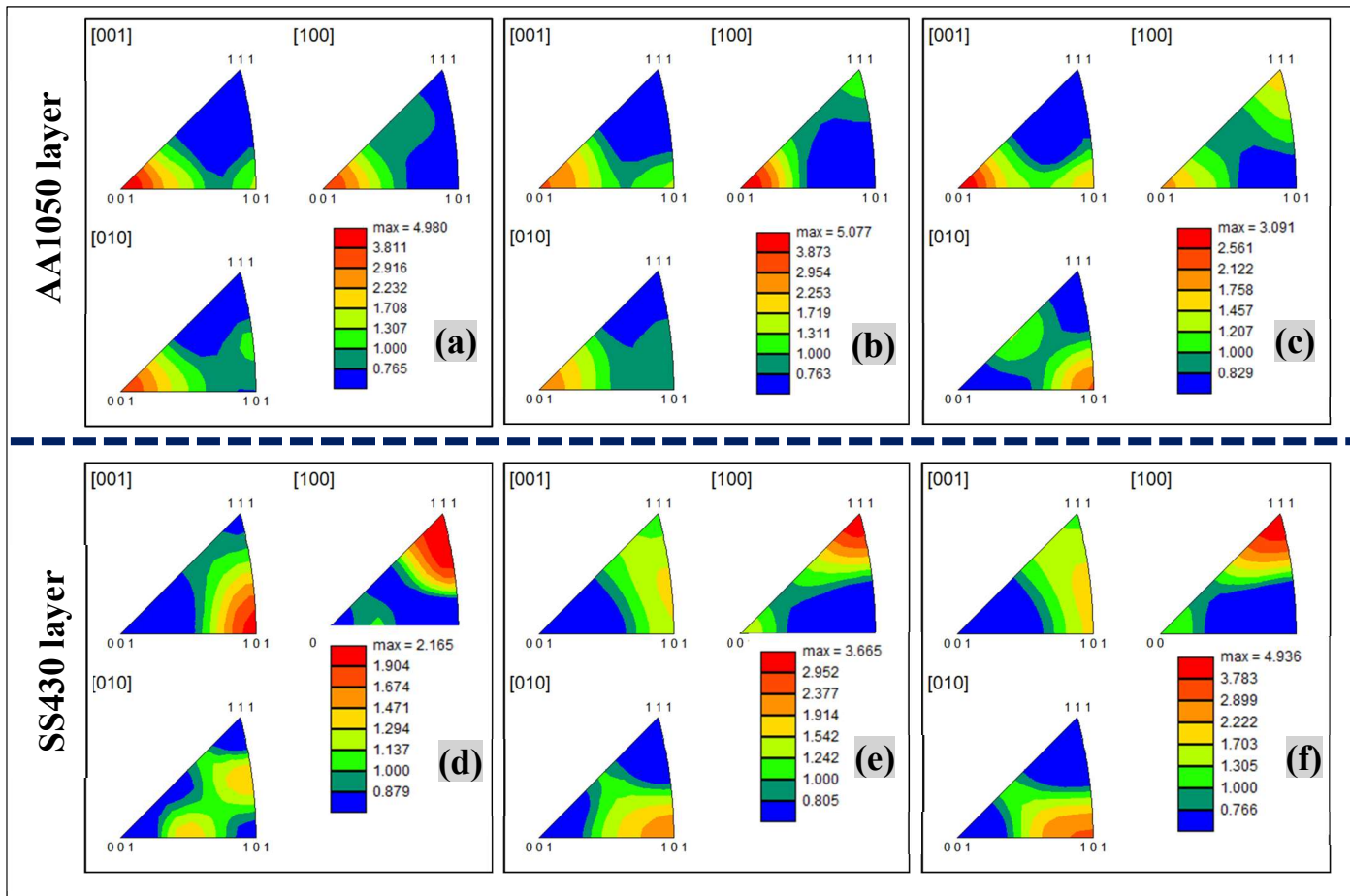


Fig. 6.11. IPF of the AA and SS layers of (a), (d) As-received clad sheet; (b), (e) 20% deformed clad sheet at room temperature and (c), (f) 20% deformed clad sheet at 300°C

The deformed clad sheet at room temperature shows an increase in texture intensity in both of the materials. The texture intensity in aluminium increased to 5.077 MRD along the (001) plane in the [100] direction, and the intensity of the SS430 increased

to 3.665 MRD along the (111) plane in the [100] direction. The deformed clad sheet at 300°C shows that the texture intensity of aluminium decreases to 3.091 MRD along the (001) plane in the [001] direction. This decrease indicates more random grain orientation in the microstructure attributed to the increased grain boundary mobility and recrystallization at elevated temperature, which finally results in an increase in ductility of the aluminium layer. Whereas, the texture intensity of SS430 in the deformed clad sheet at 300°C shows increased texture intensity of 4.936 MRD along the (111) plane in the [100] direction, indicating more grains are aligned in a particular direction, which can lead to anisotropic deformation and reduced ductility.

The AA1050 layer of the as-received clad sheet consists of elongated, rolling-textured grains with high dislocation density, whereas the SS430 layer exhibits finer, equiaxed grains with weak texture. This difference in microstructural features determines the initial mechanical response to plastic deformation; AA1050 provides little strength but a considerable ductility, whereas SS430 carries the majority of the load due to its higher modulus of elasticity adding stiffness to the clad sheet. After deformation at room temperature, both layers exhibit work hardening. In AA1050, the grains are further elongated with pronounced intragranular misorientations, indicating the accumulation of dislocations and the formation of substructures, resulting in a higher value of flow stress. Similarly, SS430 develops higher dislocation density after deformation indicating increased flow stress. After deformation at 300°C, the two layers evolve in different ways. AA1050 undergoes recovery and partial recrystallization, resulting in equiaxed grains with a weaker texture and reduced dislocation density. This transformation reduces yield strength considerably while increasing ductility. On the other hand, deformation in SS430 at high temperatures,



results in less intragranular misorientation and more equiaxed grains. At 300°C, the texture intensity of SS430 increases along the (111) plane in the [100] direction, indicating that more grains are aligned in a specific direction, potentially resulting in anisotropic deformation. The annihilation of dislocations in SS430 leads to a lowering of strength values. The strong texture of the material leads to higher normal anisotropy of SS430 at elevated temperature with reduced ductility.

### 6.2.3 Misorientation angles (LAGB and HAGB)

The high-angle grain boundaries (HAGBs) are grain boundaries with a misorientation angle above 15°, while low-angle grain boundaries (LAGBs) possess angles ranging from 1° to 5°. The gray-shaded grains in the grain boundary map signify the recrystallized, strain-free crystals exhibiting minimal dislocations [113].

The EBSD measurement as shown in Fig. 6.12 reveals that the fraction of HAGBs is 77.9%, while that of LAGBs is 22.1% in the SS430 layer of the clad sheet. The microstructure of SS430 is predominantly strain-free and recrystallized. The AA1050 layer comprises 32.2% HAGBs and 67.8% LAGBs. The elevated proportion of LAGB in AA1050 indicates that the aluminium component significantly contributes during hot roll bonding as the deformation in the form of dislocations have transformed into the LAGBs at the sub-grain boundaries of aluminium. The interface region has HAGB concentrated region adjacent to SS430 (zone I) and LAGB concentrated region is adjacent to AA1050 (zone II). The presence of higher fraction of HAGB in zone I impedes the movement of dislocation in this particular region. The microstructure of the 20% elongated clad sheet at RT reveals that the AA1050 grains are further elongated, exhibiting an average grain size of 32.57 µm, while the SS430 displays elongated grains with a reduced grain size of 10.53 µm.



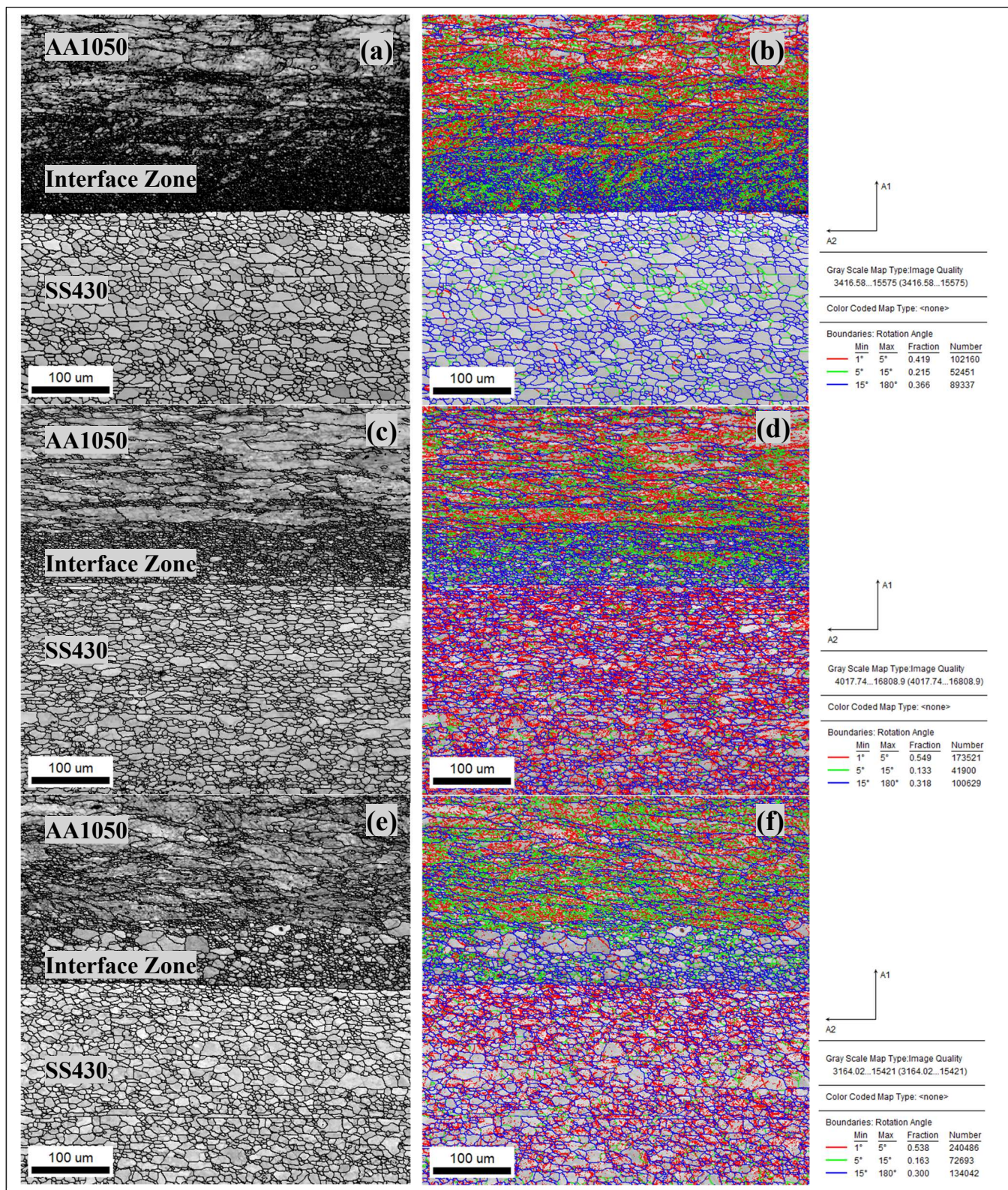


Fig. 6.12. Microstructure, and grain boundary map of interface region of the (a)-(b) as received clad sheet, (c)-(d) 20% plastic strained at RT, (e)-(f) 20% plastic strained at 300°C.



The SS430 layer comprises 27.2% HAGBs and 72.8% LAGBs, whereas the AA1050 layer consists of 27.5% HAGBs and 72.5% LAGBs after the deformation at RT.

At 300°C, the microstructure of the sample tested to 20% plastic strain revealed that the grain size of AA1050 layer grew to 36.71  $\mu\text{m}$  with elongated grains, whereas the grain size of SS430 layer increased to 12.01  $\mu\text{m}$  with mostly equiaxed grains. The SS430 layer has 30.6% HAGBs and 69.4% LAGBs, whereas the AA1050 layer consists of 24.9% HAGBs and 75.1% LAGBs following deformation at 300°C. The 3.4% rise in the fraction of high-angle grain boundaries in SS430 layer reflects a reduction in ductility at elevated temperatures, as HAGBs impede dislocation movement during deformation. But the HAGBs percentage in AA1050 layer decreases by 2.6%, demonstrating an easy movement of dislocations at elevated temperatures, thereby enhancing ductility.

#### **6.2.4 Geometrically necessary dislocations (GND) density**

The geometrically necessary dislocations (GND) density ( $10^{12} / \text{m}^2$ ) map as shown in Fig. 6.13, results from the necessity for adjusting with the lattice curvature during non-uniform plastic deformation. It has less influence on the plastic strain but rather contributes to the work hardening of the material. The GND density distribution plot (Fig. 6.14) shows the average dislocations in the SS430 and AA1050 for as received sheet is  $204 \times 10^{12} / \text{m}^2$  and  $305 \times 10^{12} / \text{m}^2$  respectively. This magnitude of the density in the SS430 and AA1050 components increases drastically after the deformation at room temperature to  $705 \times 10^{12} / \text{m}^2$  and  $385 \times 10^{12} / \text{m}^2$  respectively. Furthermore, the GND density decreases to  $626 \times 10^{12} / \text{m}^2$  and  $323 \times 10^{12} / \text{m}^2$  for SS430 and AA1050 components respectively after the deformation at 300°C.

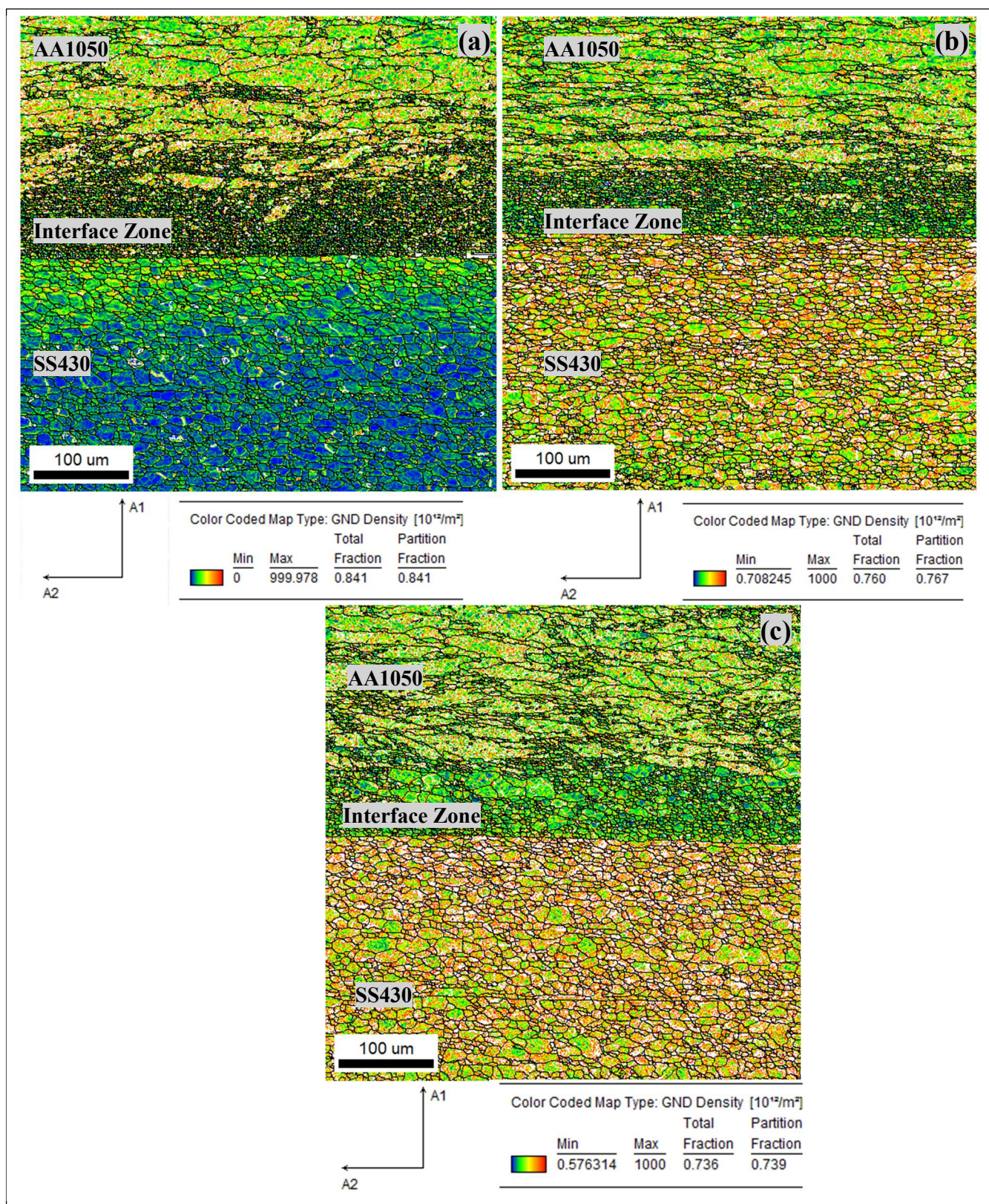


Fig. 6.13 GND map of clad sheet: (a) as received, (b) 20% plastic strained at RT, (c) 20% plastic strained at 300°C.



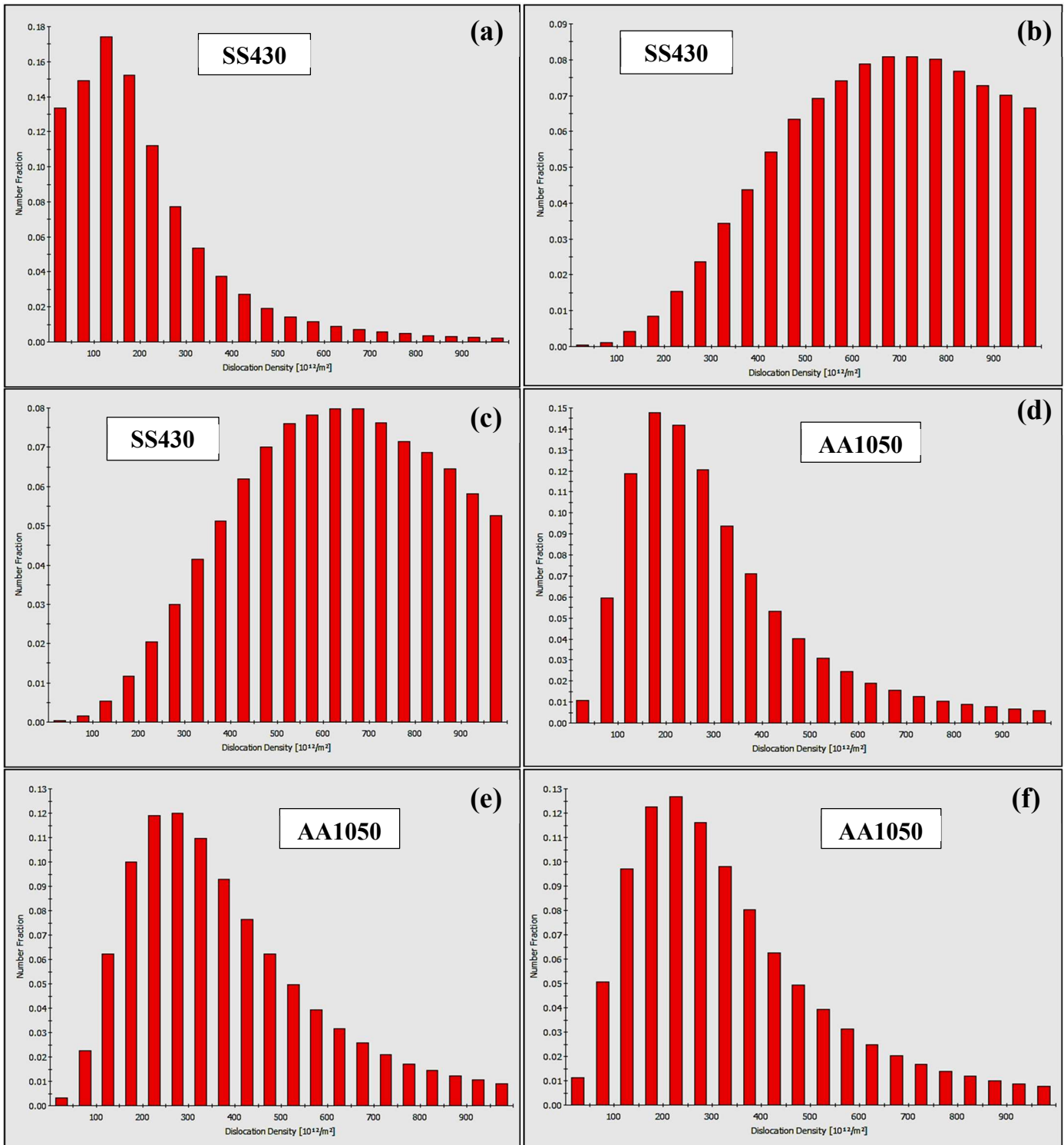


Fig. 6.14 GND density ( $10^{12}/m^2$ ) distribution plot of SS430 and AA1050 for (a), (d) as received sheet; (b), (e) 20% plastic strained at RT; (c), (f) 20% plastic strained at 300°C.

This decrease in the total GND density is due the annihilation of the dislocations under recovery conditions at the elevated temperatures. The reduced total dislocations tend

to reduce the barriers for the dislocation motion, resulting in the reduction of the strength values. The decrease in the yield and tensile strength values of the clad sheet and the parent layers at elevated temperatures is primarily attributed to the reduction of the total dislocation density due to the dislocation annihilation.

### 6.2.5 Fractography and SEM-EDAX

The elemental profile plot of the SS/AA clad interface is obtained via SEM-EDAX method as shown in Fig. 6.15. The section on the left-hand side of the plot represents the SS430 layer, whereas the rightmost section corresponds to the AA1050 layer. The interface region, measuring approximately 139  $\mu\text{m}$  in total width, is partitioned into two zones. Zone I is abundant in elements, including Fe, Cr, and Mn, situated adjacent to the SS430 layer as a result of element diffusion in the area, which occurred during the roll bonding of the SS/AA clad sheet. The Zone II is characterized by a high aluminium content and which is susceptible to failure, situated next to AA1050 layer. The presence of alloying elements in zone I of the interface makes it stronger than Zone II. Due to this reason several attempts to separate the SS430 and AA1050 layers through a peel test performed as per ASTM D1876 standard to determine the bond strength have been unsuccessful. Repeatedly, the bond failed from the zone II of the interface, leaving behind a layer of zone I on the SS430 having the aluminium texture appearing on the surface.

Moreover, during the tensile test the clad specimens exhibits a delamination crack at the zone II of the clad interface as shown in Fig. 6.16(a)-(d). The diffuse necking and localised necking appears at the same location on the both SS and AA side along the longitudinal axis of the tensile specimen, as the interface region between the two layers significantly influences the concurrent occurrence of the necking region.

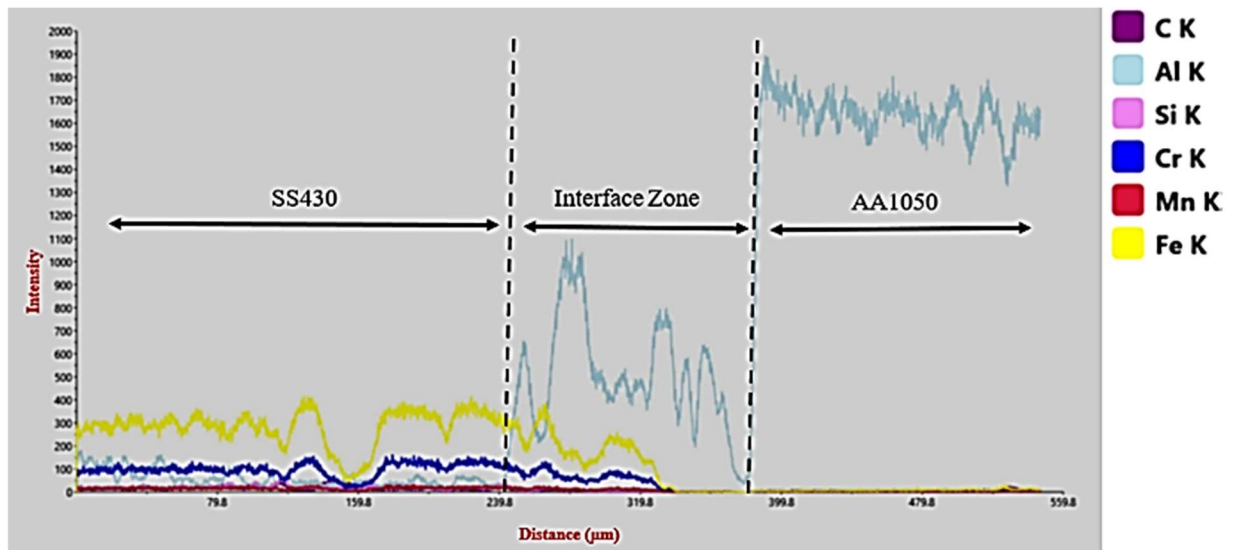


Fig. 6.15. Elemental profile plot of SS/AA clad interface

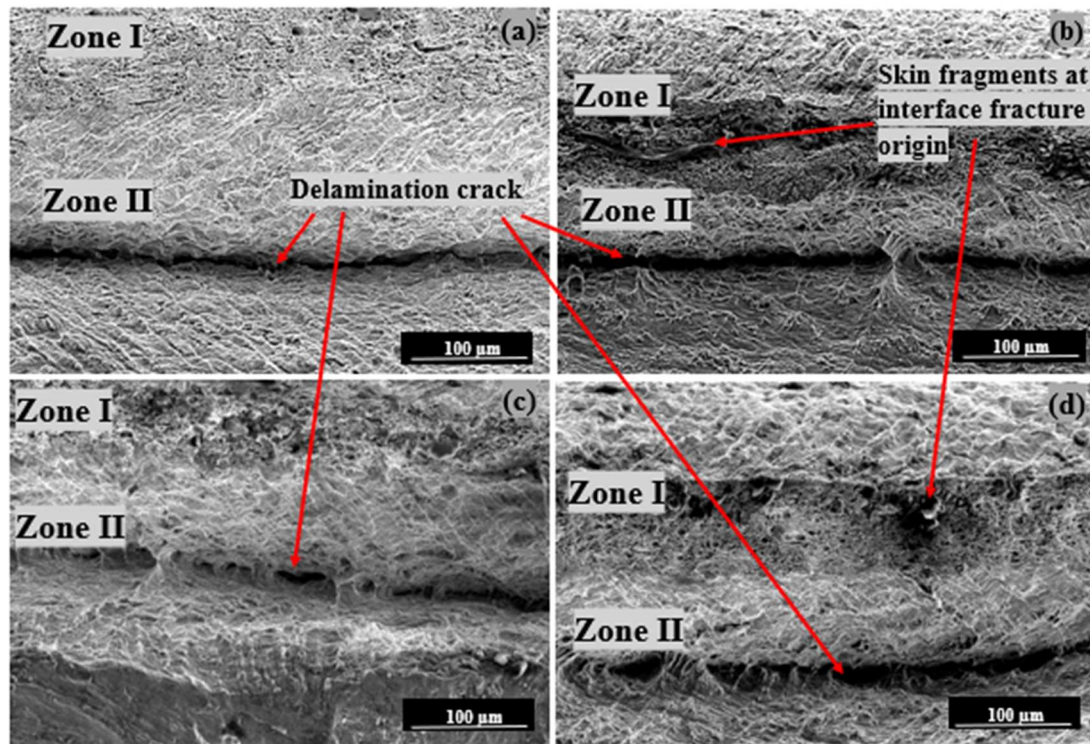


Fig. 6.16. Fractographs of SS430/AA1050 interface at (a) RT, (b) 180°C, (c) 220°C, and (d) 300°C.

Diffuse necking is the instability point at which strain hardening is counterbalanced by geometric softening due to a reduction in the specimen's cross-sectional area. The secondary point of instability is localized necking, corresponding to a plane strain deformation, implying there is no change in the width and the strain is confined to

reduction in thickness. The width of the diffuse necking region is decreasing with rising temperature as illustrated in Fig. 6.17, correlating with the reduction in ductility. The diffuse necking width is greater on the AA side of the clad sheet than on the SS side, attributing to an enhanced geometric softening of aluminium layer. The width of localised necking is equal to the layer thickness in the SS side and double the sheet layer thickness on aluminium side. No substantial change in the localized necking width is observed due to temperature effects; nevertheless, the angle of the localized necking band relative to the longitudinal axis decreases from  $73.32^\circ$  at RT to  $67.21^\circ$  at  $300^\circ\text{C}$ .

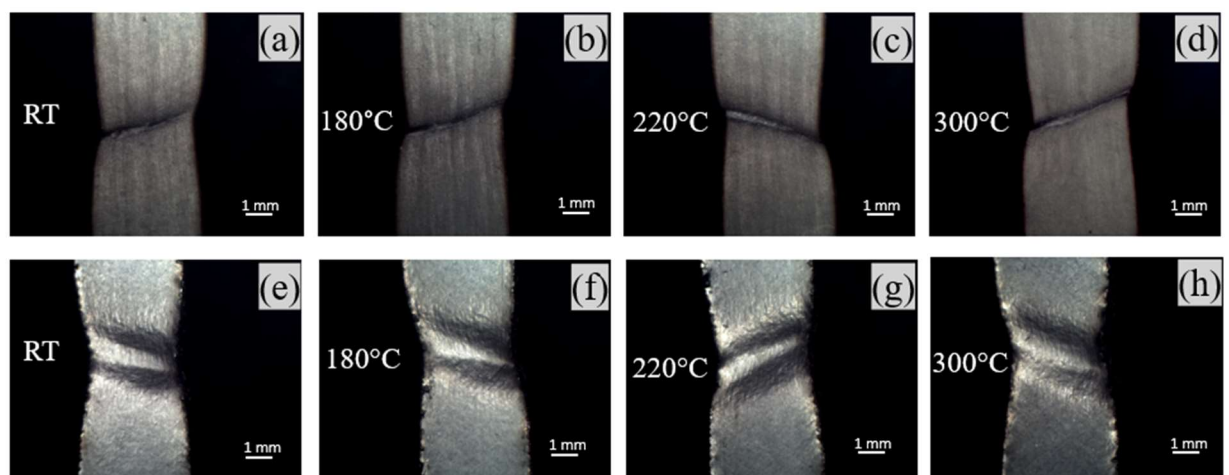


Fig. 6.17. Necking region in tensile specimen on the (a)-(d) SS430 side, (e)-(h) AA1050 side, of the clad sheet at different temperatures.

Localized necking is followed by a fracture. The fracture appears to originate from the interface zone to the either side of the bonding region. The fractographs indicate that at room temperature, the fracture exhibits a mixed form, characterized by microscopic microvoids (ductile fracture) in zone I and a river pattern (brittle fracture) in zone II. As the temperature rises, the cleavage facets in Zone I become more apparent, indicating a greater incorporation of alloying elements due to diffusion.



## 6.3 Formability analysis

### 6.3.1 Forming limit diagram of clad sheet

The major and minor strains are measured from the safe and necked regions of aluminium-stainless steel clad sheet samples subjected to the FLD experiments as shown in Fig. 6.18. In all the experiments, aluminium layer remains in contact with the punch, while the stainless steel layer forms the outer surface of the dome. Strain measurements are conducted on the stainless steel surface to determine the forming limit strains of the clad sheet and the strains are plotted using the failure strains.



Fig. 6.18. Test FLD specimens of 2-ply clad sheet with steel as outer layer of dome

This study investigates the influence of friction on the FLD of the clad sheet under no lubrication conditions at various temperatures. The coefficient of friction between the sheet and forming tools, like other mechanical properties, significantly affects the material's formability. Fig. 6.19(a) presents the FLD of the clad sheet under dry conditions at room temperature (RT), 180 °C, 220 °C, and 300 °C. The limit strains initially increased with increase in the temperature to 180°C.

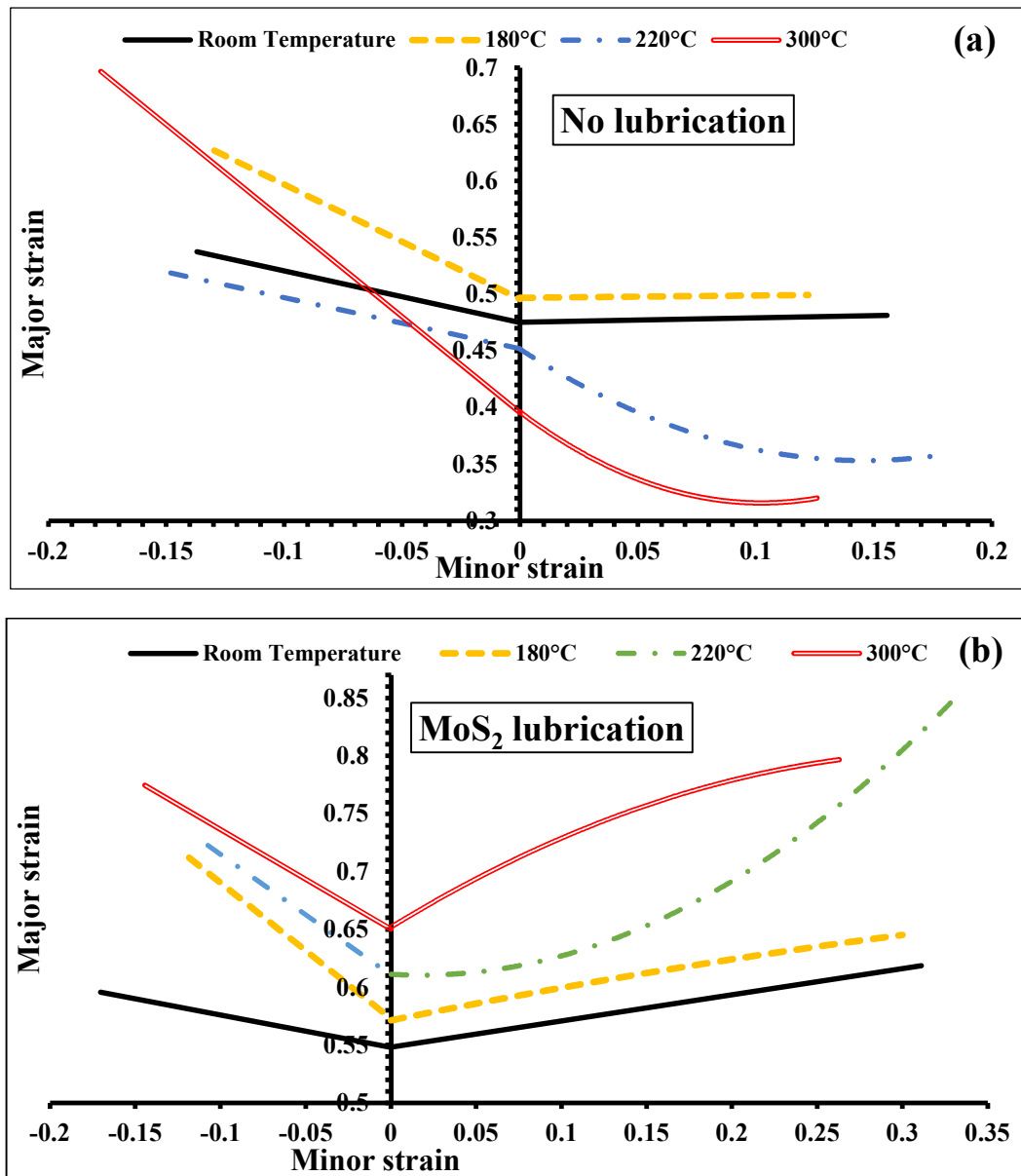


Fig. 6.19. Forming limit diagram of clad sheet at different temperatures with (a) no lubrication and (b) lubrication condition

Specifically, the major strain at the plane strain condition (FLD<sub>0</sub>) increases from 0.47 at RT to 0.49 at 180 °C. However, as the temperature increases further to 220 °C and 300 °C, the FLD<sub>0</sub> decreases to 0.45 and 0.39, respectively. This reduction in forming limits is attributed to increased frictional resistance at higher temperatures, which restricts material flow during the plane strain condition.

Across all tested temperatures, the right-hand side of the FLD, corresponding to the

tension-tension deformation mode, consistently exhibits a negative slope. This indicates that as the major strain increases, the minor strain decreases, resulting in higher major strain values near the plane strain condition compared to those observed under biaxial tension.

Table 6.5 Dome heights of the LDH tested specimens under no lubrication condition.

Sample width (mm)	Dome height (mm)- No Lubrication			
	RT	180°C	220°C	300°C
10	18.46	18.64	17.38	18.92
20	16.64	18.00	17.58	18.68
30	17.66	16.44	17.62	17.88
40	17.62	18.40	18.40	18.68
50	16.64	16.96	16.42	15.72
60	16.12	14.86	15.80	16.46
70	16.74	15.62	14.12	14.14
80	16.50	15.36	14.54	15.84
90	15.00	14.58	14.90	15.32
100	14.84	15.08	15.26	14.74

Table 6.6 Dome heights of the LDH tested specimens under MoS<sub>2</sub> lubrication condition.

Sample width (mm)	Dome height (mm)- MoS <sub>2</sub> Lubrication			
	RT	180°C	220°C	300°C
10	20.56	21.38	21.98	22.16
20	18.76	21.32	16.68	20.26
30	20.28	20.22	17.94	19.84
40	17.42	17.98	20.40	19.70
50	16.96	17.24	18.84	19.60
60	18.46	16.46	16.38	19.00
70	19.64	16.30	18.66	18.06
80	19.84	17.90	20.74	18.72
90	19.28	21.14	20.52	17.72
100	18.90	19.98	19.14	20.54

Fig. 6.19(b) presents the FLD of the clad sheet with MoS<sub>2</sub> lubrication applied between the blank and the forming punch. The limit strains under lubricated conditions increase significantly at all temperatures when compared to those under dry conditions. The FLD<sub>0</sub> values at room temperature and 180 °C are 0.54 and 0.57, respectively, representing an average increase of approximately 15% compared to the dry condition.

At elevated temperatures of 220 °C and 300 °C, the  $FLD_0$  values further increase to 0.61 and 0.65, respectively, an average improvement of about 53% over the corresponding dry conditions. The FLD curves obtained under lubrication exhibit a positive slope in the tension-tension deformation region across all temperatures, indicating improved formability under biaxial stretching.

Additionally, dome heights recorded from the LDH tests under  $MoS_2$  lubrication are consistently higher than those obtained under dry conditions, as given in Table 6.5 and Table 6.6. The plane strain specimens at all temperatures and under both lubricating condition is shown in Fig. 6.20. It is also observed that the necking region on the LDH specimens shifts toward the pole of the formed dome under lubricated conditions, in contrast to its location under dry conditions. This shift further confirms the enhanced material flow and delayed onset of localized necking due to the reduced friction at the tool-blank interface.

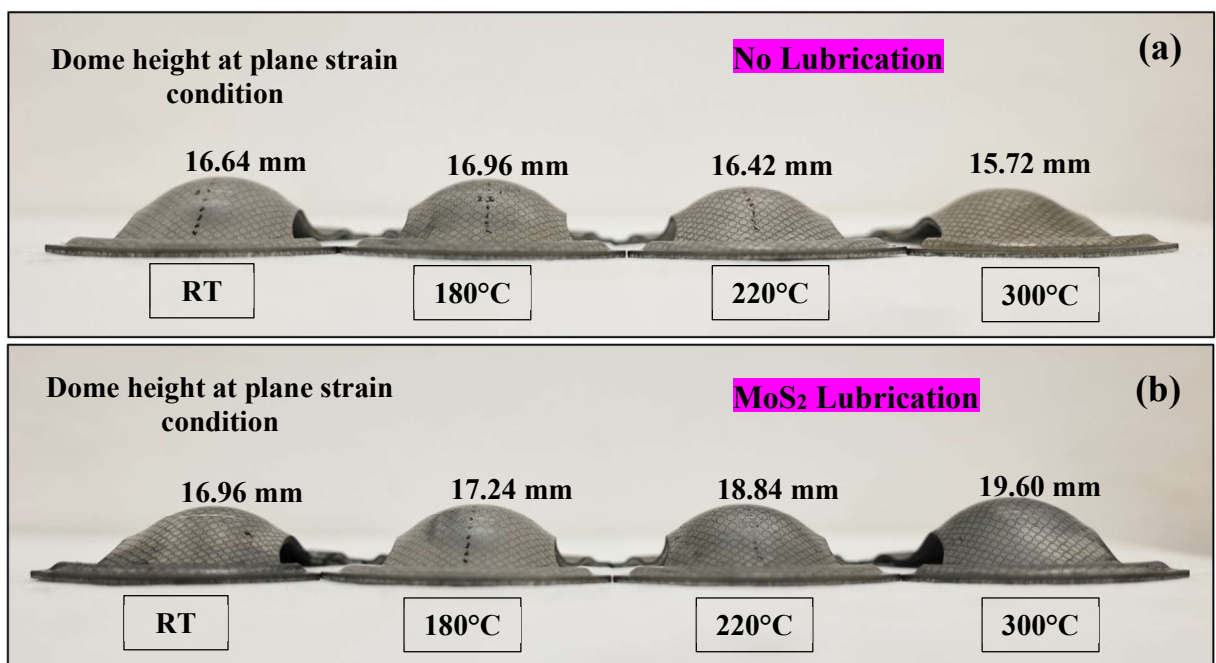


Fig. 6.20. Plane strain specimens of the clad sheet from LDH test under (a) no lubrication and (b)  $MoS_2$  lubrication condition

### 6.3.2 Deep drawing analysis of clad sheet

Deep drawing experiments are conducted on the clad sheet with aluminium layer in the contact with punch, under two distinct conditions: with MoS<sub>2</sub> lubrication and without lubrication. The key indicator for drawability i.e. LDR, which represents the maximum blank diameter that can be drawn without failure, is determined under both lubrication and no lubrication condition at all four temperatures. The results clearly indicate that the application of lubrication significantly enhances the formability of the clad sheets.

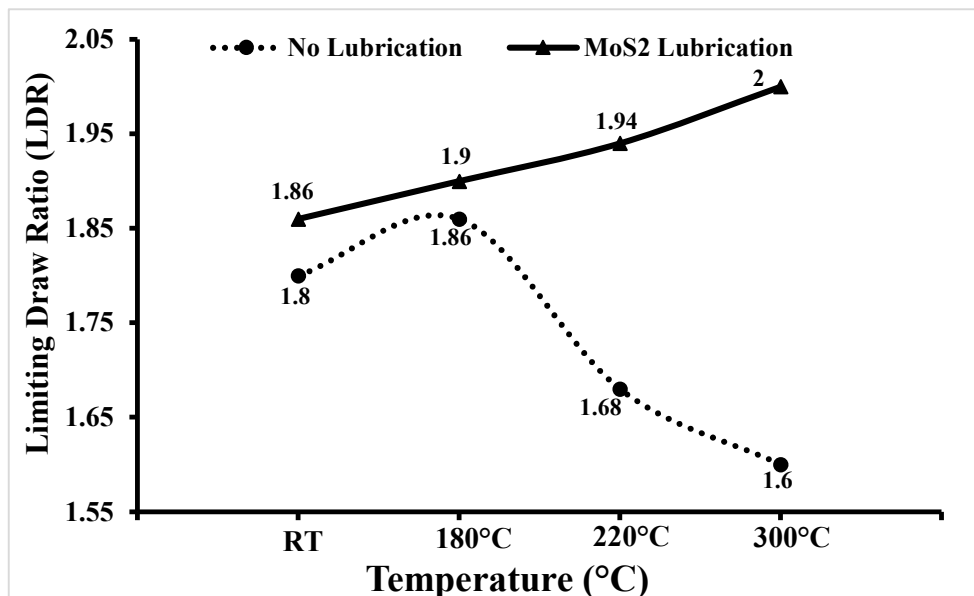


Fig. 6.21. Variation of LDR of the clad sheet with temperature under different lubricating conditions

Under lubricated conditions, a higher LDR was consistently achieved compared to the unlubricated conditions, as shown in Fig. 6.21. The LDR of the clad sheet in unlubricated condition at room temperature is 1.8, which increased to 1.86 when drawing is performed at 180°C. Further increasing the temperature showed a downward trend of the draw ratio.

This drop in the draw ratio is attributed to the increase in the sticking friction between



the die and blank interface. A comparison of the forming conditions revealed that lubrication significantly improved the LDR. When forming was performed at 220 °C, the LDR under lubrication was 15% higher than in the unlubricated state.

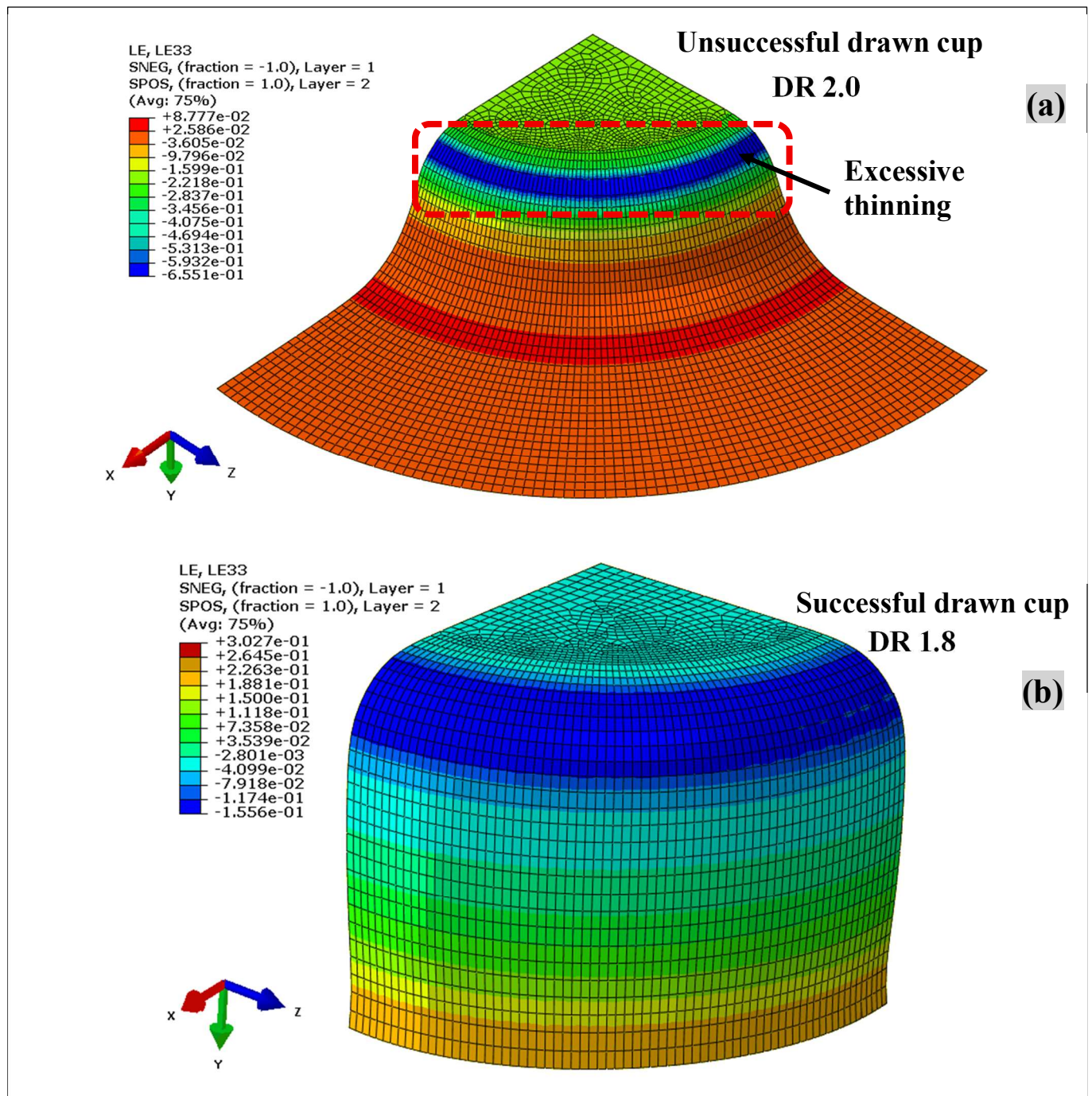


Fig. 6.22. FEA result of the deep drawing of clad sheet at RT under no lubrication with (a) draw ratio of 2.0 and (b) draw ratio of 1.8

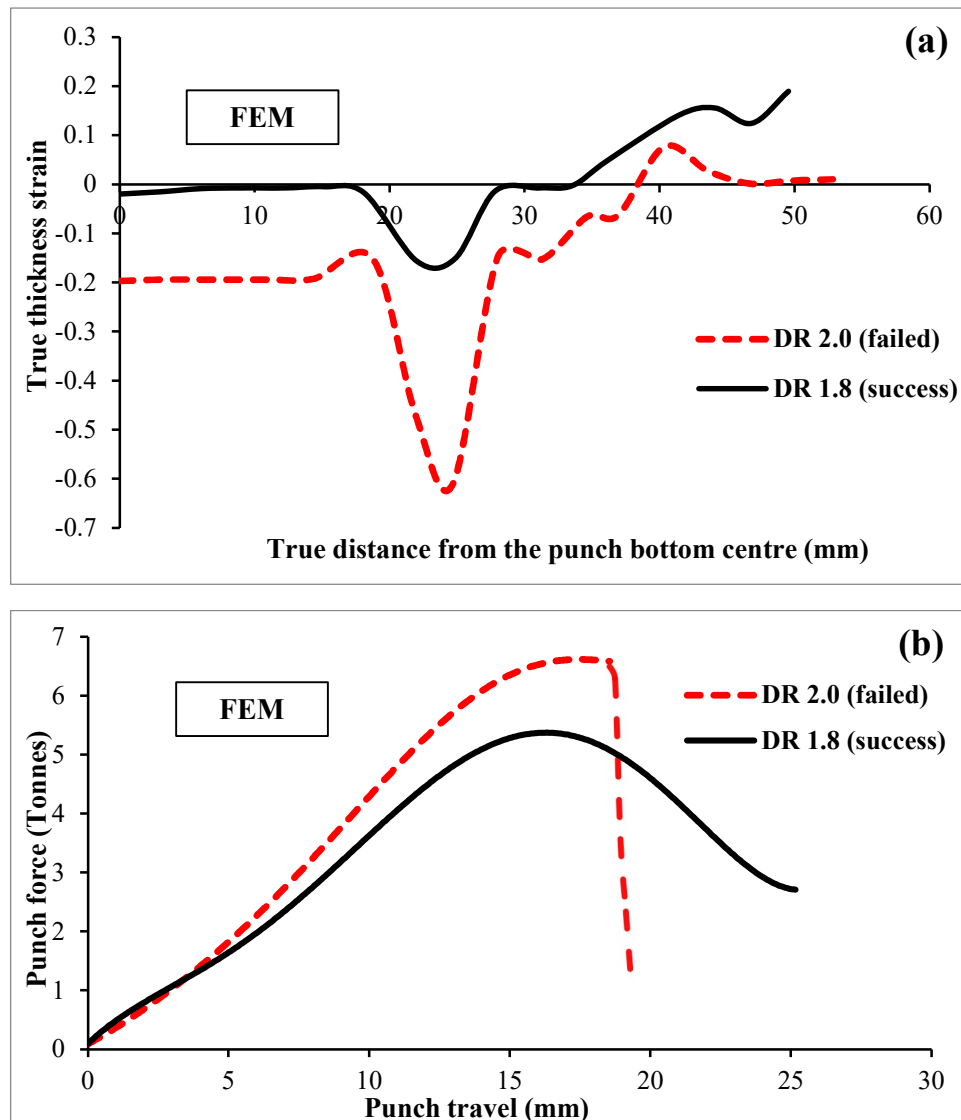


Fig. 6.23. FEA predictions of (a) true thickness strain distribution and (b) punch force plot, of the failed and successful drawn cup at RT under no lubrication

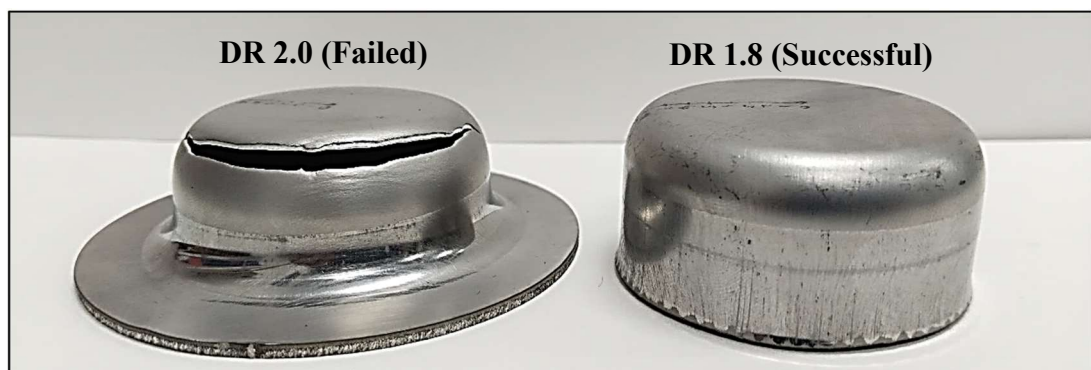


Fig. 6.24. Experimental result of the deep drawing of clad sheet at RT under no lubrication with draw ratio of 2.0 and 1.8



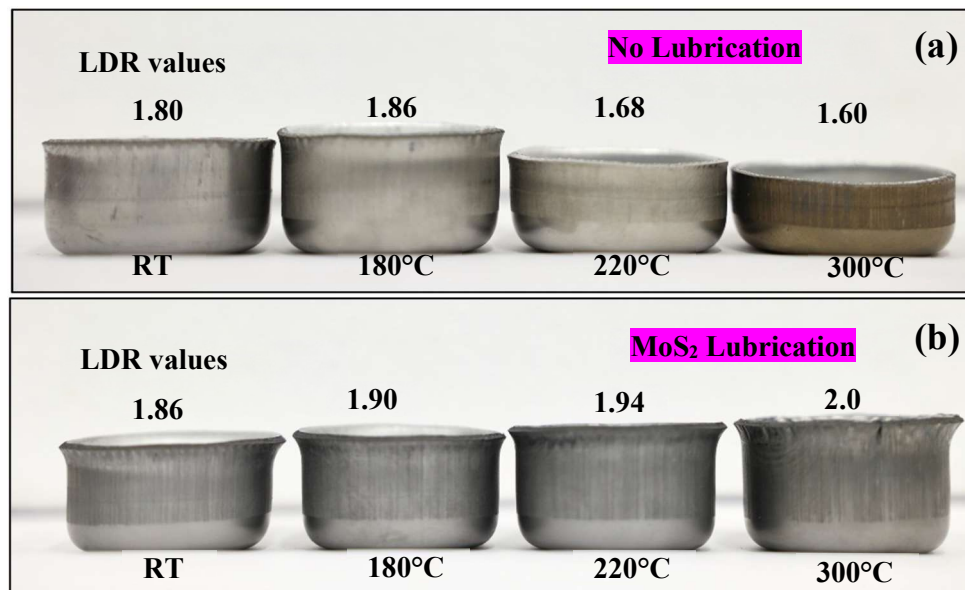


Fig. 6.25. Experimental result of LDR values at different temperature under (a) no lubrication and (b) MoS<sub>2</sub> lubrication

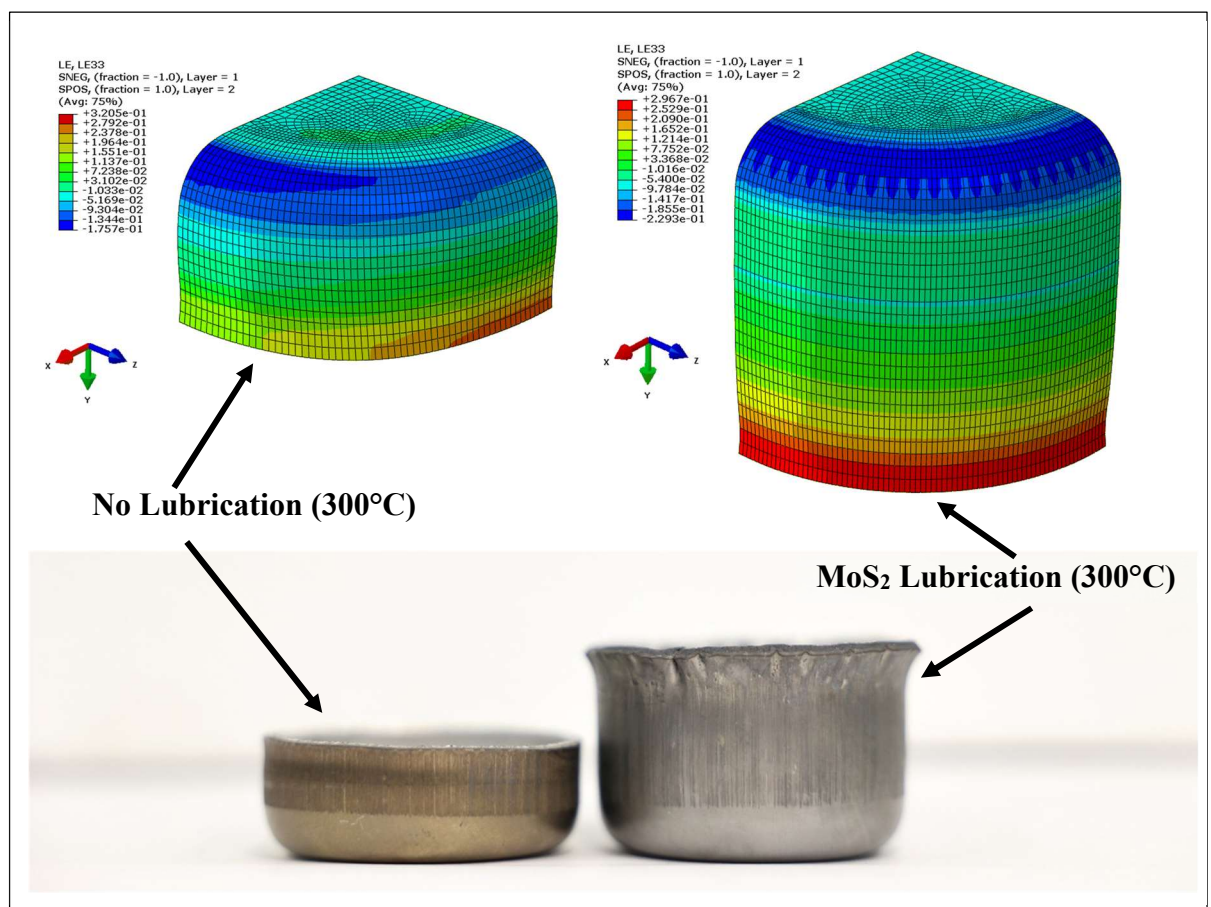


Fig. 6.26. Experimental and FEA results of deep drawn cups at 300°C under different lubricating conditions

Table 6.7. Maximum punch force of deep drawing specimens under no lubrication condition

<b>Maximum punch force (Tonnes)- No Lubrication</b>					
Temperature (°C)	Experimental (1)	Analytical (2)	FEM (3)	Error (%) (2) – (1) (1)	Error (%) (3) – (1) (1)
RT	4.91	5.12	5.26	4.28	2.73
180°C	4.14	4.41	4.08	6.52	-7.48
220°C	3.32	3.22	3.07	-3.01	-4.66
300°C	3.25	3.41	3.19	4.92	-6.45

Table 6.8. Maximum punch force of deep drawing specimens under MoS<sub>2</sub> lubrication condition

<b>Maximum punch force (Tonnes)- MoS<sub>2</sub> Lubrication</b>					
Temperature (°C)	Experimental (1)	Analytical (2)	FEM (3)	Error (%) (2) – (1) (1)	Error (%) (3) – (1) (1)
RT	5.48	5.28	5.01	-3.64	-5.11
180°C	4.71	4.67	4.3	-0.84	-7.92
220°C	4.52	4.45	4.98	-1.54	11.91
300°C	4.31	4.41	4.36	2.32	-1.13

This improvement further increased to 25% at 300 °C, indicating the positive influence of lubrication in reducing friction at the die-blank interface. The LDR is also predicted by the finite element analysis (FEA).

As shown in Fig. 6.22, the FEA of the deep drawing performed in unlubricated condition at room temperature failed at a draw ratio of 2.0. The blank is observed to be thinning excessively at the punch corner profile region. The true strain in the thickness direction at this region reached to a value of about -0.6 as shown in Fig. 6.23. Negative value of true strain indicates thinning. Any additional punch displacement beyond this point led to localized thinning at the particular element, indicating the onset of process instability and unsuccessful forming. Whereas the FEA performed with a draw ratio of 1.8 under same condition is completed with successful drawn cup.

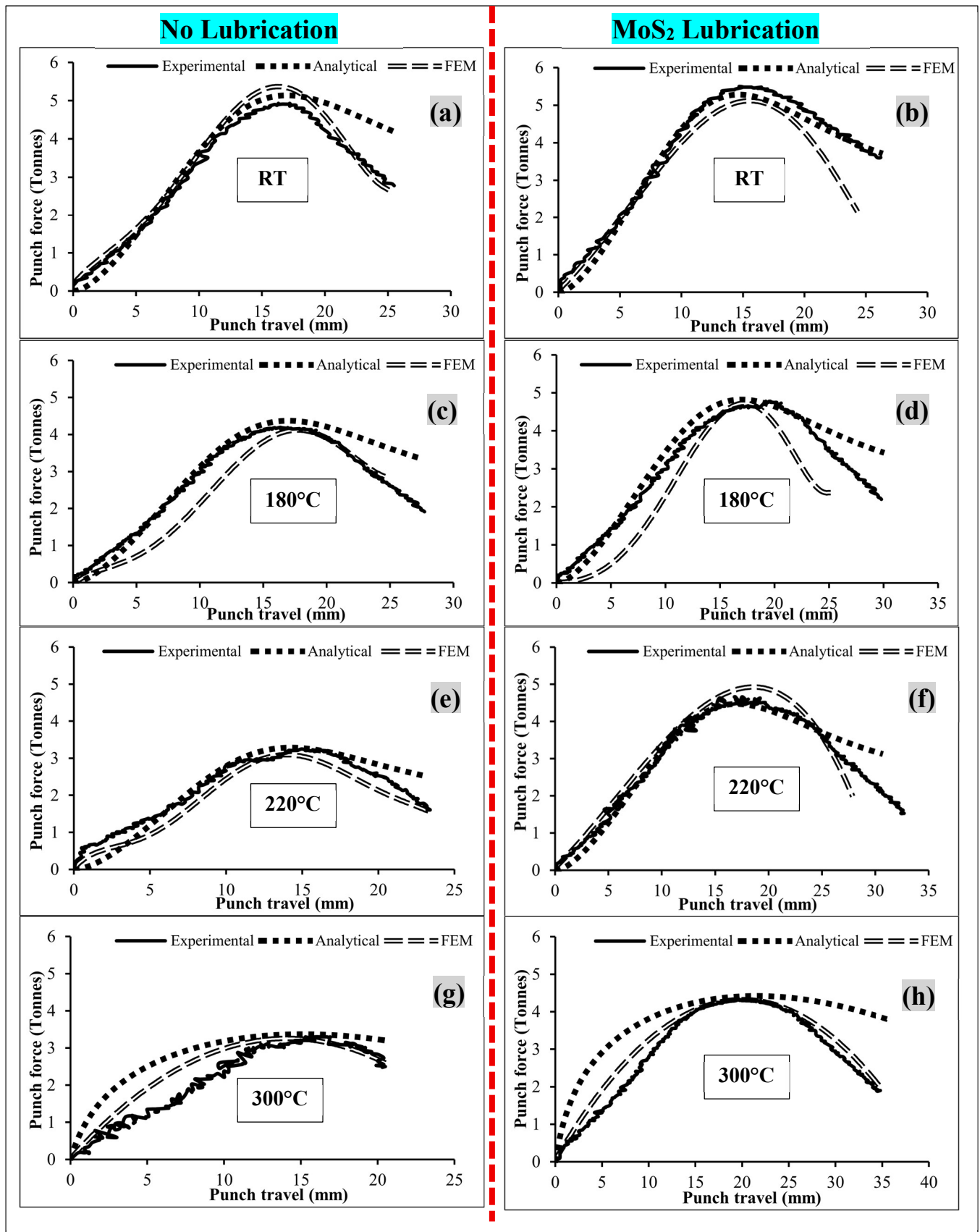


Fig. 6.27. Experimental and predicted punch force vs. travel plots for deep drawing

The validating experimental test specimen for the LDR at room temperature under dry condition is shown in Fig. 6.24. All the successful drawn cups in deep drawing operation at different temperature and both lubricating condition is shown in Fig. 6.25.

The maximum LDR of 2.0 is observed at 300 °C under lubrication, whereas the minimum LDR of 1.6 is also observed at 300 °C under dry condition. This highlights the critical role of controlling friction at the blank and tool interface to enhance formability during the forming process.

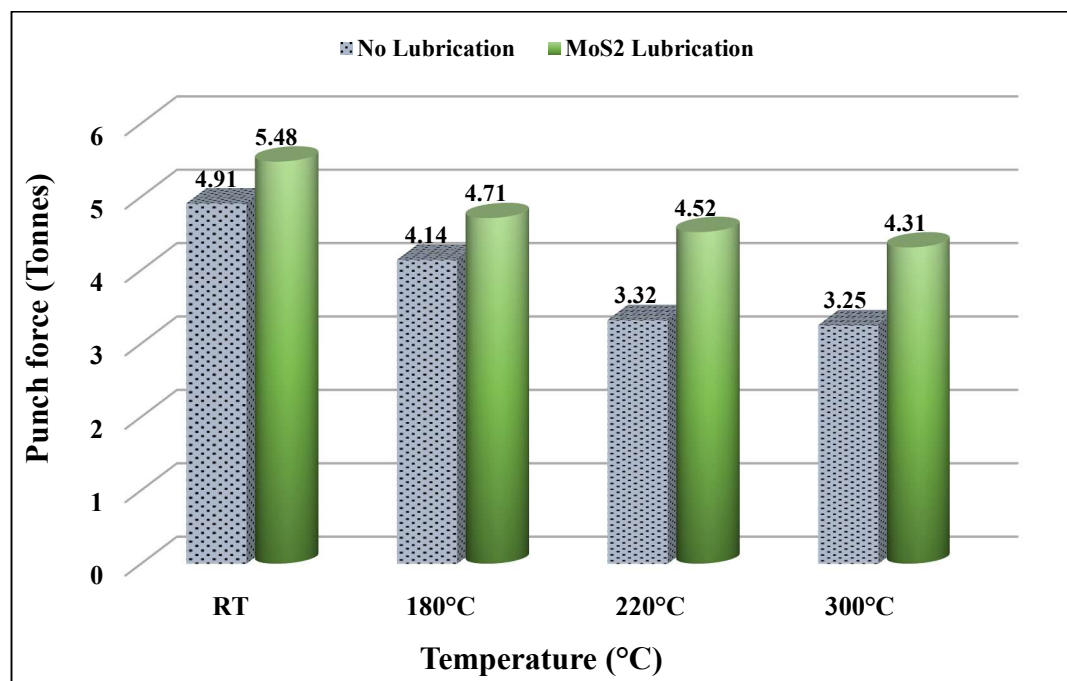


Fig. 6.28. Variation of maximum punch force for the LDR at different temperatures with and without lubrication.

The comparison of the cups formed through experimental and FEA at 300 °C under both lubricating condition is shown in Fig. 6.26. The punch force vs displacement predicted analytically and through FEA is compared with the experimental curve, as shown in Fig. 6.27. The maximum punch force predictions are in good agreement with the experimental results, as shown in Table. 6.7 and Table. 6.8. The relative error of the analytical prediction of the peak punch force with the experimental result is  $\pm 7\%$ ,

whereas this error is  $\pm 12\%$  for the results obtained by FEA prediction.

The variation in the results of maximum punch force obtained by experiments for the LDR at different temperatures and lubrication conditions is shown in Fig. 6.28. Without lubrication, the peak punch force for LDR at the room temperature is observed to be 4.91 tonnes. The punch force reduced to a value of 3.25 tonnes at a temperature of 300 °C. The peak punch force is observed to be reducing continuously as the temperature increases, which can be attributed to the reduction of the flow stress values of the clad sheet with an increase in temperature. A lower draw ratio indicates that less material will flow into the die cavity during drawing, resulting in reduced radial stress in the flange region, thereby lowering the required punch force. With MoS<sub>2</sub> lubrication condition, the punch force shows a similar reducing trend with increase in temperature due to softening of the material. Also, the LDR increases continuously with increase in temperature from 1.86 at RT to 2.0 at 300 °C. The punch force at elevated temperatures is also seen to reduce in spite of an increase in the LDR due to reduced flow stress of material and lower friction values between the die and blank. In the case of lubrication, as the LDR increases with temperature, the punch force is higher than in the case of no lubrication because more material flows into the die cavity, resulting in higher radial stresses in the flange region. The punch force, not only depends on the temperature, but rather on the draw ratio, interface friction, circumferential strain causing thickening and the resultant draw stress.

## 6.4 Summary

The mechanical and microstructural characterization of the SS430/AA1050 clad sheet across a temperature range from room temperature to 300°C reveals a clear inter-

dependence of thermal, mechanical, and microstructural characteristics. The tensile testing results indicate that both the yield and tensile strengths of the clad sheet decrease with increase in temperature, while ductility experiences a reduction. This reduction in strengths is attributed primarily to the decrease in dislocation density caused by thermally activated dislocation annihilation, as shown in GND density maps. The strain hardening exponent of the clad sheet increases from 0.20 to 0.23 with increase in temperature, indicating a greater tendency for uniform elongation at elevated temperatures despite the strength loss. This may be attributed to the deformation behaviour of SS430 layer at elevated temperature. In comparison, the SS430 layer retains its higher strength than that of the clad sheet at all temperatures, although its strength values decrease at higher temperatures, which is primarily attributed to the dislocation annihilation. The increase in HAGBs proportion with increase in temperature contribute to the decrease in ductility by limiting dislocation motion. Conversely, the AA1050 layer, shows a lower strength and demonstrates higher ductility at elevated temperature. This behaviour of aluminium layer correlates with its increasing fraction of LAGBs, suggesting easier dislocation movement at elevated temperatures. Microstructural observations show that after deformation at the interface, AA1050 has softened microstructure and reduced texture intensity at 300°C, while SS430 develops a stronger texture. These changes directly influence the sheet's deformation behavior.

Residual stress analysis using  $\cos \alpha$  method reveals compressive stress in the SS layer and tensile stress in the AA layer, which is attributed to the higher value of elastic recovery of the AA layer due to its lower Young's modulus compared to the SS layer. The residual stress of both the layers decreases with an increase in the temperature,

attributed to the reduction in the strength values at elevated temperatures.

The results obtained by Vickers micro-indentation follows the same trend, with a 12% and 51% hardness reduction in the SS430 and AA1050 layers, respectively. The friction behavior of the clad sheet showed a strong dependence on both material and temperature. The AA1050 layer consistently exhibited a higher coefficient of friction (COF) than the SS430 layer, reflecting its softer nature and greater tendency to adhere to the tooling surface. Under dry conditions, friction increased steadily with temperature, reaching a maximum COF of 0.42 for AA1050 at 300 °C, indicating a higher risk of sticking friction during warm forming. However, the application of MoS<sub>2</sub> lubrication substantially reduced the COF for both materials across all temperatures, effectively minimizing interfacial resistance and improving sheet–tool interaction during forming operations.

Elemental profiling across the interface region identifies two distinct zones: Zone I, rich in Fe, Cr, and Mn near the SS430 layer, and Zone II, dominated by Al near the AA1050 side. Zone I forms a stronger metallurgical bond due to elemental diffusion, whereas Zone II is weaker and prone to failure as observed during peel tests and tensile experiments, due to delamination initiation in the region. Necking analysis shows that diffuse necking decreases in width with increase in temperature and is more prominent on the AA side due to its greater softening. Localized necking remains largely unaffected in width but shifts in orientation with temperature rise, with fracture typically initiating near the interface. Fractography reveals mixed fracture modes: ductile micro void coalescence in Zone I and brittle river patterns in Zone II, with more pronounced cleavage at higher temperatures due to a higher diffusion of alloying element. Overall, the interplay of mechanical properties, microstructural evolution,



dislocation behaviour, and residual stresses provides a comprehensive understanding of the thermo-mechanical response of SS430/AA1050 clad sheets.

The forming limit diagrams reveal that under dry conditions, formability improves slightly up to 180°C but deteriorates at higher temperatures due to increased frictional resistance. In contrast, MoS<sub>2</sub> lubrication considerably enhances the forming limits at all temperatures, with major strain at plane strain increasing by more than 65% at 300°C and the onset of necking shifting closer to the pole of the dome, indicating improved material flow.

Deep drawing results similarly highlight the dominant role of lubrication and temperature. Without lubrication, the limiting draw ratio improves marginally at 180°C but decreases thereafter because of sticking friction. With MoS<sub>2</sub> lubrication, however, drawability improves substantially, achieving a maximum LDR of 2.0 at 300°C. Punch force decreases with temperature in both dry and lubricated conditions due to reduced flow stress, but lubricated conditions show higher punch forces overall because improved drawability allows larger blanks to be drawn successfully. Analytical predictions and finite element simulations closely match experimental punch-force trends, confirming the validity of the model. Overall, the results demonstrate that warm forming combined with effective lubrication significantly enhances the mechanical performance, stretchability, and drawability of the SS430/AA1050 clad sheet.

## **6.5 Industrial significance of the present work**

Experimental, analytical, and numerical studies on the punch force prediction of 2-ply laminate composite consisting of aluminium and stainless steel have significant industrial significance.

## 1. Punch Force Prediction and Control

The analytical and FEA models developed in this work enable accurate prediction of punch forces across different temperatures and lubrication conditions. This allows industries to design forming operations with greater confidence, control process loads, and prevent unexpected tool overload or component failure. Reliable force prediction also helps in selecting appropriate press capacity and ensures safe, consistent operation during mass production.

## 2. Process Optimization

The study provides clear insights into how temperature and lubrication influence formability, friction, and drawability of SS/AA clad sheets. Manufacturers can use this information to optimize forming parameters, including temperature settings, lubrication strategy, and draw ratio, to achieve better material flow and reduced defect rates. Understanding FLD and LDR behaviour further supports tuning of blank-holder forces and punch speeds for enhanced performance.

## 3. Material Selection and Design

The mechanical and microstructural characterization of SS430 and AA1050 at elevated temperatures helps engineers select suitable clad combinations for specific applications. Knowledge of how each layer responds to warm deformation enables smarter material design for components requiring strength on one side and thermal conductivity or ductility on the other. The research also assists in tailoring layer thicknesses and orientations for improved performance.

## 4. Cost and Time Savings

By showing that warm forming with MoS<sub>2</sub> lubrication reduces punch force, friction, and tool wear, the study highlights opportunities for significant cost savings. Industries

can lower maintenance frequency, extend tool life, and reduce energy consumption during forming. Additionally, the predictive models reduce trial-and-error during die development, speeding up process setup and minimizing scrap rates.

## **5. Quality Assurance**

Enhanced formability which is reflected in higher FLDs and improved drawability, translates directly into better part quality. The findings support the production of defect-free components with minimal thinning, tearing, or wrinkling. Reduced friction and controlled deformation help ensure dimensional accuracy and consistency, which are essential for automotive, cookware, and heat-transfer applications using clad sheets.

## **6. Advancements in Composite Materials**

This work contributes to the growing industrial adoption of multi-layer and clad materials by demonstrating their reliable behaviour under warm forming conditions. By establishing a strong link between microstructure evolution, mechanical response, and forming performance, the study provides a framework for designing next-generation clad sheets with tailored properties. These insights can accelerate innovation in lightweight structures, corrosion-resistant components, and energy-efficient thermal systems.

## CHAPTER 7

### CONCLUSIONS AND FUTURE RESEARCH SCOPE

#### 7.1 Conclusions

The mechanical behaviour and the formability of the SS430/AA1050 clad sheet are systematically investigated through tensile testing, microstructural analysis, and deep drawing experiments at various temperatures under both dry and lubricated conditions. Also, the deep drawing process is predicted analytically and through finite element analysis. The key conclusions drawn from this study are:

1. The tensile strength of SS430 and AA1050 components decreased with temperature, while the ductility increased for AA1050 and decreased for SS430. The clad sheet exhibited a combined mechanical response reflecting the properties of both the constituent layers.
2. In the case of SS430, the strain hardening exponent ( $n$ ) and normal anisotropy ( $\bar{R}$ ) increased consistently with temperature, contributing to better resistance to thinning. The clad sheet followed a similar trend, improving its formability characteristics. In the case of AA1050 layer the  $n$  value decreased and  $\bar{R}$  value increased with increase in the temperature.
3. The Vickers microhardness (HV0.5) of both constituent layers exhibits a reduction of 12% and 51% in the SS and AA layers, respectively, at 300°C compared to the room temperature.
4. The residual stresses in both SS and AA layers of the deformed clad samples are observed to decrease with an increase in temperature, which is correlated to the strength of the material which decreases with increasing temperature. The SS layer experiences compressive residual stresses, while the AA layer

shows tensile stresses. This trend is attributed to the difference in Young's moduli between the materials, owing to the higher elastic recovery of the AA layer compared to the SS layer.

5. The friction behavior showed that AA1050 consistently had a higher COF than SS430, and friction increased with temperature under dry conditions, reaching 0.42 for AA1050 at 300 °C, indicating a higher risk of sticking friction during warm forming. The use of MoS<sub>2</sub> lubrication significantly reduced friction for both layers at all temperatures.
6. After the deformation of the clad sheet at 300°C depicts an increase in the grain size of SS430 to 12.01 μm from 10.53 μm (at room temperature) attributed to the grain coalescence at boundaries, while that of AA1050 grows to 36.71 μm (at 300°C) from 32 μm (at room temperature).
7. The geometrically necessary dislocation (GND) density increases significantly in both SS430 and AA1050 after room temperature deformation. At 300°C, the GND density decreases due to dislocation annihilation during recovery, reducing barriers to dislocation motion. This reduction in dislocation density leads to a decrease in yield and tensile strength of the clad sheet and parent layers at elevated temperatures.
8. The lower ductility of SS430 at elevated temperatures is caused by the 3.4% rise in HAGBs of deformed specimens at 300°C compared to room temperature. The enhanced ductility of AA1050 at 300°C is due to a 2.6% decrease in HAGBs fraction compared to room temperature.
9. Deformation at elevated temperatures resulted in elongation of grains in the direction of applied load, interfacial refinement, and changes in the texture

intensity. At 300 °C, AA1050 showed reduced texture intensity due to recrystallization, enhancing ductility, while SS430 exhibited increased texture intensity.

10. With dry conditions, forming limits improve up to 180 °C but decline at higher temperatures due to increased friction at the punch and the sheet. MoS<sub>2</sub> used as lubrication significantly enhanced the limit strains, dome heights, and material flow, especially at elevated temperatures. Forming limit diagrams under lubricated conditions showed improved biaxial stretchability and delayed necking. These results highlight the importance of friction control in optimizing clad sheet formability.
11. Deep drawing experiments on clad sheet demonstrate that MoS<sub>2</sub> lubrication significantly enhanced the drawability across all temperatures. Lubrication increases the limiting draw ratio, with highest drawing ratio of 2.0 observed at 300 °C. The peak punch force predicted through the developed analytical model and the finite element analysis is in good agreement with the experimental results.
12. The bond between SS430 and AA1050 layers is strong in Zone I but weak in Zone II, leading to failure in the softer aluminium-rich region during deformation. This bond behaviour influences the tensile properties and fracture patterns.

## 7.2 Future research work

The current analytical, numerical and experimental studies give a thorough understanding of the mechanical behaviour, microstructural properties, and formability of the SS430/AA1050 clad sheet at various temperatures and lubrication

conditions. While the experimental, analytical, and numerical research done provide useful insights, various avenues remain open for additional investigation. There are some issues that can be addressed in future: -

1. In the present research, as received 2-ply cold sheet of AA1050/SS430 have been used formability analysis. In future research, clad sheet can be manufactured through hot roll bonding technique. Clad sheets of different materials and with different thickness ratio can be used for the investigation.
2. In the present investigations, analytical model to predict punch force has been developed using Barlat 1989 yield criterion. In future research work, latest yield criterion like Barlat 2005 yield surfaces can be incorporated.
3. In the present investigations, FEM analysis of deep drawing has been conducted incorporating the Hills 1948 yield surface that is inbuilt in Abaqus. In future research work, latest yield surfaces can be employed by incorporating the user subroutine files in ABAQUS.
4. To improve forecast accuracy, the present analytical and finite element models can be modified to include temperature-dependent anisotropic constitutive laws, viscoplastic effects, and advanced damage criteria. Future research could potentially look into multi-layer material models that reflect the unique deformation characteristics of each layer, especially under warm forming circumstances. Techniques based on machine learning for parameter calibration and optimization may improve predictive capacities even further.
5. The present investigation focused on the formability of clad sheet in circular deep drawing. In future work, the formability can be extended to rectangular deep drawing of multi-ply metallic clad sheets.



6. In the present work, the formability analysis was restricted to the clad layup of aluminium in contact with the punch. In future work, this layup can be reversed with stainless steel layer in contact with punch.
7. The present work can be extended by investigating the mechanical and formability of clad sheet beyond 300°C and also, in cryogenic temperatures.
8. The future research might focus on sophisticated characterisation approaches to gain a better knowledge of interface behaviour. Transmission electron microscopy (TEM), electron backscatter diffraction (EBSD), and nano-indentation are high-resolution methods for measuring interfacial bonding quality, residual stresses, and localized deformation causes. Furthermore, high-strain-rate testing and thermomechanical fatigue studies may be conducted to determine the clad sheet's appropriateness for dynamic or cyclic loading applications.
9. In terms of formability, investigations might be broadened to incorporate various forming techniques such warm hydroforming, incremental sheet forming, and multi-stage deep drawing to assess the material's performance in more complicated industrial settings. Advanced lubrication techniques, such as solid and nano-lubricants, may also be researched for reducing frictional effects at high temperatures. In parallel, surface engineering approaches like as die coating or laser texturing could be investigated to increase tool life and forming quality.

## References

- [1] Sharma, P. K., Gautam, V., and Agarwal, A., 2023, “Effect of Punch Profile Radius and Sheet Setting on Springback in V-Bending of A 2-Ply Sheet,” *Advances in Materials and Processing Technologies*, **9**(2), pp. 416–424. <https://doi.org/10.1080/2374068X.2022.2093011>.
- [2] Sharma, P. K., Gautam, V., and Agrawal, A. K., 2021, “Analytical and Numerical Prediction of Springback of SS/Al-Alloy Cladded Sheet in V-Bending,” *J Manuf Sci Eng*, **143**(3). <https://doi.org/10.1115/1.4048953>.
- [3] Cho, Y.-R., 2021, “Clad Metals: Fabrication, Properties, and Applications,” *Metals (Basel)*, **11**(8), p. 1186. <https://doi.org/10.3390/met11081186>.
- [4] Kim, J.-G., Bae, D.-H., Hahn, B.-D., and Cho, Y.-R., 2017, “Evaluation of the Cross-Plane Thermal Conductivity of Double-Layer Materials,” *Compos B Eng*, **110**, pp. 1–6. <https://doi.org/10.1016/j.compositesb.2016.10.086>.
- [5] Kaminsky, M., 1980, “Clad Materials for Fusion Applications,” *Thin Solid Films*, **73**(1), pp. 117–132. [https://doi.org/10.1016/0040-6090\(80\)90338-7](https://doi.org/10.1016/0040-6090(80)90338-7).
- [6] Asnafi, N., Langstedt, G., Andersson, C.-H., Östergren, N., and Håkansson, T., 2000, “A New Lightweight Metal-Composite-Metal Panel for Applications in the Automotive and Other Industries,” *Thin-Walled Structures*, **36**(4), pp. 289–310. [https://doi.org/10.1016/S0263-8231\(00\)00004-5](https://doi.org/10.1016/S0263-8231(00)00004-5).
- [7] Kalaiyarasan, A., Ramesh, P., and Paramasivam, P., 2018, “Study of Advanced Composite Materials in Aerospace Application,” *Int. J. Sci. Res. Mech. Mater. Eng*, **2**(1), pp. 25–34.
- [8] Nowicke, F., Zavaliangos, A., and Rogers, H. C., 2006, “The Effect of Roll and

- Clad Sheet Geometry on the Necking Instability during Rolling of Clad Sheet Metals,” *Int J Mech Sci*, **48**(8), pp. 868–877. <https://doi.org/10.1016/j.ijmecsci.2006.01.021>.
- [9] Jamaati, R., and Toroghinejad, M. R., 2011, “The Role of Surface Preparation Parameters on Cold Roll Bonding of Aluminum Strips,” *J Mater Eng Perform*, **20**(2), pp. 191–197. <https://doi.org/10.1007/s11665-010-9664-7>.
- [10] Wu, G. Q., Li, Z. F., Luo, G. X., and Huang, Z., 2008, “The Effects of Various Finished Surfaces on Diffusion Bonding,” *Model Simul Mat Sci Eng*, **16**(8), p. 085006. <https://doi.org/10.1088/0965-0393/16/8/085006>.
- [11] Mahabunphachai, S., Koç, M., and Ni, J., 2009, “Pressure Welding of Thin Sheet Metals: Experimental Investigations and Analytical Modeling,” *J Manuf Sci Eng*, **131**(4). <https://doi.org/10.1115/1.3160597>.
- [12] Jamaati, R., and Toroghinejad, M. R., 2010, “Effect of Friction, Annealing Conditions and Hardness on the Bond Strength of Al/Al Strips Produced by Cold Roll Bonding Process,” *Mater Des*, **31**(9), pp. 4508–4513. <https://doi.org/10.1016/j.matdes.2010.04.022>.
- [13] Abbasi, M., and Toroghinejad, M. R., 2010, “Effects of Processing Parameters on the Bond Strength of Cu/Cu Roll-Bonded Strips,” *J Mater Process Technol*, **210**(3), pp. 560–563. <https://doi.org/10.1016/j.jmatprotec.2009.11.003>.
- [14] Buchner, M., Buchner, B., Buchmayr, B., Kilian, H., and Riemelmoser, F., 2008, “Investigation of Different Parameters on Roll Bonding Quality of Aluminium and Steel Sheets,” *International Journal of Material Forming*, **1**(S1), pp. 1279–1282. <https://doi.org/10.1007/s12289-008-0136-7>.
- [15] Cho, Y.-R., 2021, “Clad Metals: Fabrication, Properties, and Applications,”

- Metals (Basel), **11**(8), p. 1186. <https://doi.org/10.3390/met11081186>.
- [16] Long, L. I., Xin-jin, Z., Hui-yun, L. I. U., and Fu-xing, Y. I. N., 2013, “Formation Mechanism of Oxide Inclusion on the Interface of Hot-Rolled Stainless Steel Clad Plates,” *Journal of Iron and Steel Research*, **25**, pp. 43–47.
- [17] Wu, Z. J., Peng, W. F., and Shu, X. D., 2017, “Influence of Rolling Temperature on Interface Properties of the Cross Wedge Rolling of 42CrMo/Q235 Laminated Shaft,” *The International Journal of Advanced Manufacturing Technology*, **91**(1–4), pp. 517–526. <https://doi.org/10.1007/s00170-016-9734-6>.
- [18] Liu, B. X., An, Q., Yin, F. X., Wang, S., and Chen, C. X., 2019, “Interface Formation and Bonding Mechanisms of Hot-Rolled Stainless Steel Clad Plate,” *J Mater Sci*, **54**(17), pp. 11357–11377. <https://doi.org/10.1007/s10853-019-03581-x>.
- [19] Jing, Y., Qin, Y., Zang, X., and Li, Y., 2014, “The Bonding Properties and Interfacial Morphologies of Clad Plate Prepared by Multiple Passes Hot Rolling in a Protective Atmosphere,” *J Mater Process Technol*, **214**(8), pp. 1686–1695. <https://doi.org/10.1016/j.jmatprotec.2014.03.019>.
- [20] Jing, Y., Qin, Y., Zang, X., Shang, Q., and Hua, S., 2014, “A Novel Reduction-Bonding Process to Fabricate Stainless Steel Clad Plate,” *J Alloys Compd*, **617**, pp. 688–698. <https://doi.org/10.1016/j.jallcom.2014.07.186>.
- [21] Qin, Q., Zhang, D., Zang, Y., and Guan, B., 2015, “A Simulation Study on the Multi-Pass Rolling Bond of 316L/Q345R Stainless Clad Plate,” *Advances in Mechanical Engineering*, **7**(7). <https://doi.org/10.1177/1687814015594313>.
- [22] Qin, Q., Wu, Z., Zang, Y., Guan, B., and Zhang, J., 2016, “Warping

- Deformation of 316L/Q345r Stainless Composite Plate after Removal Strake,”  
World Journal of Engineering, **13**(3), pp. 206–209.  
<https://doi.org/10.1108/WJE-06-2016-027>.
- [23] Tachibana, S., Kuronuma, Y., Yokota, T., Yamada, K., Moriya, Y., and Kami, C., 2015, “Effect of Hot Rolling and Cooling Conditions on Intergranular Corrosion Behavior in Alloy625 Clad Steel,” *Corros Sci*, **99**, pp. 125–133.  
<https://doi.org/10.1016/j.corsci.2015.06.028>.
- [24] Xie, G., Luo, Z., Wang, G., Li, L., and Wang, G., 2011, “Interface Characteristic and Properties of Stainless Steel/HSLA Steel Clad Plate by Vacuum Rolling Cladding,” *Mater Trans*, **52**(8), pp. 1709–1712.  
<https://doi.org/10.2320/matertrans.M2011127>.
- [25] Khan, H. A., Asim, K., Akram, F., Hameed, A., Khan, A., and Mansoor, B., 2021, “Roll Bonding Processes: State-of-the-Art and Future Perspectives,” *Metals (Basel)*, **11**(9), p. 1344. <https://doi.org/10.3390/met11091344>.
- [26] Zhang, W., Bay, N., and Wanheim, T., 1992, “Influence of Hydrostatic Pressure in Cold-Pressure Welding,” *CIRP Annals*, **41**(1), pp. 293–297.  
[https://doi.org/10.1016/S0007-8506\(07\)61207-4](https://doi.org/10.1016/S0007-8506(07)61207-4).
- [27] Derby, B., and Wallach, E. R., 1984, “Diffusion Bonding: Development of Theoretical Model,” *Metal Science*, **18**(9), pp. 427–431.  
<https://doi.org/10.1179/030634584790419809>.
- [28] Shirzadi, A. A., Assadi, H., and Wallach, E. R., 2001, “Interface Evolution and Bond Strength When Diffusion Bonding Materials with Stable Oxide Films,” *Surface and Interface Analysis*, **31**(7), pp. 609–618.  
<https://doi.org/10.1002/sia.1088>.

- [29] "Https://Enggwave.Weebly.Com/Sheet-Metal-Forming.Html."
- [30] Kleiner, M., Geiger, M., and Klaus, A., 2003, "Manufacturing of Lightweight Components by Metal Forming," *CIRP Annals*, **52**(2), pp. 521–542. [https://doi.org/10.1016/S0007-8506\(07\)60202-9](https://doi.org/10.1016/S0007-8506(07)60202-9).
- [31] Hosford, W. F. ; C. R. M., 2011, *Metal Forming: Mechanics and Metallurgy*, Cambridge University Press: New York.
- [32] Sorce, F. S., Ngo, S., Lowe, C., and Taylor, A. C., 2019, "Quantification of Coating Surface Strains in Erichsen Cupping Tests," *J Mater Sci*, **54**(10), pp. 7997–8009. <https://doi.org/10.1007/s10853-019-03392-0>.
- [33] S. S. Hecker, 1974, "Cup Test for Assessing Stretchability," *Met Eng Q*, **14**(4), pp. 30–36.
- [34] Duncan, J. ; K. J. ; G. G., 1976, "Bulge Testing as an Aid to Formability Assessment," *Sheet Metal Forming and Energy Conservation*, **9**, pp. 131–150.
- [35] Prakash, V., Kumar, D. R., Horn, A., Hagenah, H., and Merklein, M., 2020, "Modeling Material Behavior of AA5083 Aluminum Alloy Sheet Using Biaxial Tensile Tests and Its Application in Numerical Simulation of Deep Drawing," *The International Journal of Advanced Manufacturing Technology*, **106**(3–4), pp. 1133–1148. <https://doi.org/10.1007/s00170-019-04587-0>.
- [36] Swift, H., 1954, "The Mechanism of a Simple Deep-Drawing Operation," *Sheet Met Ind*, **31**(3), pp. 817–828.
- [37] Keeler, S. P., 1965, "Determination of Forming Limits in Automotive Stampings." <https://doi.org/10.4271/650535>.
- [38] Goodwin, G. M., 1968, "Application of Strain Analysis to Sheet Metal Forming Problems in the Press Shop." <https://doi.org/10.4271/680093>.

- [39] Ravi Kumar, D., 2002, “Formability Analysis of Extra-Deep Drawing Steel,” *J Mater Process Technol*, **130–131**, pp. 31–41. [https://doi.org/10.1016/S0924-0136\(02\)00789-6](https://doi.org/10.1016/S0924-0136(02)00789-6).
- [40] Serope Kalpakjian, and Steven R. Schmid, 2001, *Manufacturing Engineering and Technology*, Pearson Education, Inc.
- [41] Nakazima, K. ; K. T. ; A. K., 1971, “Study on the Formability of Steel Sheet,” Yawata Technical Report, pp. 678–680.
- [42] J. Hu, Z. M. and J. D., 2002, *Mechanics of Sheet Metal Forming*. , Elsevier.
- [43] Gautam, V., Sharma, P., and Ravi Kumar, D., 2018, “Experimental and Numerical Studies on Spring Back in U-Bending of 3-Ply Cladded Sheet Metal,” *Mater Today Proc*, **5(2)**, pp. 4421–4430. <https://doi.org/10.1016/j.matpr.2017.12.010>.
- [44] Kim, I.-K., and Hong, S. I., 2013, “Effect of Component Layer Thickness on the Bending Behaviors of Roll-Bonded Tri-Layered Mg/Al/STS Clad Composites,” *Mater Des*, **49**, pp. 935–944. <https://doi.org/10.1016/j.matdes.2013.02.052>.
- [45] Akramifard, H. R., Mirzadeh, H., and Parsa, M. H., 2014, “Cladding of Aluminum on AISI 304L Stainless Steel by Cold Roll Bonding: Mechanism, Microstructure, and Mechanical Properties,” *Materials Science and Engineering: A*, **613**, pp. 232–239. <https://doi.org/10.1016/j.msea.2014.06.109>.
- [46] Abedi, R., and Akbarzadeh, A., 2015, “Bond Strength and Mechanical Properties of Three-Layered St/AZ31/St Composite Fabricated by Roll Bonding,” *Mater Des*, **88**, pp. 880–888. <https://doi.org/10.1016/j.matdes.2015.09.043>.



- [47] Okui, T., Yoshida, K., and Yonemitsu, Y., 2014, "Development of Metal Clad Sheets and Strips," Nippon Steel and Sumitomo Metal Technical Report, **106**, pp. 103–107.
- [48] Karajibani, E., Hashemi, R., and Sedighi, M., 2016, "Determination of Forming Limit Curve in Two-Layer Metallic Sheets Using the Finite Element Simulation," Proceedings of the Institution of Mechanical Engineers, Part L: Journal of Materials: Design and Applications, **230**(6), pp. 1018–1029. <https://doi.org/10.1177/1464420715593565>.
- [49] Akramifard, H. R., Mirzadeh, H., and Parsa, M. H., 2014, "Cladding of Aluminum on AISI 304L Stainless Steel by Cold Roll Bonding: Mechanism, Microstructure, and Mechanical Properties," Materials Science and Engineering: A, **613**, pp. 232–239. <https://doi.org/10.1016/j.msea.2014.06.109>.
- [50] Akramifard, H. R., Mirzadeh, H., and Parsa, M. H., 2014, "Cladding of Aluminum on AISI 304L Stainless Steel by Cold Roll Bonding: Mechanism, Microstructure, and Mechanical Properties," Materials Science and Engineering: A, **613**, pp. 232–239. <https://doi.org/10.1016/j.msea.2014.06.109>.
- [51] Choi, S.-H., Kim, K.-H., Oh, K. H., and Lee, D. N., 1997, "Tensile Deformation Behavior of Stainless Steel Clad Aluminum Bilayer Sheet," Materials Science and Engineering: A, **222**(2), pp. 158–165. [https://doi.org/10.1016/S0921-5093\(96\)10514-1](https://doi.org/10.1016/S0921-5093(96)10514-1).
- [52] Nyung Lee, D., and Keun Kim, Y., 1988, "Tensile Properties of Stainless Steel-Clad Aluminium Sandwich Sheet Metals," J Mater Sci, **23**(4), pp. 1436–1442. <https://doi.org/10.1007/BF01154614>.
- [53] Masoumi, M., and Emadoddin, E., 2013, "Interface Characterization and

- Formability of Two and Three-Layer Composite Sheets Manufactured by Roll Bonding,” *Materials & Design* (1980-2015), **44**, pp. 392–396. <https://doi.org/10.1016/j.matdes.2012.08.030>.
- [54] Yoshida, F., and Hino, R., 1997, “Forming Limit of Stainless Steel-Clad Aluminium Sheets under Plane Stress Condition,” *J Mater Process Technol*, **63**(1–3), pp. 66–71. [https://doi.org/10.1016/S0924-0136\(96\)02601-5](https://doi.org/10.1016/S0924-0136(96)02601-5).
- [55] Kim, R. E., Gu, G. H., Kwon, H., Ahn, S. Y., Kwon, J., Lee, J. A., Choi, Y. T., Seo, M. H., and Kim, H. S., 2022, “Role of Synergistic Hardening and Damage Evolution on the Stretchability of Al1050/Steel/Al1050 Sheets,” *Journal of Materials Research and Technology*, **21**, pp. 3514–3525. <https://doi.org/10.1016/j.jmrt.2022.10.143>.
- [56] Cao, M., Deng, K., Nie, K., Wang, C., Wang, L., and Liang, W., 2020, “Microstructure, Mechanical Properties and Formability of Ti/Al/Ti Laminated Composites Fabricated by Hot-Pressing,” *J Manuf Process*, **58**, pp. 322–334. <https://doi.org/10.1016/j.jmapro.2020.08.013>.
- [57] Manesh, H. D., and Taheri, A. K., 2003, “Bond Strength and Formability of an Aluminum-Clad Steel Sheet,” *J Alloys Compd*, **361**(1–2), pp. 138–143. [https://doi.org/10.1016/S0925-8388\(03\)00392-X](https://doi.org/10.1016/S0925-8388(03)00392-X).
- [58] Basril, M. A. M., Teng, H. M., Azuddin, M., and Choudhury, I. A., 2017, “The Effect of Heating Temperature and Methods towards the Formability of Deep Drawn Square Metal Cup,” *IOP Conf Ser Mater Sci Eng*, **210**, p. 012067. <https://doi.org/10.1088/1757-899X/210/1/012067>.
- [59] Jayahari, L., Naik, B. B., and Singh, S. K., 2014, “Effect of Process Parameters and Metallographic Studies of ASS-304 Stainless Steel at Various

- Temperatures under Warm Deep Drawing,” *Procedia Materials Science*, **6**, pp. 115–122. <https://doi.org/10.1016/j.mspro.2014.07.013>.
- [60] Ghosh, M., Miroux, A., Werkhoven, R. J., Bolt, P. J., and Kestens, L. A. I., 2014, “Warm Deep-Drawing and Post Drawing Analysis of Two Al–Mg–Si Alloys,” *J Mater Process Technol*, **214**(4), pp. 756–766. <https://doi.org/10.1016/j.jmatprotec.2013.10.020>.
- [61] Alinia, S., Khamedi, R., and Ahmadi, I., 2018, “The Investigation and Optimization of Process Parameters in Warm Deep Drawing of ASS304 Steel Using Box Behnken Design and Applying Temperature Gradient,” *Exp Tech*, **42**(6), pp. 645–657. <https://doi.org/10.1007/s40799-018-0285-7>.
- [62] Goud, R. R., Prasad, K. E., and Singh, S. K., 2014, “Formability Limit Diagrams of Extra-Deep-Drawing Steel at Elevated Temperatures,” *Procedia Materials Science*, **6**, pp. 123–128. <https://doi.org/10.1016/j.mspro.2014.07.014>.
- [63] Basak, S., Panda, S. K., and Lee, M.-G., 2020, “Formability and Fracture in Deep Drawing Sheet Metals: Extended Studies for Pre-Strained Anisotropic Thin Sheets,” *Int J Mech Sci*, **170**, p. 105346. <https://doi.org/10.1016/j.ijmecsci.2019.105346>.
- [64] Singh, A., Basak, S., P.S., L. P., Roy, G. G., Jha, M. N., Mascarenhas, M., and Panda, S. K., 2018, “Prediction of Earing Defect and Deep Drawing Behavior of Commercially Pure Titanium Sheets Using CPB06 Anisotropy Yield Theory,” *J Manuf Process*, **33**, pp. 256–267. <https://doi.org/10.1016/j.jmapro.2018.05.003>.
- [65] Lin, P., Sun, Y., Chi, C., and Wang, W., 2017, “Effect of Plastic Anisotropy of ZK60 Magnesium Alloy Sheet on Its Forming Characteristics during Deep

- Drawing Process,” *The International Journal of Advanced Manufacturing Technology*, **88**(5–8), pp. 1629–1637. <https://doi.org/10.1007/s00170-016-8816-9>.
- [66] Atrian, A., and Fereshteh-Saniee, F., 2013, “Deep Drawing Process of Steel/Brass Laminated Sheets,” *Compos B Eng*, **47**, pp. 75–81. <https://doi.org/10.1016/j.compositesb.2012.10.023>.
- [67] Atrian, A., and Panahi, H., 2018, “Experimental and Finite Element Investigation on Wrinkling Behaviour in Deep Drawing Process of Al3105/Polypropylene/Steel304 Sandwich Sheets,” *Procedia Manuf*, **15**, pp. 984–991. <https://doi.org/10.1016/j.promfg.2018.07.396>.
- [68] Pazand, K., Moarrefzadeh, A., and Morovvati, M. R., 2022, “Experimental and Numerical Evaluation of Formability in Three-Layer Metallic Sheets with Various Layer Arrangements,” *Engineering Research Express*, **4**(3), p. 035034. <https://doi.org/10.1088/2631-8695/ac89ce>.
- [69] Karajibani, E., Fazli, A., and Hashemi, R., 2015, “Numerical and Experimental Study of Formability in Deep Drawing of Two-Layer Metallic Sheets,” *The International Journal of Advanced Manufacturing Technology*, **80**(1–4), pp. 113–121. <https://doi.org/10.1007/s00170-015-6978-5>.
- [70] Afshin, E., and Kadkhodayan, M., 2015, “An Experimental Investigation into the Warm Deep-Drawing Process on Laminated Sheets under Various Grain Sizes,” *Mater Des*, **87**, pp. 25–35. <https://doi.org/10.1016/j.matdes.2015.07.061>.
- [71] Trzepieciński, T., Pieja, T., Malinowski, T., Smusz, R., and Motyka, M., 2018, “Investigation of 17-4PH Steel Microstructure and Conditions of Elevated

- Temperature Forming of Turbine Engine Strut,” *J Mater Process Technol*, **252**, pp. 191–200. <https://doi.org/10.1016/j.jmatprotec.2017.09.026>.
- [72] Trzepieciński, T., 2020, “Recent Developments and Trends in Sheet Metal Forming,” *Metals (Basel)*, **10**(6), p. 779. <https://doi.org/10.3390/met10060779>.
- [73] Hussaini, S. M., Krishna, G., Gupta, A. K., and Singh, S. K., 2015, “Development of Experimental and Theoretical Forming Limit Diagrams for Warm Forming of Austenitic Stainless Steel 316,” *J Manuf Process*, **18**, pp. 151–158. <https://doi.org/10.1016/j.jmapro.2015.03.005>.
- [74] Laurent, H., Coër, J., Manach, P. Y., Oliveira, M. C., and Menezes, L. F., 2015, “Experimental and Numerical Studies on the Warm Deep Drawing of an Al–Mg Alloy,” *Int J Mech Sci*, **93**, pp. 59–72. <https://doi.org/10.1016/j.ijmecsci.2015.01.009>.
- [75] Kumar, M., Sotirov, N., and Chimani, C. M., 2014, “Investigations on Warm Forming of AW-7020-T6 Alloy Sheet,” *J Mater Process Technol*, **214**(8), pp. 1769–1776. <https://doi.org/10.1016/j.jmatprotec.2014.03.024>.
- [76] Tokita, Y., Nakagaito, T., Tamai, Y., and Urabe, T., 2017, “Stretch Formability of High Strength Steel Sheets in Warm Forming,” *J Mater Process Technol*, **246**, pp. 77–84. <https://doi.org/10.1016/j.jmatprotec.2017.03.012>.
- [77] Venema, J., Matthews, D. T. A., Hazrati, J., Wörmann, J., and van den Boogaard, A. H., 2017, “Friction and Wear Mechanisms during Hot Stamping of AlSi Coated Press Hardening Steel,” *Wear*, **380–381**, pp. 137–145. <https://doi.org/10.1016/j.wear.2017.03.014>.
- [78] Leu, D.-K., 1997, “Prediction of the Limiting Drawing Ratio and the Maximum Drawing Load in Cup-Drawing,” *Int J Mach Tools Manuf*, **37**(2), pp. 201–213.

[https://doi.org/10.1016/0890-6955\(95\)00107-7](https://doi.org/10.1016/0890-6955(95)00107-7).

- [79] Azodi, H. D., Moslemi Naeini, H., Parsa, M. H., and Liaghat, G. H., 2008, “Analysis of Rupture Instability in the Hydromechanical Deep Drawing of Cylindrical Cups,” *The International Journal of Advanced Manufacturing Technology*, **39**(7–8), pp. 734–743. <https://doi.org/10.1007/s00170-007-1262-y>.
- [80] ŞENER, B., 2021, “Investigation of the Prediction Capability of Yld89 Yield Criterion for Highly Anisotropic Sheet Materials,” *Journal of Advances in Manufacturing Engineering*, pp. 7–13. <https://doi.org/10.14744/ytu.jame.2021.00002>.
- [81] Aghchai, A. J., Shakeri, M., and Mollaei-Dariani, B., 2008, “Theoretical and Experimental Formability Study of Two-Layer Metallic Sheet (Al100/St12),” *Proc Inst Mech Eng B J Eng Manuf*, **222**(9), pp. 1131–1138. <https://doi.org/10.1243/09544054JEM1140>.
- [82] Bagherzadeh, S., Mollaei-Dariani, B., and Malekzadeh, K., 2012, “Theoretical Study on Hydro-Mechanical Deep Drawing Process of Bimetallic Sheets and Experimental Observations,” *J Mater Process Technol*, **212**(9), pp. 1840–1849. <https://doi.org/10.1016/j.jmatprotec.2012.04.002>.
- [83] Li, S., Luo, C., Liu, Z., Zhao, J., Han, J., and Wang, T., 2020, “Interface Characteristics and Mechanical Behavior of Cu/Al Clad Plate Produced by the Corrugated Rolling Technique,” *J Manuf Process*, **60**, pp. 75–85. <https://doi.org/10.1016/j.jmapro.2020.10.015>.
- [84] Dhib, Z., Guermazi, N., Ktari, A., Gasperini, M., and Haddar, N., 2017, “Mechanical Bonding Properties and Interfacial Morphologies of Austenitic

- Stainless Steel Clad Plates,” *Materials Science and Engineering: A*, **696**, pp. 374–386. <https://doi.org/10.1016/j.msea.2017.04.080>.
- [85] Liu, Y., Li, Y., Wang, Z., Liu, Y., Wang, T., Huang, Q., and Wang, T., 2023, “Deformation Mechanism and Microstructure Evolution in Stainless Steel Clad Plate of Longitudinal Corrugated Hot Rolling,” *J Mater Process Technol*, **316**, p. 117957. <https://doi.org/10.1016/j.jmatprotec.2023.117957>.
- [86] Wu, K., Chang, H., Maawad, E., Gan, W. M., Brokmeier, H. G., and Zheng, M. Y., 2010, “Microstructure and Mechanical Properties of the Mg/Al Laminated Composite Fabricated by Accumulative Roll Bonding (ARB),” *Materials Science and Engineering: A*, **527**(13–14), pp. 3073–3078. <https://doi.org/10.1016/j.msea.2010.02.001>.
- [87] LI, X., ZU, G., and WANG, P., 2015, “Microstructural Development and Its Effects on Mechanical Properties of Al/Cu Laminated Composite,” *Transactions of Nonferrous Metals Society of China*, **25**(1), pp. 36–45. [https://doi.org/10.1016/S1003-6326\(15\)63576-2](https://doi.org/10.1016/S1003-6326(15)63576-2).
- [88] Wang, T., Wang, Y., Bian, L., and Huang, Q., 2019, “Microstructural Evolution and Mechanical Behavior of Mg/Al Laminated Composite Sheet by Novel Corrugated Rolling and Flat Rolling,” *Materials Science and Engineering: A*, **765**, p. 138318. <https://doi.org/10.1016/j.msea.2019.138318>.
- [89] Nie, H., Liang, W., Chen, H., Wang, F., Li, T., Chi, C., and Li, X. rong, 2019, “A Coupled EBSD/TEM Study on the Interfacial Structure of Al/Mg/Al Laminates,” *J Alloys Compd*, **781**, pp. 696–701. <https://doi.org/10.1016/j.jallcom.2018.11.366>.
- [90] Han, J., Li, S., Gao, X., Huang, Z., Wang, T., and Huang, Q., 2023, “Effect of



- Annealing Process on Interface Microstructure and Mechanical Property of the Cu/Al Corrugated Clad Sheet,” *Journal of Materials Research and Technology*, **23**, pp. 284–299. <https://doi.org/10.1016/j.jmrt.2022.12.188>.
- [91] Carpenter, J. S., Nizolek, T., McCabe, R. J., Knezevic, M., Zheng, S. J., Eftink, B. P., Scott, J. E., Vogel, S. C., Pollock, T. M., Mara, N. A., and Beyerlein, I. J., 2015, “Bulk Texture Evolution of Nanolamellar Zr–Nb Composites Processed via Accumulative Roll Bonding,” *Acta Mater*, **92**, pp. 97–108. <https://doi.org/10.1016/j.actamat.2015.03.020>.
- [92] Kolahi, A., Akbarzadeh, A., and Barnett, M. R., 2009, “Electron Back Scattered Diffraction (EBSD) Characterization of Warm Rolled and Accumulative Roll Bonding (ARB) Processed Ferrite,” *J Mater Process Technol*, **209**(3), pp. 1436–1444. <https://doi.org/10.1016/j.jmatprotec.2008.03.064>.
- [93] Barlat, F., and Lian, K., 1989, “Plastic Behavior and Stretchability of Sheet Metals. Part I: A Yield Function for Orthotropic Sheets under Plane Stress Conditions,” *Int J Plast*, **5**(1), pp. 51–66. [https://doi.org/10.1016/0749-6419\(89\)90019-3](https://doi.org/10.1016/0749-6419(89)90019-3).
- [94] Gautam, V., Raut, V. M., and Kumar, D. R., 2018, “Analytical Prediction of Springback in Bending of Tailor-Welded Blanks Incorporating Effect of Anisotropy and Weld Zone Properties,” *Proceedings of the Institution of Mechanical Engineers, Part L: Journal of Materials: Design and Applications*, **232**(4), pp. 294–306. <https://doi.org/10.1177/1464420715624261>.
- [95] J. Fish, and T. Belytschko, 2007, *A First Course in Finite Elements*, John Wiley & Sons.
- [96] G. P. Nikishkov, 2004, *INTRODUCTION TO THE FINITE ELEMENT*

*METHOD*, Report, University of Aizu, Japan.

- [97] WAGONER, R., and LI, M., 2007, "Simulation of Springback: Through-Thickness Integration," *Int J Plast*, **23**(3), pp. 345–360. <https://doi.org/10.1016/j.ijplas.2006.04.005>.
- [98] Wagoner, R. H., 2005, "Advances in Springback," *AIP Conference Proceedings*, AIP, pp. 209–214. <https://doi.org/10.1063/1.2011219>.
- [99] Xu, W. L., Ma, C. H., Li, C. H., and Feng, W. J., 2004, "Sensitive Factors in Springback Simulation for Sheet Metal Forming," *J Mater Process Technol*, **151**(1–3), pp. 217–222. <https://doi.org/10.1016/j.jmatprotec.2004.04.044>.
- [100] D. Banabic, 2010, *Sheet Metal Forming Processes: Constitutive Modelling and Numerical Simulation.*, Springer Science & Business Media.
- [101] D. Hibbit, B. Karlsson, and P Sorensen, 2010, *ABAQUS/Standard Analysis User's Manual*, Hibbit, Karlsson, Sorensen Inc, Providence,USA.
- [102] KILIÇ, S., KACAR, İ., ÖZTÜRK, F., and TOROS, S., 2019, "FARKLI OPTİMİZASYON YÖNTEMLERİNİN YLD2000 AKMA KRİTERİ KATSAYILARININ TAHMİNLERİNE ETKİLERİ," *Ömer Halisdemir Üniversitesi Mühendislik Bilimleri Dergisi*. <https://doi.org/10.28948/ngumuh.517160>.
- [103] Taira S, T. K. Y. T., 1978, "A Method of X-Ray Microbeam Measurement of Local Stress and Its Application to Fatigue Crack Growth Problems.," *J Soc Mater Sci* 27(294):251–256.
- [104] Sasaki, T., and Hirose, Y., 1997, *Influence of Image Processing Conditions of Debye Scherrer Ring Images in X-Ray Stress Measurement Using an Imaging Plate*.

- [105] Kumar, A., Digavalli, R. K., Gautam, V., and Krishnaswamy, H., 2022, “Characterization of Residual Stresses in Conventional Forming and Hydroforming of Tailor Welded Blanks,” *J Mater Eng Perform*, **31**(12), pp. 10171–10186. <https://doi.org/10.1007/s11665-022-07020-y>.
- [106] George E. Dieter, 1961, *Mechanical Metallurgy*, McGraw Hill.
- [107] Suchy, I., 1998, *Handbook of Die Design*, McGraw-Hill New York, USA.
- [108] Blau, P. J., and Davis, J. R., 1900, *Metals Handbook. Properties and Selection: Irons, Steels, and High-Performance Alloys*, ASM International: Ohio, USA.
- [109] Bong, H. J., Barlat, F., Ahn, D. C., Kim, H.-Y., and Lee, M.-G., 2013, “Formability of Austenitic and Ferritic Stainless Steels at Warm Forming Temperature,” *Int J Mech Sci*, **75**, pp. 94–109. <https://doi.org/10.1016/j.ijmecsci.2013.05.017>.
- [110] Peñalba, F., Gómez-Mitxelena, X., Jiménez, J. A., Carsí, M., and Ruano, O. A., 2016, “Effect of Temperature on Mechanical Properties of 9%Cr Ferritic Steel,” *ISIJ International*, **56**(9), pp. 1662–1667. <https://doi.org/10.2355/isijinternational.ISIJINT-2016-097>.
- [111] Yang, J., Bu, K., Zhou, Y., Song, K., Huang, T., Peng, X., Liu, H., and Du, Y., 2023, “Microstructure, Residual Stress, and Mechanical Properties Evolution of a Cu–Fe–P Alloy under Different Conditions,” *Journal of Materials Research and Technology*, **24**, pp. 7896–7909. <https://doi.org/10.1016/j.jmrt.2023.05.015>.
- [112] Pavlina, E. J., and Van Tyne, C. J., 2008, “Correlation of Yield Strength and Tensile Strength with Hardness for Steels,” *J Mater Eng Perform*, **17**(6), pp. 888–893. <https://doi.org/10.1007/s11665-008-9225-5>.

- [113] Yadav, R. D., and Gautam, V., 2024, “Effect of Magnetic Field on Deformation Behavior of a Steel Sheet in Uniaxial Tension,” *J Test Eval*, **52**(1).  
<https://doi.org/10.1520/JTE20230284>.

## PUBLICATIONS BASED ON THE PRESENT WORK

The followings are the publications in journals and conferences based on the present research work.

### International Journals: -

1. **Bijendra Prasad** and Vijay Gautam (2024) “Experimental and Numerical Investigations of formability of Two-Ply Clad Sheet of Stainless Steel and Aluminium Alloy”. Journal of Metrology Society of India (**Springer**) Vol 39(4), pp. 887–900. <https://doi.org/10.1007/s12647-024-00765-y>.
2. **Bijendra Prasad** and Vijay Gautam (2025) “Temperature-Dependent Mechanical Properties and Interfacial Microstructural Evolution of a 2-ply Clad Sheet”. Journal of Materials Engineering and Performance (**ASM International**). <https://doi.org/10.1007/s11665-025-11895-y>.
3. **Bijendra Prasad** and Vijay Gautam (2026) “Investigations on Formability of a SS/AA Clad Sheet at Elevated Temperatures”. Journal of Engineering Materials and Technology (**ASME**) 148(2): 021002. <https://doi.org/10.1115/1.4070118>.

### International Conferences: -

1. **Bijendra Prasad** and Vijay Gautam “Mechanical characterization and Formability analysis of two-ply clad sheet metal” International conference on Recent Advances in Mechanical Engineering for Sustainable Development (ISME-2024) held at Delhi Technological University during July 11-13, 2024.
2. **Bijendra Prasad** and Vijay Gautam “Effect of Strain Rate on the Stress-Strain Behaviour of Aluminium Alloy at different temperatures” International conference

on Recent Advances in Mechanical Engineering for Sustainable Development  
(ISME-2024) held at Delhi Technological University during July 11-13, 2024.

## BIO DATA

Mr. Bijendra Prasad is currently working as a research scholar in the department of mechanical engineering at Delhi Technological University. Before joining the PhD, he had a total of four years of working experience, with one year in teaching in Galgotias university, Greater Noida, and three years' experience in research and development work at CSIR-AMPRI, Bhopal and ICAR-IARI, New Delhi. His area of research has been in sheet metal forming of composite sheet metal at elevated temperatures, design of machine elements like actuators based on shape memory alloys for below-elbow prosthesis application and component for the microclimate moderation in the tractors for agricultural application. He has authored three SCIE and Scopus indexed journals. He has presented eight papers at national and international conferences. His work was awarded with the best paper award at the international conference ISME-2024. Also, he has been awarded the commendable Research Excellence Award in September 2025 by Delhi Technological University, for his work published in Springer.